

Editorial corner – a personal view

Powder injection molding: Borderlines and interfaces

Gy. Bánhegyi*

Bay Zoltán Nonprofit Ltd., Department of Advanced Materials and Processes, Fehérvári út 130, H-1116 Budapest, Hungary

In addition to traditional thermoplastics injection molding technology (which also produces novelties continuously) there is a special branch exhibiting double digit growth both in developing and in mature markets: powder injection molding. In a broad sense this is a family of technologies by itself, the essence of which is that first a highly filled compound is prepared with metal or ceramic filler, which is injection molded (or compression molded) to a 'green product'. This step is followed by the decomposition of the organic component and by sintering, resulting in a final product. The technology by itself is not new but, due to the almost infinite combination of parameters and components it continuously opens up new possibilities. Here I provide only a non-exhaustive list of possibilities being presently explored. First to mention is the possibility of controlled porosity formation: depending on the selection of the polymer and the inorganic component the resulting final product may be porous or non-porous. Residual porosity depends on the volatility and on the decomposition rate of the polymer and on the conditions of sintering. The degradation and evaporation rate of the organic component may be controlled by forming pores in the green body before the sintering processes e.g. by selective dissolution at the surface using solvents or supercritical fluids. The pores may be filled by ceramic precursor polymers which are transformed into amorphous or nano-crystalline solids on thermal decomposition. A special subgroup of the technologies mentioned is called gel casting, wherein *in situ* formed organic-inorganic hybrids are prepared, molded and decomposed in a

controlled manner into a mostly inorganic final product. (It is not necessary, however, to remove the organic components completely, thermoset organic-inorganic hybrids may also be the final products). It is possible to combine various metallic and/or ceramic components with each other or with polymers, to prepare composites with special electric, optical or magnetic properties. Nano-scale milling of the ceramic or metal components is important, which may include mechanical activation, formation of non-equilibrium (high entropy) phases. If the fine-grained structure is to be preserved the sintering process should be led to stabilize the special non-equilibrium structures (by preventing recrystallization) in the final product. These problems are further aggravated by the fact that typical shrinking in the sintering process may be as high-as 20–30% which means further challenges to the technologists aiming at high dimensional precision. I foresee further possibilities in developing new products and technologies in this exciting field of science and technology, where we are at the borderline of scientific disciplines and where controlled manipulation of interfaces is the key to success.



Dr. György Bánhegyi
Member of Executive Editorial Board

*Corresponding author, e-mail: gyorgy.banhegyi@bzaka.hu
© BME-PT

Thermoplastic polyurethane/(organically modified montmorillonite) nanocomposites produced by in situ polymerization

M. Strankowski^{1*}, J. Strankowska², M. Gazda³, Ł. Piszczyk¹, G. Nowaczyk⁴, S. Jurga⁴

¹Gdansk University of Technology, Chemical Faculty, Department of Polymer Technology, G. Narutowicza Str. 11/12, 80-233 Gdansk, Poland

²University of Gdansk, Faculty of Mathematics, Physics and Informatics, Department of Applied Physics, Wita Stwosza Str. 57, 80-952 Gdansk, Poland

³Gdansk University of Technology, Faculty of Applied Physics and Mathematics, G. Narutowicza Str. 11/12, 80-233 Gdansk, Poland

⁴Adam Mickiewicz University, Faculty of Physics, Department of Macromolecular Physics, Umultowska Str. 85, 61-614 Poznan, Poland

Received 11 October 2011; accepted in revised form 12 February 2012

Abstract. A series of polyurethane nanocomposites were synthesized from thermoplastic polyurethanes (with different hard segment ratios) and two types of organically modified montmorillonites (OMMT) – Cloisite[®] 10A and Cloisite[®] 20A. The thermal behavior was examined by non-isothermal thermogravimetry (TG, DTG), Differential Scanning Calorimetry (DSC) and Dynamic-Mechanical Thermal Analysis (DMTA). The results of X-ray analyses showed that the OMMT produced the intercalated polyurethane nanocomposites. It has been proven that the thermal stability and tensile properties of these new systems were higher when the organoclay was present within the polymer matrix. Moreover, these properties depend on both the OMMT loading and the type of gallery cations of the organically modified montmorillonites.

Keywords: nanocomposite, polyurethane, montmorillonite, Cloisite, thermal analysis

1. Introduction

The development of materials modified with nanofillers is the basis for producing of many sophisticated products. Presently, several works are being carried out aimed at reducing the dimensions of the existent materials, such as powders or metal oxides and to take advantage of new plastic processing technologies [1–3]. The first works with polymer nanocomposites were carried out during the 1980s by Toyota (polyamide nanocomposites) [4], which started intensive research on these materials and the application of different polymer matrixes: *i.a.* polyepoxides [5], polyethylene [6], polypropylene [7],

polyamide 6 and 11 [8–10], natural rubber [11], polyimides [12] and polystyrene [13, 14]. Currently, research is heavily focused on increasing the scope of polymer nanocomposites, mainly in the electrical [15–17], and automotive industries and in packaging production [18].

Polymer nanocomposites obtained from a polyurethane matrix and the adequate nanofillers offer a chance to produce new materials [19, 20], where the least favorable properties of polyurethanes can be improved without compromising their best qualities. Unfortunately, this is very difficult to achieve with common chemical structure modification. The

*Corresponding author, e-mail: micstran@pg.gda.pl
© BME-PT

use of polyurethane nanocomposites is not as extensive as for example polypropylene nanocomposites [21], but interest in them is high because of the enormous opportunities to develop their properties, and thus, opening new opportunities to use these materials in various areas of everyday life and in many industries. Therefore, the probabilities of finding useful applications for polyurethane nanocomposites are very high.

Polymer nanocomposites obtained from natural clays of the montmorillonite type, which consist of layered silicates, have attracted a great deal of attention due to the improvements in the mechanical, thermal, and gas barrier properties of the polymer [22]. Montmorillonite is a natural clay belonging to the 2:1 phyllosilicates and its crystal structure is made of two layers of silica tetrahedra sharing some vertexes with an intercalated octahedral sheet of either aluminum or magnesium hydroxide. These silicates self-organize to form stacks with a regular van der Waals gap between the galleries. The existence of ionic bonds (e.g. Al^{3+} replaced by Mg^{2+} or Fe^{2+} generates negative charges that are counterbalanced by cations like Na^+ , Ca^{2+} or K^+) and the ability to form hydrogen bonds with water make montmorillonite highly hydrophilic and incompatible with organic polymers [23]. The properties' improvement upon organoclay addition is related to the morphological structure and the dispersion efficiency of the organoclay particles in the polymer matrix, which is associated with the compatibility between the polymer and the organoclay. For this reason, in order to achieve an optimal dispersion of the silicates in the polymer, it is of prime importance to modify the montmorillonite with various organic cationic molecules to render the silicates organophilic [24]. This paper presents the effect of Cloisite 10A [25–29] and Cloisite 20A [30–32] on thermoplastic polyurethane elastomers containing various amounts of stiff segments, and the analysis of the materials obtained carried out using different techniques.

2. Experimental

2.1. Materials

Montmorillonites modified with a quaternary ammonium salt (OMMT) [Cloisite 10A (organic modifier 2MBHT: dimethyl, benzyl, hydrogenated tallow, quaternary ammonium) and Cloisite 20A (organic

modifier 2M2HT: dimethyl, dihydrogenated tallow, quaternary ammonium)] (Southern Clay Products Inc. Texas, USA). The polyester polyol, poly(ethylene, butylene)adipate diol, (PEBA) (Poles 55/20) (ZACHEM, Bydgoszcz, Poland). The 4,4'-methylene diisocyanate (MDI) (Borsodchem, Hungary). 1,4-butanediol (1,4-BD) (BASF, Germany). Organically modified montmorillonites were dried for 6 h at 90°C in a thermal vacuum chamber. PEBA and 1,4 BD were dried separately by heating at 100°C and stirring under reduced pressure. MDI was melted at 46°C and filtered before use.

2.2. Nanocomposites preparation

In the first step, OMMT in an amount of 1% by weight was dispersed in PEBA by means of a homogenizer (5000 r.p.m., 80°C, 5 h) and an ultrasound bath. In the second step, a calculated amount of MDI was added to the obtained dispersion and the mixture was stirred at 80°C for 1 hour to obtain a prepolymer. In the third step the prepolymer was mixed with vigorous stirring with 1,4 BD at a 1.05 NCO/OH molar ratio and poured into a heated (90°C) centrifuge drum. After the solidification (30 min) the resulting 2 mm thick band was annealed at 100°C for 6 hours to complete the reaction. Two types of non-modified polyurethanes were obtained, with different amounts of hard segments (TPU_h – 46% HS and TPU_s – 30% HS).

2.3. Nanocomposites characterization

Thermal analysis (TG and DTG curves) was performed using a Perkin-Elmer Thermogravimetric Analyzer TGA Pyris 1 at a heating rate of 20°C·min⁻¹ under nitrogen flow and heating program 25–600°C. DSC measurements were made using a Perkin-Elmer Differential Scanning Calorimeter DSC 7 for encapsulated (aluminum pans) samples of ca. 3–10 mg at a heating/cooling rate of 20°C·min⁻¹ under nitrogen flow. A second melting scan was also performed. The calibration of the temperature and heat flow scales at the same heating rate was performed with In and Zn. For the DMTA measurements an analyzer from Polymer Laboratories was used in bending mode (dual cantilever) (heating form –70 to 120°C at 10Hz frequency and 4°C·min⁻¹ heating rate). The X-ray patterns of the crystalline residues were recorded in an X'Pert Philips diffractometer (source radiation: $\text{CuK}_{\alpha 1}$, $\lambda = 0.1546$ nm,

40 kV, 30 mA) in the $0.5\text{--}10^\circ$ (2θ range) and at scanning rate $0.25^\circ\cdot\text{s}^{-1}$. A Zwick/Roell Z020 testing machine was used to verify the mechanical properties of the samples (ISO 527, tension mode, speed $300\text{ mm}\cdot\text{min}^{-1}$).

3. Results and discussion

3.1. Differential scanning calorimetry (DSC)

The thermal behavior of polyurethane nanocomposites and unmodified TPU was analyzed during a controlled temperature increase. For a system containing a low amount of rigid segments (TPUs), it was observed that the polyurethane nanocomposites melting temperature increased in comparison with its pure reference material (Figure 1a). For TPUs containing 1% of Cloisite 10A the melting temperature increases 2.7°C , whereas for the sample containing 1% Cloisite 20A the maximal melting rate of crystallites was observed to be 6°C higher than the melting temperature of the unmodified system. The enthalpy values of the transitions for the investigated systems containing nanofiller particles, connected with the melting process of the crystalline aggregates, are lower than those of pure polyurethanes (Table 1). The lowest value of transition enthalpy was observed for the nanocomposite with 1% Cloisite 20A [TPUs(20A)]. The decrease in transition heat could be brought about by the interaction of the nanofiller plates with the rigid polyurethane segments, which makes the packing of these domains difficult. Thus, as a consequence of the presence of plates in the nanocomposite structure, the crystallization rate of the modified systems decreases. For polyurethanes containing a higher fraction of rigid segments (TPUh) and nanofiller particles, an

increase of the melting point temperature was observed (Figure 1b). For TPUh(10A) the melting temperature increases 1.6°C in comparison with pure TPUh, whereas for the TPUh(20A) sample the temperature difference referred to the pure reference material was equal to 5.6°C . An interesting fact is that the transition enthalpy for nanocomposites containing 1% Cloisite 10A is about 1.7 J/g higher compared to TPUh, while for the system containing the second nanofiller, TPUh(20A) – the enthalpy value decreases at about 3.9 J/g (Table 1). Most probably, nanofiller Cloisite 10A, having a major chemical affinity towards polyurethane chains, can increase the density of the nucleation process and, as a consequence, a higher value of crystallization enthalpy for TPUh(10A) is observed. It is significant fact is that polyurethanes containing a higher amount of rigid segments also possess higher transition enthalpies.

Polyurethane nanocomposites prepared using the organically modified montmorillonite Cloisite 20A, are characterized by higher melting temperatures compared to systems containing Cloisite 10A.

Table 1. The melting endothermic parameters estimated base on DSC measurements for polyurethane nanocomposites and pure TPU

Sample	Melting temperature (max.) [°C]	Enthalpy (ΔH) [$\text{J}\cdot\text{g}^{-1}$]
TPUh	163.6	16.3
TPUh(10A)	165.2	18.1
TPUh(20A)	169.2	12.4
TPUs	153.7	7.7
TPUs(10A)	156.0	6.7
TPUs(20A)	159.7	5.6

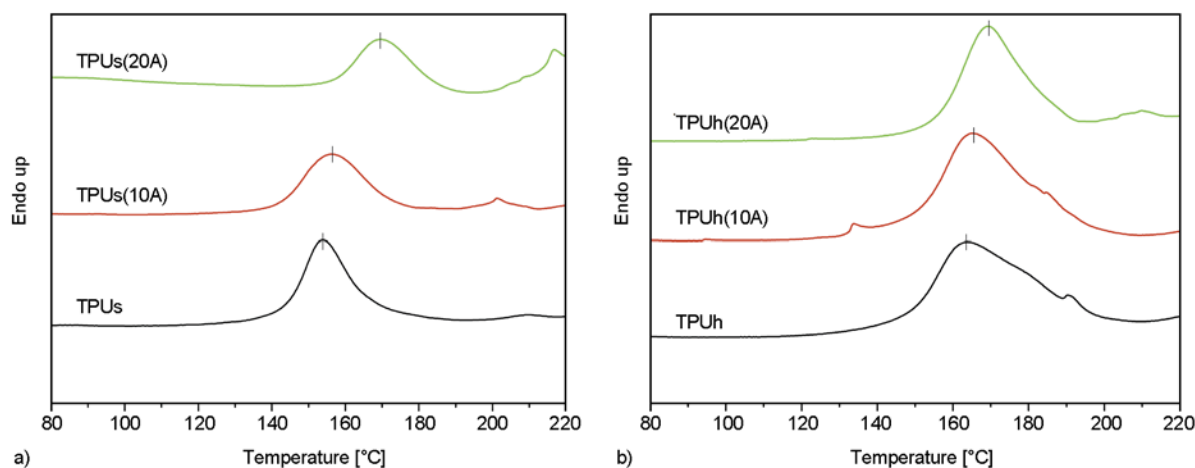


Figure 1. DSC curves for polyurethane nanocomposites and pure TPU

3.2. Dynamic mechanical thermal analysis (DMTA)

The dynamic mechanical thermal analysis of the mechanical properties enabled the estimation of the glass transition temperatures of polyurethanes and systems modified by nanoparticles. Meaningful changes were registered for the storage modulus, which reached higher values in the modified systems, especially in the temperature range above glass transition. The highest value of the storage modulus, at room temperature, was registered for the nanocomposite containing 1% Cloisite 20A (Figure 2a). It was also observed that the addition of both nanofillers caused the stiffening of the more elastic polymer matrix (containing a lower amount of rigid segments).

For systems containing a higher amount of rigid segments in the polymer matrix, the shifting of the loss tangent to lower temperatures (3.6°C less than the unmodified polyurethane) was observed (Figure 2b). For the TPUh (10A) system it was registered that the value of the storage modulus is higher compared to TPUh in the studied temperature range (Table 2). Addition of the second nanofiller (Cloisite 20A) to a more rigid polyurethane matrix did not produce a meaningful increase of the stor-

Table 2. List of temperatures corresponding to the maximum peaks of the $\tan\delta(T)$ curves and storage modulus in $-30, 0, 30^\circ\text{C}$ temperatures

Sample	Storage module E' [log Pa]			$T_{\max}(\tan\delta)$ [°C]
	-30°C	0°C	30°C	
TPUh	8.6	8.2	7.8	-2.0
TPUh(10A)	8.8	8.4	8.1	-5.6
TPUh(20A)	8.7	8.2	7.9	-2.0
TPUs	8.8	7.5	7.2	-6.5
TPUs(10A)	8.8	7.9	7.5	-5.3
TPUs(20A)	8.8	8.1	8.0	-8.3

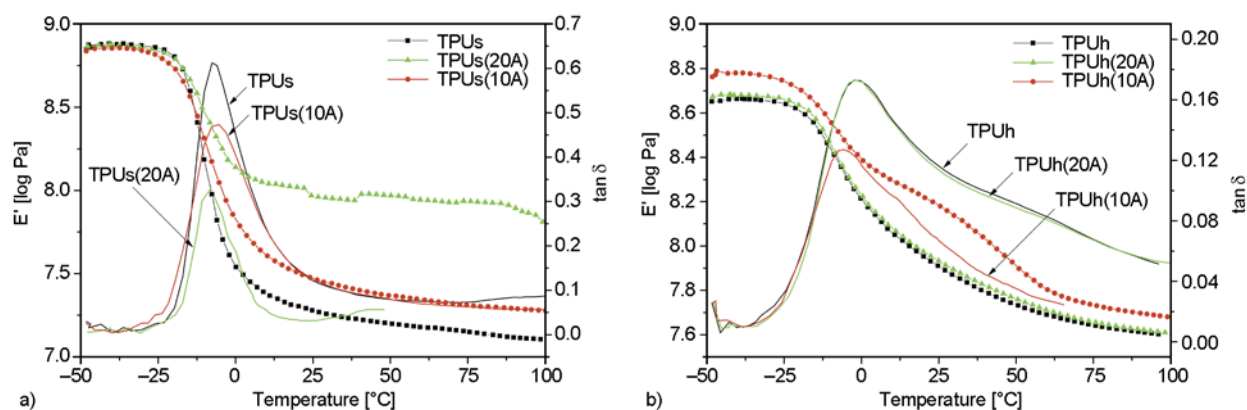


Figure 2. Temperature dependences of dynamic storage modulus (E'), loss tangent ($\tan\delta$) for nanocomposites and TPU

age modulus in the investigated temperature range (Figure 2b). This effect could demonstrate the significant interaction of incorporated nanofillers with the polyurethane phase.

Relatively small amounts of nanofillers incorporated to the polymer matrix caused a distinct increase of the storage modulus values for the modified systems. It should likewise be stressed that systems containing a lower amount of rigid segments in the polymer matrix are more susceptible to interaction, thus the reinforcement effect in these systems is more visible.

3.3. Rheological properties (ARES)

The rheology of polyurethane nanocomposites containing Cloisite 10A or Cloisite 20A was examined in order to obtain information about the influence of nanoparticles on the rheological behavior of polymer alloys. The systems were measured at 200°C and $0.1\div 100$ rad/s frequency range. Nanofiller plates in the systems containing either more (TPUh) or less rigid segments (TPUs) caused an increase of the viscosity of the obtained nanocomposites. For the TPUh(10A) system the highest dynamic viscosity was registered, in comparison to nanocomposites TPUh(20A) obtained using another nanofiller. The opposite behavior was measured for two systems with the lowest amount of rigid segments, where higher viscosity was registered for the TPUs(20A) system. Additionally, TPUs nanocomposites and its TPUs equivalents had higher viscosity values, compared to the values registered for nanocomposites with a more rigid polyurethane matrix and their pure equivalent (TPUh) (Figure 3). The dynamic storage modulus (G') as a frequency function for studied systems has a close characteristic through the whole frequency range (Figure 4a, b). The highest storage modulus values were regis-

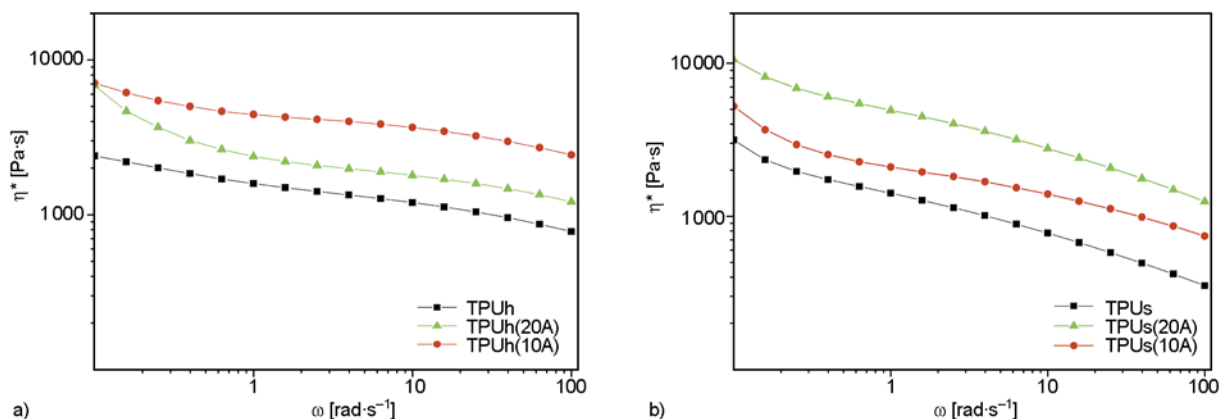


Figure 3. Dynamic viscosity (η^*) dependence on frequency (ω) for TPUh, TPUs and nanocomposites

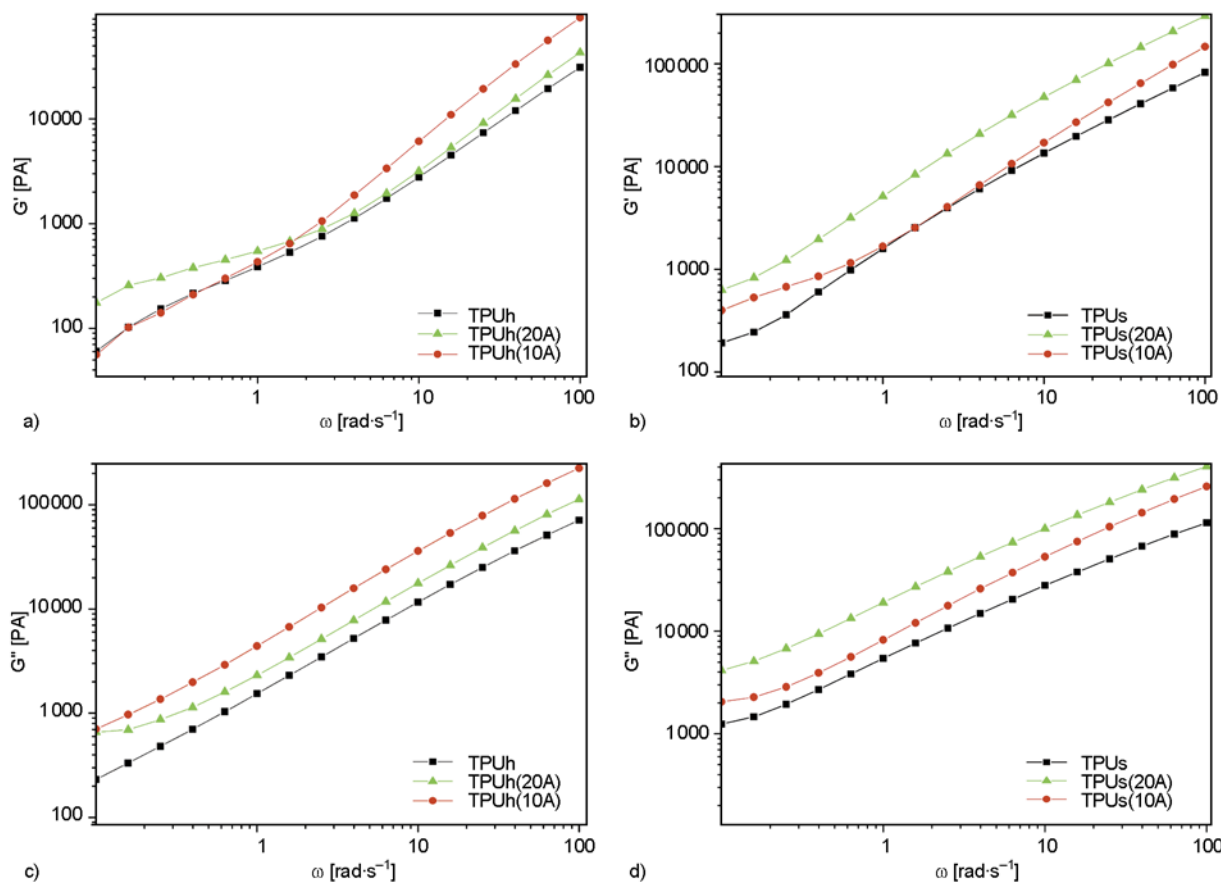


Figure 4. Dynamic loss modulus (G') as a function of the frequency (ω) for TPUh (a), TPUs (b), and nanocomposites. Dynamic loss modulus (G'') as a function of frequency (ω) for TPUh (c), TPUs (d) and nanocomposites.

tered for the TPUs(20A) system. Furthermore, the G' modulus for TPUs, TPUs(10A) and TPUs(20A) systems were higher than for TPUh, TPUh(10A) and TPUh(20A).

For polyurethane nanocomposites obtained using Cloisite 10A and Cloisite 20A, the dynamic loss modulus (G'') as a function of the frequency had higher values in comparison with G'' for their pure equivalents (TPUh and TPUs) (Figure 4c, d). The

highest values of G'' were registered for TPUh(20A) and TPUs(10A). Furthermore, TPUs nanocomposites and unmodified TPUs had higher loss moduli through the whole frequency range had higher loss moduli in comparison with their more rigid equivalents TPUh.

3.4. Thermogravimetric analysis (TGA)

Thermogravimetric analysis is one of the most important methods used to study polymer nanocom-

posites. The results of these experiments make the description of the nanofiller influence on the improvement rate of polymer thermal properties possible. Nonetheless, even for commercial nanocomposites, it is possible to find results of studies that indicate the absence of thermal improvement for modified polymers. The fact is that the preparation of nanocomposites with better thermal parameters than the initial materials is difficult. For all samples the weight losses for the first and second stages were observed (Figure 5b, 6b). The first weight loss during thermal degradation of TPU's is due to the degradation of the hard segment as a consequence of the relatively low thermal stability of the urethane groups whereas the second weight loss has been associated to soft segment decomposition [33]. According to the analysis of the results obtained for nanocomposite systems containing lower amounts of rigid segments in the polyurethane matrix (Figure 5 and 6) a clear improvement of the thermal parameters is visible. Temperatures, at which 95% of

the initial mass of the sample remained, are higher for nanocomposites TPUs(10A) and TPUs(20A) than for the unmodified systems – differences of 9.3 and 13.6°C, respectively (Table 3). Especially obvious is the shifting of the dP_{zm}/dT curve maximum. For TPUs(10A) and TPUs(20A) a shift of about 22.8°C towards higher temperatures can be noticed, which indicates a considerable improvement of thermal strength in nanocomposite systems (Table 3). The addition of Cloisite 10A and Cloisite 20A in considerable quantities improves the thermal strength of polyurethane elastomers containing a lower amount of rigid segments in the polymer matrix. The analysis of the maxima on the derivative curve of % mass conservation as a function of temperature indicates the distinct increase of thermal stability obtained at the 350÷450°C temperature range.

For polyurethane systems containing a higher share of rigid segments – TPUh(10A) and TPUh(20A) – a considerable improvement of thermal stability was

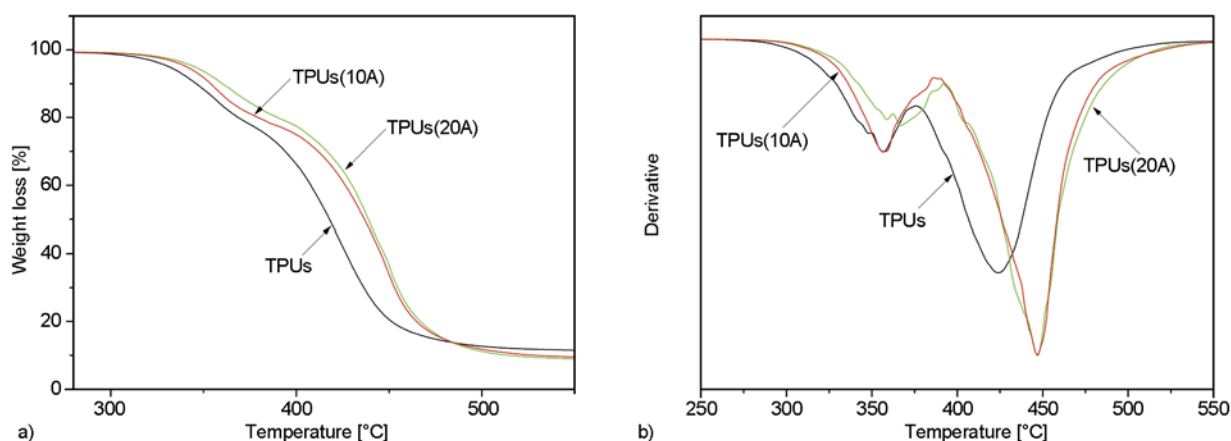


Figure 5. % mass conservation and derivative dependence on temperature for TPUs and TPUs nanocomposites

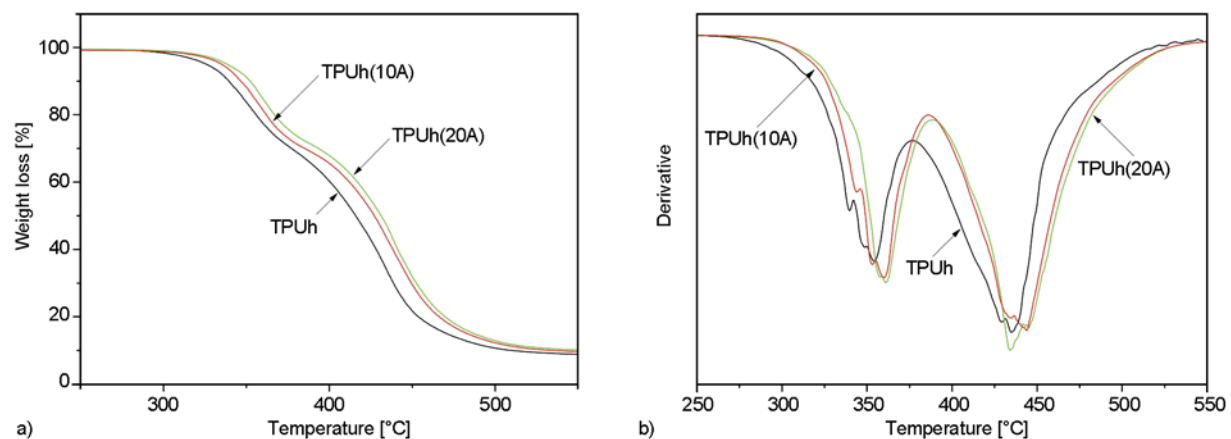


Figure 6. % mass conservation and derivative dependence on temperature for TPUh and TPUh nanocomposites

Table 3. Thermal decomposition of pure TPU and TPU nanocomposites

Sample	Weight loss		T_{\max} [°C]
	5%	50%	
	Temperature [°C]		
TPUs	331.4	417.8	356.3; 424.1
TPUs(10A)	340.7	436.6	357.5; 446.9
TPUs(20A)	345.0	438.7	366.8; 446.7
TPUh	325.8	415.5	354.0; 435.0
TPUh(10A)	335.1	427.2	360.1; 444.0
TPUh(20A)	338.2	431.3	361.0; 434.2

also registered. It is worth noticing that the improvements in thermal stability are visible especially in the early stage of the sample decomposition to gaseous products. 5% mass loss for TPUh(10A) system is observed at 335.1°C temperature, 9.3°C higher than for the TPUh sample. For the TPUh(20A) nanocomposite, the shifting of the temperature at which a 5% mass is lost was recorded to be 12.4°C higher compared to the unmodified system. In the case of nanocomposites with rigid segments, the distinct improvement of thermal stability within flexible segments was not observed. It is noticeable, however, a difference in thermal stability, especially in an early stage of decomposition, between TPUs and TPUh systems. It is related to a lower amount of thermally weaker urethane bond occurring in the TPUs sample, which causes a higher thermal resistance in this type of system. Comparing the different nanofillers applied to the modification of polyurethane, it was noticed that, regarding thermal stability, it seems to be favorable to use Cloisite 20A. Nonetheless, both nanoclays used to prepare the polyurethane systems produced the desired effect on the thermal properties of the obtained products.

3.5. Mechanical properties

For all the prepared nanocomposite systems strength experiments were performed. The most distinct reinforcement effect of nanofiller particles was observed in their extension measurements. For a more elastic polyurethane matrix, containing 1% Cloisite 10A – TPUs(10A), an improvement of the stress at break of up to 10 MPa compared to the unmodified polyurethane was obtained (Table 4). When the second nanofiller (Cloisite 20A) was added to a system containing a lower amount of rigid segments, the stress at break was equal to 41.2 MPa (Table 4). This value is 8 MPa higher than that for pure thermoplastic polyurethane (TPUs). With the increase of the stress needed to break the samples, a relative elongation at break-increase of the elongation at break was not observed. TPUs(10A) and TPUs(20A) reveal negligibly lower values for the maximal relative elongation at break (Figure 7a). This means that the nanofillers influence on the polyurethane matrix results in it stiffening. In a system containing a higher amount of rigid segments, an improvement of the mechanical properties of the samples was also observed as a consequence of organoclay addition. The highest value of stress at break was registered for the TPUh(10A) sample and equals to 46.7, 14.1 MPa higher than for the TPUh system without a nanofiller (Table 4, Figure 7b). Compared to the pure polyurethane, the stress at break for TPUh(20A) containing Cloisite 20A increases up to 11.2 MPa (Table 4). Polyurethanes modified by nanofillers, with a higher amount of rigid segments, exhibit a lower relative elongation at break in comparison with their pure reference materials.

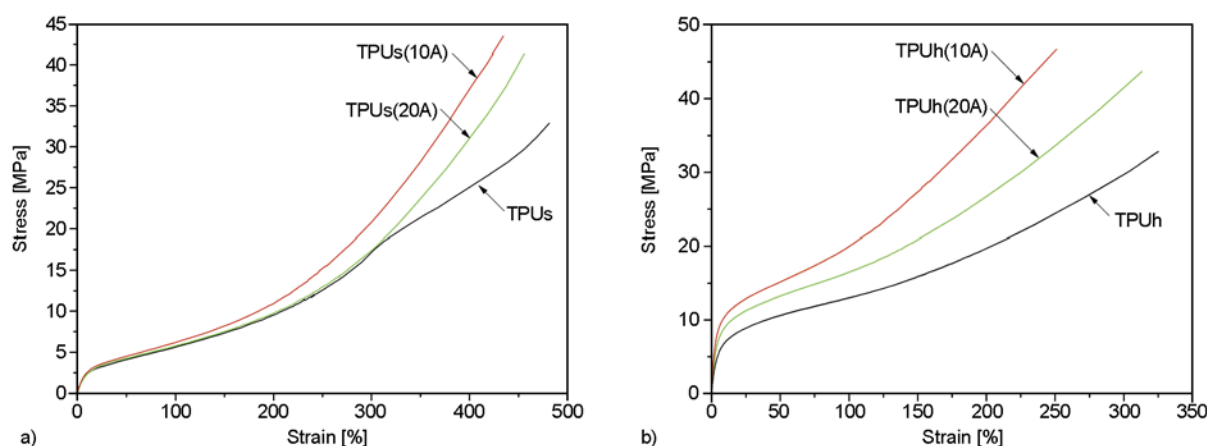
**Figure 7.** Stress dependence on relative extension during elongation for TPU and TPU nanocomposites

Table 4. List of stress at break and relative extension during elongation for TPU and TPU nanocomposites

Sample	Max. Stress [MPa]	Max. Strain [%]
TPUh	32.6	325
TPUh(10A)	46.7	251
TPUh(20A)	43.8	313
TPUs	33.2	481
TPUs(10A)	43.5	436
TPUs(20A)	41.2	455

Therefore, the addition of nanofiller particles to thermoplastic polyurethanes caused an increase in the intensity of the stress needed to break the sample and a negligible decrease of the maximal relative elongation at break. A greater improvement in strength properties is observed when the Cloisite 10A nanofiller is added to the polyurethane matrix (Figure 7a, b). It can be caused by a higher compatibility of this nanofiller towards polyurethane chains. Also, the dispersion rate of the particles very sensitively influences the mechanical properties of the polyurethane nanocomposites, and, related with this, the functional features of the materials obtained.

3.6. X-ray diffraction (XRD)

The X-ray diffraction method is able to describe the degree of nanofiller intercalation between polymer chains and to indicate what kind of dispersive system was obtained. The diffraction spectra of Cloisite 10A and Cloisite 20A made an estimation of the nanocomposite interlayer distances possible (Table 5). Pure, unmodified montmorillonite (MMT) has a diffractive maximum at $2\theta = 6.8^\circ$ which belongs to a distance between galleries equal to 1.28 nm. Organically modified montmorillonites (Cloisite 10A and Cloisite 20A) have therefore

much wider galleries compared with pure MMT. The increase of interlayer spaces allows polymer chains to penetrate more easily into the nanofiller plates. Pure polyurethanes in the $2\theta = 1\div 10^\circ$ angle range have no diffractive maxima (Figure 8a, b). Therefore, the degree of semicrystallinity of the obtained polyurethane elastomers is difficult to estimate using diffractive methods. On that, the XRD analysis points to amorphous polyurethane systems. For TPUs(10A), a distinct diffractive maximum shifting towards lower angles is observed, which means that the interlayer space between the MMT plates increases from 1.86 nm to 3.32 nm (Figure 8a). The TPUh(10A) nanocomposite, characterized by a more rigid polymer matrix and containing Cloisite 10A, presents a diffractive maximum at $2\theta = 2.75^\circ$. It belongs to a broadening of the nanoclay galleries to about 1.35 nm. Additionally, for this sample, the decrease of the diffractive maximum intensity was observed. This is probably related to the partial exfoliation process of the nanofiller in the polyurethane matrix. In the X-ray spectra of nanocomposites with Cloisite 10A a second, less intensive, diffractive maximum also occurs at $2\theta \approx 5.2^\circ$, which is connected with the next diffraction order – d(002). For TPUs(20A) obtained using the second nanofiller, which was in this case incorporated to a more elastic polyurethane matrix, a diffractive maximum shifting d(001) from 2.48 to 3.46° was observed (Table 5, Figure 8b). A similar 2θ angle value was estimated for TPUh(20A) – the interlayer space in this sample increases to 3.57 nm. Cloisite 20A maxima ($2\theta = 3.6^\circ$) presents a higher intensity than nanocomposites obtained from the second type of nanofiller. In this case, it seems that the polyurethane chains pene-

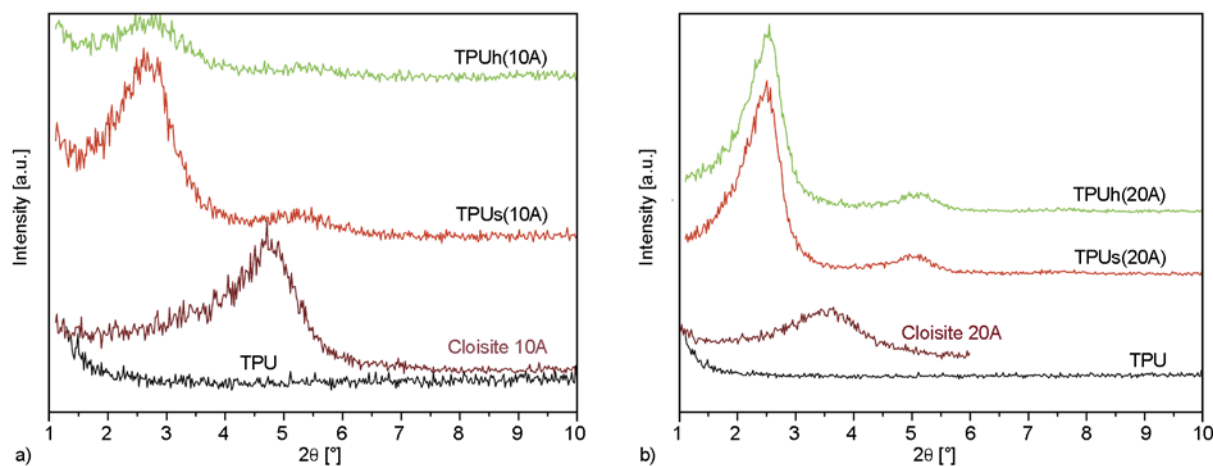
**Figure 8.** X-ray spectra of polyurethane nanocomposites and its pure reference materials

Table 5. List of diffractive maxima and interlayer spacer for TPU nanocomposites and TPU

Sample	2 θ [°]	d ₀₀₁ [nm]
TPUh	–	–
TPUh(10A)	2.75	3.21
TPUh(20A)	2.47	3.57
TPUs	–	–
TPUs(10A)	2.66	3.32
TPUs(20A)	2.55	3.46
Cloisite 10A	4.76	1.86
Cloisite 20A	3.56	2.48

trate the Cloisite 10A nanofiller plates to a more considerable degree. This is related to the higher interlayer spaces observed for this kind of nanoclay. According to the X-ray spectra of the polyurethanes modified by nanofillers, the resulting nanocomposites present an intercalated structure.

4. Conclusions

Polyurethane/OMMT nanocomposites were prepared by a two-step process using MDI, 1,4-BD, Polyol and modified MMT. The effect of the addition of 1% nanofiller (Cloisite 10A and Cloisite 20A) over the polyurethane matrix containing a different quantity of stiff segments was studied. The DSC results showed a slight increase of the melting temperature with Cloisite loading. For nanocomposites with a more elastic polyurethane matrix (TPUs), it was observed that the addition of organically modified aluminosilicates affected the rubbery region of the systems. The study of the mechanical strength shows a clear increase of this parameter after the application of a nanofiller to the polyurethane matrix. In the best case, a 43% higher stress at break was attained for TPUh(10A) respect to the mechanical resistance of TPUh. The systems containing nanofillers were observed to possess a higher viscosity compared to their unmodified equivalents. In part, this is an indicator of the degree of dispersion and the interaction of the nanofiller particles in the polyurethane matrix. The study of the thermal stability confirmed that the nanocomposites are thermally more stable than the unmodified systems. A non-significant better thermal stability was observed when the nanofiller Cloisite 20A was used. The X-ray analysis indicated exfoliation (for the Cloisite 10A nanoclay) and an intercalated structure in the nanocomposites containing Cloisite 20A. The obtained results confirm a higher compatibility of Cloisite 10A

with the polyurethane matrix in comparison with the other nanofiller introduced.

References

- [1] Azizi H., Morshedian J., Barikani M., Wagner M. H.: Effect of layered silicate nanoclay on the properties of silane crosslinked linear low-density polyethylene (LLDPE). *Express Polymer Letters*, **4**, 252–262 (2010). DOI: [10.3144/expresspolymlett.2010.32](https://doi.org/10.3144/expresspolymlett.2010.32)
- [2] Tyurin A., De Filipo G., Cupelli D., Nicoletta F. P., Mashin A., Chidichimo G.: Particle size tuning in silver-polyacrylonitrile nanocomposites. *Express Polymer Letters*, **4**, 71–78 (2010). DOI: [10.3144/expresspolymlett.2010.12](https://doi.org/10.3144/expresspolymlett.2010.12)
- [3] Samal S. K., Mohanty S., Nayak S. K.: Thermal, morphological and dynamic mechanical characterization of melt blended PC nanocomposites. *Advanced Materials Research*, **29–30**, 275–278 (2007). DOI: [10.4028/www.scientific.net/AMR.29-30.275](https://doi.org/10.4028/www.scientific.net/AMR.29-30.275)
- [4] Bieliński D., Rajkiewicz M., Mikołajska A., Majewski K.: Polymer nanocomposites – Selected domains of application (in Polish). *Elastomery*, **11**, 18–24 (2007).
- [5] Yasmin A., Abot J. L., Daniel I. M.: Processing of clay/epoxy nanocomposites by shear mixing. *Scripta Materialia*, **49**, 81–86 (2003). DOI: [10.1016/S1359-6462\(03\)00173-8](https://doi.org/10.1016/S1359-6462(03)00173-8)
- [6] Kim Y. C.: Effect of maleated polyethylene on the crystallization behavior of LLDPE/clay nanocomposites. *Polymer Journal*, **38**, 250–257 (2006). DOI: [10.1295/polymj.38.250](https://doi.org/10.1295/polymj.38.250)
- [7] García-López D., Picazo O., Merino J. C., Pastor J. M.: Polypropylene–clay nanocomposites: Effect of compatibilizing agents on clay dispersion. *European Polymer Journal*, **39**, 945–950 (2003). DOI: [10.1016/S0014-3057\(02\)00333-6](https://doi.org/10.1016/S0014-3057(02)00333-6)
- [8] Yano K., Usuki A., Okada A., Kurauchi T., Kamigaito O.: Synthesis and properties of polyimide–clay hybrid. *Journal of Polymer Science Part A: Polymer Chemistry*, **31**, 2493–2498 (1993). DOI: [10.1002/pola.1993.080311009](https://doi.org/10.1002/pola.1993.080311009)
- [9] Hagesawa N., Okamoto H., Kato M., Usuki A., Sato N.: Nylon 6/Na–montmorillonite nanocomposites prepared by compounding Nylon 6 with Na–montmorillonite slurry. *Polymer*, **44**, 2933–2937 (2003). DOI: [10.1016/S0032-3861\(03\)00215-5](https://doi.org/10.1016/S0032-3861(03)00215-5)
- [10] Zhou Q., Wang K., Loo L. S.: Abrasion studies of nylon 6/montmorillonite nanocomposites using scanning electron microscopy, fourier transform infrared spectroscopy, and X-ray photoelectron spectroscopy. *Journal of Applied Polymer Science*, **113**, 3286–3293 (2009). DOI: [10.1002/app.30229](https://doi.org/10.1002/app.30229)
- [11] Varghese S., Karger-Kocsis J.: Natural rubber-based nanocomposites by latex compounding with layered silicates. *Polymer*, **44**, 4921–4927 (2003). DOI: [10.1016/S0032-3861\(03\)00480-4](https://doi.org/10.1016/S0032-3861(03)00480-4)

- [12] Delozier D. M., Orwoll R. A., Cahoon J. F., Johnston N. J., Smith Jr. J. G., Conell J. W.: Preparation and characterization of polyimide/organoclay nanocomposites. *Polymer*, **43**, 813–822 (2002). DOI: [10.1016/S0032-3861\(01\)00640-1](https://doi.org/10.1016/S0032-3861(01)00640-1)
- [13] Fu X., Qutubuddin S.: Polymer–clay nanocomposites: Exfoliation of organophilic montmorillonite nanolayers in polystyrene. *Polymer*, **42**, 807–813 (2001). DOI: [10.1016/S0032-3861\(00\)00385-2](https://doi.org/10.1016/S0032-3861(00)00385-2)
- [14] Ma C-C. M., Chen Y-J., Kuan H-C.: Polystyrene nanocomposite materials: Preparation, morphology, and mechanical, electrical, and thermal properties. *Journal of Applied Polymer Science*, **98**, 2266–2273 (2005). DOI: [10.1002/app.22121](https://doi.org/10.1002/app.22121)
- [15] Jones W. E. Jr., Chiguma J., Johnson E., Pachamuthu A., Santos D.: Electrically and thermally conducting nanocomposites for electronic applications. *Materials*, **3**, 1478–1496 (2010). DOI: [10.3390/ma3021478](https://doi.org/10.3390/ma3021478)
- [16] Tomer V., Polizos G., Randall C. A., Manias E.: Polyethylene nanocomposite dielectrics: Implications of nanofiller orientation on high field properties and energy storage. *Journal of Applied Physic*, **109**, 074113/1–074113/11 (2011). DOI: [10.1063/1.3569696](https://doi.org/10.1063/1.3569696)
- [17] Tomer V., Polizos G., Manias E., Randall C. A.: Epoxy-based nanocomposites for electrical energy storage. I: Effects of montmorillonite and barium titanate nanofillers. *Journal of Applied Physic*, **108**, 074116/1–074116/14 (2010). DOI: [10.1063/1.3487275](https://doi.org/10.1063/1.3487275)
- [18] Koo J. H.: *Polymer nanocomposites: Processing, characterization, and applications*. McGraw-Hill, New York (2006).
- [19] Finnigan B., Martin D., Halley P., Truss R., Campbell K.: Morphology and properties of thermoplastic polyurethane nanocomposites incorporating hydrophilic layered silicates. *Polymer*, **45**, 2249–2260 (2004). DOI: [10.1016/j.polymer.2004.01.049](https://doi.org/10.1016/j.polymer.2004.01.049)
- [20] Kim J-Y., Jung W-C., Park K-Y., Suh K-D.: Synthesis of Na⁺-montmorillonite/amphiphilic polyurethane nanocomposite via bulk and coalescence emulsion polymerization. *Journal of Applied Polymer Science*, **89**, 3130–3136 (2003). DOI: [10.1002/app.12506](https://doi.org/10.1002/app.12506)
- [21] Janik J.: Effect of multiple processing on the properties of polypropylene nanocomposite (in Polish). *Przemysł Chemiczny*, **12**, 1694–1696 (2010).
- [22] Xiong J., Zheng Z., Jiang H., Ye S., Wang X.: Reinforcement of polyurethane composites with an organically modified montmorillonite. *Composites Part A: Applied Science and Manufacturing*, **38**, 132–137 (2007). DOI: [10.1016/j.compositesa.2006.01.014](https://doi.org/10.1016/j.compositesa.2006.01.014)
- [23] Tien Y. I., Wei K. H.: Hydrogen bonding and mechanical properties in segmented montmorillonite/polyurethane nanocomposites of different hard segment ratios. *Polymer*, **42**, 3213–3221 (2001). DOI: [10.1016/S0032-3861\(00\)00729-1](https://doi.org/10.1016/S0032-3861(00)00729-1)
- [24] Chen-Yang Y. W., Lee Y. K., Chen Y. T., Wu J. C.: High improvement in the properties of exfoliated PU/clay nanocomposites by the alternative swelling process. *Polymer*, **48**, 2969–2979 (2007). DOI: [10.1016/j.polymer.2007.03.024](https://doi.org/10.1016/j.polymer.2007.03.024)
- [25] Zhang X., Xu R., Wu Z., Zhou C.: The synthesis and characterization of polyurethane/clay nanocomposites. *Polymer International*, **52**, 790–794 (2003). DOI: [10.1002/pi.1152](https://doi.org/10.1002/pi.1152)
- [26] Stankowski M., Kropidłowska A., Gazda M., Haponiuk J. T.: Properties of polyamide 6 and thermoplastic polyurethane blends containing modified montmorillonites. *Journal of Thermal Analysis and Calorimetry*, **94**, 817–823 (2007). DOI: [10.1007/s10973-007-8886-x](https://doi.org/10.1007/s10973-007-8886-x)
- [27] Subramani S., Choi S-W., Lee J-Y., Kim H. J.: Aqueous dispersion of novel silylated (polyurethane-acrylic hybrid/clay) nanocomposite. *Polymer*, **48**, 4691–4703 (2007). DOI: [10.1016/j.polymer.2007.06.023](https://doi.org/10.1016/j.polymer.2007.06.023)
- [28] Cao X., Lee L. J., Widya T., Macosko C.: Polyurethane/clay nanocomposites foams: Processing, structure and properties. *Polymer*, **46**, 775–783 (2005). DOI: [10.1016/j.polymer.2004.11.028](https://doi.org/10.1016/j.polymer.2004.11.028)
- [29] Pegoretti A., Dorigato A., Brugnara M., Penati A.: Contact angle measurements as a tool to investigate the filler–matrix interactions in polyurethane–clay nanocomposites from blocked prepolymer. *European Polymer Journal*, **44**, 1662–1672 (2008). DOI: [10.1016/j.eurpolymj.2008.04.011](https://doi.org/10.1016/j.eurpolymj.2008.04.011)
- [30] Jang E. S., Khan S. B., Seo J., Nam Y. H., Choi W. J., Akhtar K., Han H.: Synthesis and characterization of novel UV-curable polyurethane–clay nanohybrid: Influence of organically modified layered silicates on the properties of polyurethane. *Progress in Organic Coatings*, **77**, 36–42 (2011). DOI: [10.1016/j.porgcoat.2010.12.007](https://doi.org/10.1016/j.porgcoat.2010.12.007)
- [31] Nigmatullin R., Gao F., Konovalova V.: Polymer-layered silicate nanocomposites in the design of antimicrobial materials. *Journal of Materials Science*, **43**, 5728–5733 (2008). DOI: [10.1007/s10853-008-2879-4](https://doi.org/10.1007/s10853-008-2879-4)
- [32] Khan S. B., Rahman M. M., Jang E. S., Akhtar K., Han H.: Special susceptible aqueous ammonia chemi-sensor: Extended applications of novel UV-curable polyurethane-clay nanohybrid. *Talanta*, **84**, 1005–1010 (2011). DOI: [10.1016/j.talanta.2011.02.036](https://doi.org/10.1016/j.talanta.2011.02.036)
- [33] Cervantes-Uc J. M., Moo Espinosa J. I., Cauich-Rodríguez J. V., Ávila-Ortega A., Vázquez-Torres H., Marcos-Fernández A., San Román J.: TGA/FTIR studies of segmented aliphatic polyurethanes and their nanocomposites prepared with commercial montmorillonites. *Polymer Degradation and Stability*, **94**, 1666–1677 (2009). DOI: [10.1016/j.polymdegradstab.2009.06.022](https://doi.org/10.1016/j.polymdegradstab.2009.06.022)

Biomimetic synthesis of poly(lactic-co-glycolic acid)/multi-walled carbon nanotubes/apatite composite membranes

H. L. Zhang*

College of Stomatology, Ningxia Medical University, 750004 Yinchuan, China

Received 23 November 2011; accepted in revised form 15 February 2012

Abstract. Bioactive guided tissue regeneration (GTR) membrane has had some success for periodontal therapy. In this study, poly(lactic-co-glycolic acid) (PLGA)/multi-walled carbon nanotubes (MWNTs) composite membranes were incubated in three supersaturated calcification solutions (SCS) of different pH values for 21 days to prepare a PLGA/MWNTs/apatite composite. Scanning electron microscope (SEM), X-ray diffraction (XRD), Fourier transform infrared spectroscopy (FTIR), energy dispersive spectroscopy (EDS), water contact angle measurement and mechanical testing were used for characterization. It was found that after 21 days incubation, apatite with low crystallite size and crystallinity was formed on the PLGA/MWNTs composite membranes. The Ca-poor carboxyapatite was similar in morphology and composition to that of natural bone. The size and shape of the apatite crystals immersed in three SCS were different from each other. The hydrophilicity and mechanical properties of the PLGA/MWNTs composite membranes were significantly enhanced after mineralization. This indicated that biomimetic mineralization may be an effective method to improve the biocompatibility and bone inductivity of certain materials. The PLGA/MWNTs/apatite composites may be potentially useful in GTR applications, particularly as GTR membranes for periodontal tissue regeneration.

Keywords: polymer composites, biomineralization, apatite crystal, GTR membrane

1. Introduction

Periodontitis is a common oral disease, which is the main reason for tooth loss in the adult world population. The ultimate goal of periodontal therapy is to restore the lost structure and function of the periodontal tissue, including the regeneration of periodontal membrane, cementum and alveolar bone. Traditional periodontal treatment can only control inflammation, but it is difficult to achieve the effect of regeneration. Therefore, how to regenerate the lost periodontal tissue has already become a key issue in periodontal therapy. However, the technique of guided tissue regeneration (GTR), proposed by Nyman *et al.* [1] in the early 1980s, has had some success. In this treatment technology, GTR

membrane is the key factor that directly affects the final restoration results.

An ideal GTR membrane should be biocompatible and biodegrade to nontoxic products within a specific time scale [2, 3]. It should be easy to fabricate with proper mechanical properties [4, 5] and present a penetrating structure [6, 7] that plays a role of blocking as well as transporting the nutrients and metabolic waste of the tissue [8, 9]. However, the GTR membranes currently in clinical use still have many problems, such as mechanical strength, degradation rate and the host immune response. Researchers apply a variety of new materials and new technologies to this area, trying to develop the membranes which meet the GTR requirements.

*Corresponding author, e-mail: hua31415926@163.com
© BME-PT

From the perspective of materials science, single material and single structure fail to meet the above requirements, therefore, the ideal GTR membrane should have multi-layer composite structure.

Poly(lactic-co-glycolic acid) (PLGA) and multi-walled carbon nanotubes (MWNTs) are two materials commonly used in tissue engineering. PLGA has attracted significant attention for its application in soft tissue engineering, bone tissue engineering, drug delivery, and nerve regeneration, due to its biocompatibility and biodegradability [10]. MWNTs have good biocompatibility when in contact with blood, bone, cartilage and soft tissue. Moreover, MWNTs have excellent biomedical properties, and can dramatically increase the mechanical properties of the composites [11, 12]. Therefore, they may both serve as candidates for GTR applications. However, PLGA has poor hydrophilicity for osteoprogenitor cellular vitality and specific cell interactions. Hydroxyapatite (HA), a major inorganic component of natural bone, on the other hand, exhibits good biocompatibility and osteoconductivity, which is generally suggested for effective acceleration of new bone formation [13, 14]. Therefore, HA coatings have been widely used in order to improve the biocompatibility and bone inductivity of the hydrophobic materials [15].

Mineralized composite membranes or scaffolds have been reported by many researchers by using different mineralization methods. Yang *et al.* [16] has reported mineralization of chitosan/MWNTs composite membranes by alternate soaking process and found that orientated nanoscopic crystallites of apatite were formed on the surface of the composites. However, this method needed to replace mineralization solutions every 12 h and the Ca/P molar ratio was ~2.6 to 3.0, which was rather a lot higher than that of stoichiometric hydroxyapatite (1.67). Corncob/HA scaffold has been fabricated by simulated body fluid (SBF) method by Ye *et al.* [17], but preparation of the mineralization solutions was somewhat complicated and time consuming. Supersaturated calcification solutions (SCS) method is an easy and effective way for preparing novel and bioactive composite materials [18]. Moreover, mineralization of PLGA/MWNTs composite membranes by SCS method has hardly been reported.

In this study, we are aiming at synthesizing the PLGA/MWNTs/apatite composites by biomimetic

mineralization, studying the formation of apatite on PLGA/MWNTs membranes, and evaluating various properties before and after mineralization, as a foundation for further study of the PLGA/MWNTs/apatite composites for GTR application.

2. Experimental

2.1. Materials

PLGA ($M_w = 100\ 000$ g/mol) with a lactide/glycolide ratio of 75:25 was purchased from Shandong Daigang Co. Ltd. (Jinan, China). MWNTs (diameter: 8–15 nm, length: 0.5 μm , purity >95 wt%) were purchased from Chengdu Organic Chemistry Co. Ltd. (Chengdu, China). Dimethyl formamide (DMF), trichloromethane (TCM) and other chemical reagents (A.R.) were purchased from Tianjin Chemical Reagent Co., Ltd. (Tianjin, China).

2.2. Preparation of PLGA/MWNTs composite membranes

PLGA/MWNTs composite membranes were prepared using the solution casting technique. Briefly, PLGA (2 g) was dissolved in a 20 mL mixture of TCM and DMF (volume ratio 7:3). MWNTs (0.1 g) were added to the PLGA solution and the mixture was then ultrasonicated for 1 h to disperse the MWNTs. The mixture was poured into a glass culture dish (diameter 12 cm) and placed in the ventilating cabinet for 48 h to evaporate the solvent, resulting in a membrane ~0.1 mm thick. All experiments were carried out in air and the ambient condition was 25°C and 60% humidity.

2.3. Mineralization of the composite membranes

In this study, three supersaturated calcification solutions (SCS) of different pH values (SCS1, SCS2 and SCS3) were selected for mineralization [18]. The ion concentrations and pH values of the three supersaturated calcification solutions are shown in Table 1. The composite membranes (22 mm \times 22 mm) were soaked in a freshly prepared saturated Ca(OH)₂ solution at room temperature for one hour first, and rinsed with distilled water. Then the membranes were divided into three groups, immersed in three different SCS respectively, and incubated at 37°C for 21 days to determine the mineralization behavior in vitro. The three SCS were replaced every 24 h. At the end of the incubation time, the samples

Table 1. The ion concentrations [mM/L] and pH values of the three supersaturated calcification solutions

	Na ⁺	Ca ²⁺	Cl ⁻	H ₂ PO ₄ ⁻	HCO ₃ ⁻	pH
SCS1	6.5	5	10	5	1.5	5.96
SCS2	4	5	10	2.5	1.5	6.31
SCS3	4	10	20	2.5	1.5	6.20

were rinsed with deionized water and then dried under vacuum at room temperature.

2.4. Characterization of composite membranes

The morphology of the samples was observed with SEM (JSM-7500F, JEOL, Japan). FTIR (Nicolet 560, Nicolet Co., USA) was used in the range from 4000 to 400 cm⁻¹ for the analysis of the crystals formed on the surface of the composites. Elemental analysis of the crystals was by EDS (JSM-7500F, JEOL, Japan). An X-ray diffractometer (SA-HF3, Rigaku, Japan) was used to investigate the mineral crystals grown on the surface of the membranes. The XRD was carried out with a Ni-filtered CuK α radiation source operated at a voltage of 40 kV and a current of 30 mA. The samples were scanned from 3 to 80° (2θ) and the scan rate was 8°/min. The wettability of the samples was determined by water contact angle measurement using JGW-360B (Midwest group, Beijing, China). Samples were placed on a sample stage and a single drop (20 μ L) of distilled water was dropped at three different places and the contact angle was then measured. The mechanical properties of the samples were analyzed using a universal testing machine (UTM, Instron 5567, USA) at room temperature. The extension rate was kept at 5 mm/min and the load cell used was 100 N with a gauge length of 25 mm. The dimensions of the samples were 10 mm \times 70 mm ($W \times L$) [19].

3. Results and discussion

3.1. Crystalline structure by XRD

The X-ray diffractogram of PLGA/MWNTs composite membranes, and the samples immersed in three different SCS for 21 days are shown in Figure 1. The XRD observations revealed that the PLGA/MWNTs composites were amorphous. The inorganic phase in the mineralized samples was determined as apatite crystals from the presence of several characteristic XRD diffraction peaks. It can

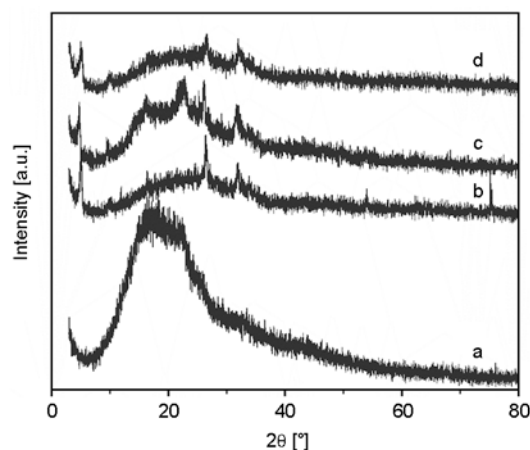


Figure 1. XRD patterns of (a) PLGA/MWNTs composite membranes, and PLGA/MWNTs composite membranes after immersion in (b) SCS1, (c) SCS2 and (d) SCS3 for 21 days

be seen that the samples immersed in SCS1, SCS2, and SCS3 all showed main diffraction peaks at $2\theta = 26$ and 32° , which were corresponded to planes 002 and 211 of HA. The samples immersed in SCS1 also showed the other peak at $2\theta = 54^\circ$, which was caused by the plane 004 of HA. However, the other diffraction peaks of HA were not found. Besides, the peaks of 211, 112 and 300 overlapped with each other without division, suggesting that the crystallinity of the apatite crystals was very low. Compared with JCPDS standard card of HA, the peaks of the apatite crystals in the mineralized samples became wider, which indicated that the crystallite size was tiny and the crystallinity was very low, closely resembling that of the natural bone tissue [20, 21]. Moreover, the diffraction peak at $2\theta = 26^\circ$ of apatite in group SCS1 was the highest and sharpest, followed by that in group SCS2 and then group SCS3, which may indicate that the sizes of the apatite crystals in three groups are in the same order.

Another notable feature was that the peak at $2\theta = 26^\circ$ (002) was higher and sharper than that at $2\theta = 32^\circ$ (211), indicating that the mineral crystals preferred orientation growth along the (002) surface of the C-axis of HA. HA is a hexagonal columnar crystal, and OH groups arranges in the C-axis or (002) plane. (002) direction is the preferred growth direction. The atoms accumulated along the (002) plane densely, which caused the formation of needle-like or lamellar appearance of the crystals. The mineral crystals grew along a certain axis, making

the overlap of some planes or defects of crystal growth, which also contributed to the lack of the other diffraction peaks of HA [22]. As C-axis of HA in natural bone tissue aligned along the collagen fibers, it has a certain significance to study how the organic matrix template controls the growth of apatite in biomimetic mineralization.

3.2. FTIR analysis of the mineral crystals and PLGA/MWNTs composite membranes

The apatite crystals were scraped off the surface of the PLGA/MWNTs composite membranes immersed in SCS2 for analysis by FTIR. The FTIR spectrum of the PLGA/MWNTs composite membranes was also presented for comparison. As shown in Figure 2, the FTIR spectrum of the apatite crystals showed characteristic PO_4^{3-} absorption bands at 1036, 603, and 566 cm^{-1} and O–H absorption band

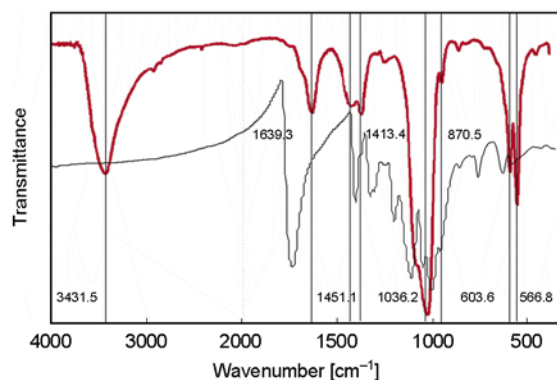
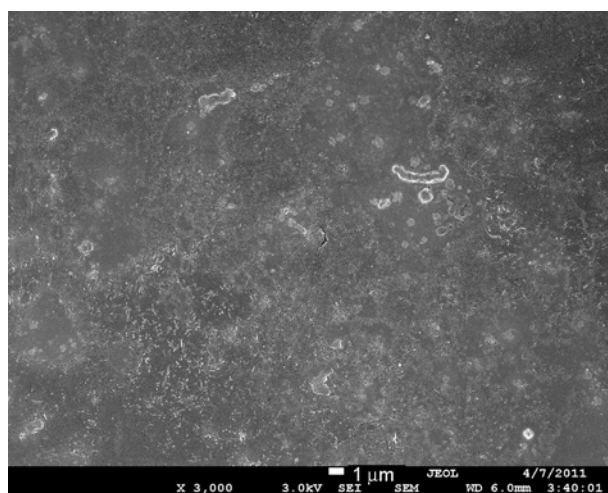
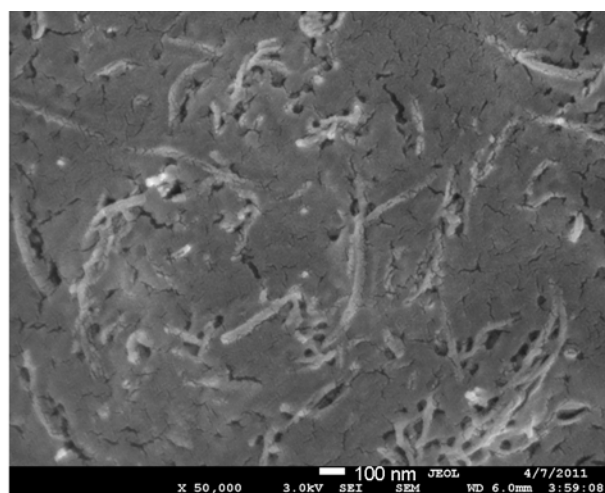


Figure 2. FTIR spectrum of the PLGA/MWNTs composite membranes (black) and the apatite crystals scraped off the surface of the PLGA/MWNTs composite membranes immersed in SCS2 for 21 days (red)



a)



b)

Figure 3. SEM images of PLGA/MWNTs composite membranes (a) at a magnification of 3000; (b) at a magnification of 50 000

around 3431 cm^{-1} . The difference of the PO_4^{3-} absorption bands between the apatite crystals grown on the surface of the composites and HA was that the absorption peak of the former around 1000 ~1100 cm^{-1} was not split, indicating a lower crystallinity of apatite coating. The CO_3^{2-} absorption bands appeared at 1451, 1413, and 870 cm^{-1} , indicating that CO_3^{2-} entered the crystal lattice structure of apatite. The apatite coating was composed of carbapatite, which was similar to the composition of HA in natural bone tissue.

3.3. Surface morphology by SEM

The SEM images of uncoated PLGA/MWNTs composite membranes are shown in Figure 3. It can be seen that the structure of the uncoated PLGA/MWNTs composite membranes was relatively well-proportioned and identical. There was no bubble or hole on the surface of the membranes. The SEM image taken at a higher magnification in Figure 3b reveals that MWNTs which were short tubular shaped were well dispersed and embedded in PLGA matrix, indicating that good alignment of MWNTs was achieved in PLGA matrix during the preparation of the composite membranes.

After 21 days of mineralization, the surfaces of the three samples were all covered by a layer of white mineralized crystals, but the mineral solutions still remained clear, indicating that heterogeneous nucleation occurred on the surfaces of the composite membranes [23, 24]. As shown in SEM images presented in Figure 4, the surfaces of all the PLGA/MWNTs composite membranes showed an obvious

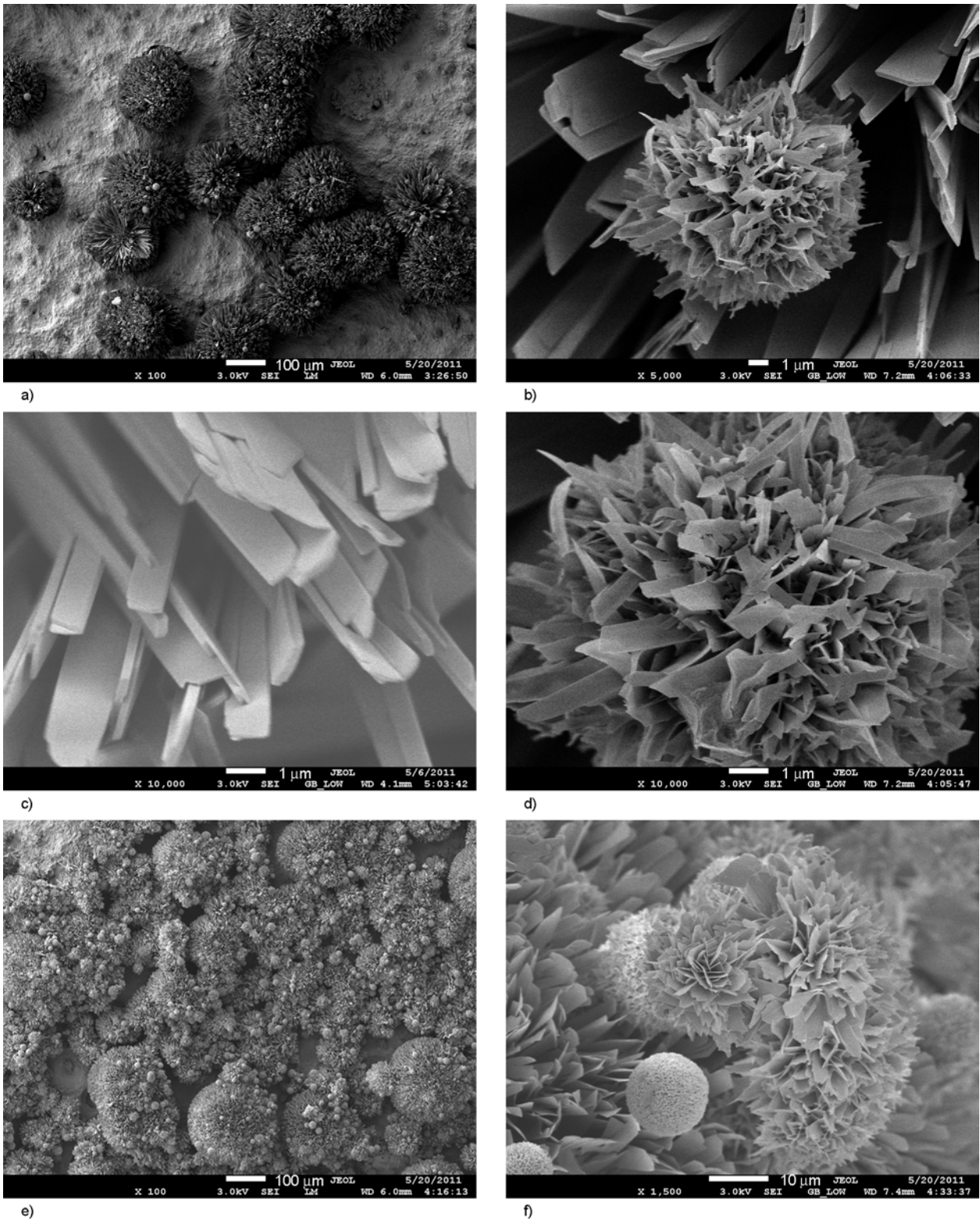


Figure 4. SEM images of PLGA/MWNTs composite membranes immersed in (a) (b) (c) (d) SCS1, (e) (f) (g) (h) SCS2, and (i) (j) (k) (l) SCS3 for 21 days (continued on next page)

change after mineralization. The apatite crystals clustered together regularly to form spherical particles on the surface of the composite membranes. However, the morphology of the crystals was

slightly different from each other due to the different ion concentrations and pH values of SCS. The SEM images taken at a higher magnification reveal that the flat quadrilateral-shaped single crystals at

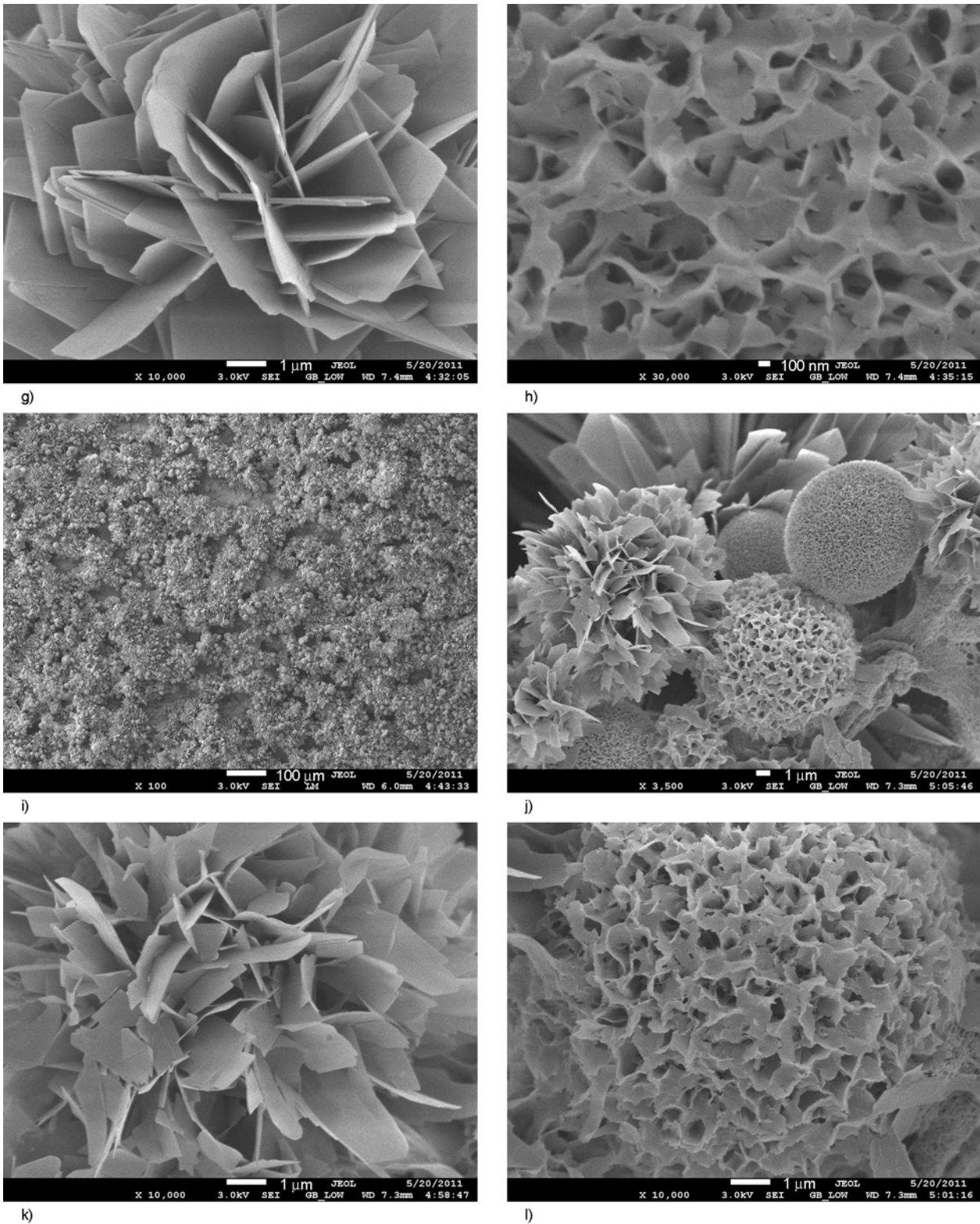


Figure 4. (continued from the previous page) SEM images of PLGA/MWNTs composite membranes immersed in (a) (b) (c) (d) SCS1, (e) (f) (g) (h) SCS2, and (i) (j) (k) (l) SCS3 for 21 days

the bottom layer, which formed from the original calcium and phosphorus deposits, interweave into a bundle. These crystals formed flowers-like shape and covered the entire surface of the matrix. Above

these crystals, it can be seen that tiny and slender quadrilateral-shaped crystals were formed in group SCS1, and leaf-shaped and honeycomb-shaped crystals were formed uniformly in group SCS2 and

SCS3, indicating that the crystals previously formed served as secondary nucleation sites for additional mineral formation. Besides, the amount of the apatite crystals in group SCS3 was the most, followed by that in group SCS2 and then group SCS1. Moreover, the size of the apatite crystals was the largest in group SCS1, followed by that in group SCS2 and then group SCS3, which also confirmed the results of XRD patterns. As for how the ion concentrations and pH values affect the size and shape of the crystals, further study is needed.

3.4. Elements analysis

EDS was used to analyze the type and proportion of elements of crystals. As shown in Figure 5, the evident presence of Ca and P peaks indicated the presence of HA on all the surfaces of the three samples. Table 2 shows the Ca/P molar ratios determined

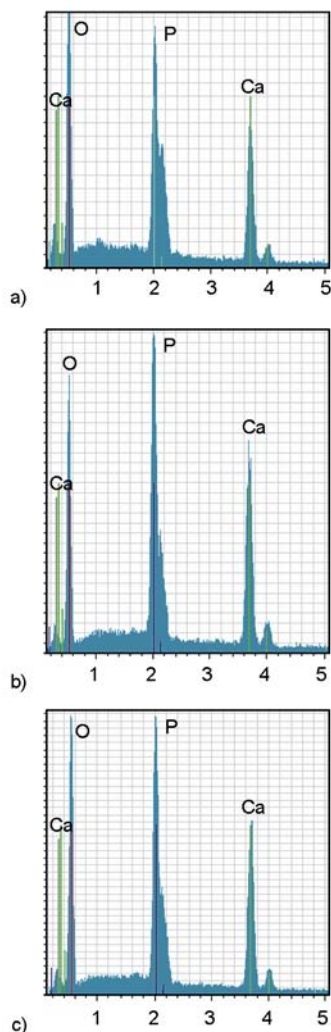


Figure 5. EDS scan results from the crystals of PLGA/MWNTs composite membranes immersed in (a) SCS1, (b) SCS2 and (c) SCS3 for 21 days

Table 2. Ca/p ratio of apatite on the surface of different samples

	Ca/P
SCS1	1.59
SCS2	1.43
SCS3	1.46

from EDS analysis. Ca/P molar ratios of the samples immersed in SCS1, SCS2 and SCS3 were 1.59, 1.43 and 1.46, respectively, which were all slightly lower than that of the chemical dose-HA (Ca/P = 1.67). Since the crystals contain carbonate ion substituted at phosphate ion lattice sites, therefore, the coatings are calcium-deficient-carbonated apatite and the apatite deposited on the surface of the composite membranes is Ca-poor apatite [25].

3.5. Wettability analysis

In this study, hydrophilicity of the surface of PLGA, PLGA/MWNTs, and the PLGA/MWNTs/apatite membranes immersed in SCS2 for 21 days was measured by water contact angle (Table 3). The contact angle of pure PLGA membrane was $117.5 \pm 3.6^\circ$, which clearly demonstrated the hydrophobic nature of PLGA surface. Addition of MWNTs into PLGA matrix did not change the hydrophobic nature of PLGA/MWNTs surface and the contact angle ($114.7 \pm 3.1^\circ$) was similar as that of the PLGA membrane. However, after mineralization, the surface of the PLGA/MWNTs/apatite membranes was completely hydrophilic (water contact angle 0°). Similar phenomenon was also observed by Lee *et al.* [26].

Table 3. Water contact angles of PLGA, PLGA/MWNTs and PLGA/MWNTs/apatite membranes immersed in SCS2 for 21 days

Sample name	Water contact angle [°]
PLGA	117.5 ± 3.6
PLGA/MWNTs	114.7 ± 3.1
PLGA/MWNTs/apatite	0

3.6. Mechanical characterization

Mechanical properties of PLGA, PLGA/MWNTs and PLGA/MWNTs/apatite membranes immersed in SCS2 for 21 days were shown in Table 4. Compared to the pure PLGA membrane, the mechanical properties of the PLGA/MWNTs membranes increased dramatically. The Young's modulus and

Table 4. Young's modulus, tensile stress and elongation at break of three membranes

Sample name	Young's modulus [MPa]	Tensile stress [MPa]	Elongation at break [%]
PLGA	152.0±16.6	5.43±0.62	36.8±4.69
PLGA/MWNTs	314.9±30.2	6.03±1.03	51.6±6.71
PLGA/MWNTs/apatite	382.4±34.4	7.73±0.95	11.2±2.17

tensile strength increased sharply by 107 and by 11%, respectively. The elongation at break was increased by 40%. It is evident that even a small amount of MWNTs would significantly improve the mechanical properties of the composites [17]. After mineralization, the Young's modulus and tensile strength of the PLGA/MWNTs/apatite membranes increased to 382.4±34.4 and 7.73±0.95 MPa, respectively. This may be due to increase in rigidity over the PLGA/MWNTs membranes after mineralization. However, the elongation at break decreased after mineralization, indicating that the PLGA/MWNTs/apatite composites became somewhat stiffer compared to PLGA/MWNTs membranes. The results of mechanical test indicated that the mechanical properties of the PLGA/MWNTs/apatite composites and PLGA/MWNTs composites were greatly improved compared to the pure PLGA membrane.

4. Conclusions

Apatite crystals were coated on the surface of the PLGA/MWNTs composite membranes after immersion in SCS for 21 days, suggesting that the PLGA/MWNTs composites have good biomineralization performance in vitro and it is feasible to prepare biomimetic materials for GTR by this method. The formed apatite with low crystallite size and crystallinity was Ca-poor carboxyapatite, which was similar in composition and structure to that of natural bone. The size and shape of the apatite crystals immersed in three SCS of different ion concentrations and pH values were different from each other, indicating that we may control the size and shape of the crystals through regulating the composition of the mineral solution. The PLGA/MWNTs membranes showed improved hydrophilicity and mechanical strength after mineralization. These novel PLGA/MWNTs/apatite composites with controlled macroscale and microscale configuration are expected to be a promising bioactive GTR membrane for periodontal tissue regeneration.

Acknowledgements

This work was supported by the Key Project of Ministry of Education of China (grant number: 211196), Natural Science Foundation of NingXia, China (grant number: NZ11124) and the School Program of Ningxia Medical University (grant number: XT201006).

References

- [1] Nyman S., Lindhe J., Karring T., Rylander H.: New attachment following surgical treatment of human periodontal disease. *Journal of Clinical Periodontology*, **9**, 290–296 (1982).
DOI: [10.1111/j.1600-051X.1982.tb02095.x](https://doi.org/10.1111/j.1600-051X.1982.tb02095.x)
- [2] Brekke J. H., Toth J. M.: Principles of tissue engineering applied to programmable osteogenesis. *Journal of Biomedical Materials Research*, **43**, 380–398 (1998).
DOI: [10.1002/\(SICI\)1097-4636\(199824\)43:4<380::AID-JBM6>3.0.CO;2-D](https://doi.org/10.1002/(SICI)1097-4636(199824)43:4<380::AID-JBM6>3.0.CO;2-D)
- [3] Gunatillake P. A., Adhikari R.: Biodegradable synthetic polymer for tissue engineering. *European Cells and Materials*, **5**, 1–16 (2003).
- [4] Lin A. S. P., Barrows T. H., Cartmell S. H., Gulberg R. E.: Microarchitectural and mechanical characterization of oriented porous polymer scaffolds. *Biomaterials*, **24**, 481–489 (2003).
DOI: [10.1016/S0142-9612\(02\)00361-7](https://doi.org/10.1016/S0142-9612(02)00361-7)
- [5] Kokubo T., Kim H-M., Kawashita M.: Novel bioactive materials with different mechanical properties. *Biomaterials*, **24**, 2161–2175 (2003).
DOI: [10.1016/S0142-9612\(03\)00044-9](https://doi.org/10.1016/S0142-9612(03)00044-9)
- [6] Li S., de Wijn J. R., Li J. P., Layrolle P., de Groot K.: Macroporous biphasic calcium phosphate scaffold with high permeability/porosity ratio. *Tissue Engineering*, **9**, 535–548 (2003).
DOI: [10.1089/107632703322066714](https://doi.org/10.1089/107632703322066714)
- [7] Deschamps A. A., Claase M. B., Sleijster W. J., de Bruijn J. D., Grijpma D. W., Feijen J.: Design of segmented poly(ether ester) materials and structures for the tissue engineering of bone. *Journal of Controlled Release*, **78**, 175–186 (2002).
DOI: [10.1016/S0168-3659\(01\)00497-7](https://doi.org/10.1016/S0168-3659(01)00497-7)
- [8] Chen Y., Mak A. F. T., Wang M., Li J., Wong M. S.: PLLA scaffolds with biomimetic apatite coating and biomimetic apatite/collagen composite coating to enhance osteoblast-like cells attachment and activity. *Surface and Coatings Technology*, **201**, 575–580 (2006).
DOI: [10.1016/j.surfcoat.2005.12.005](https://doi.org/10.1016/j.surfcoat.2005.12.005)

- [9] Goldstein A. S., Zhu G., Morris G. E., Meszlenyi R. K., Mikos A. G.: Effect of osteoblastic culture conditions on the structure of poly(DL-lactic-co-glycolic acid) foam scaffolds. *Tissue Engineering*, **5**, 421–433 (1999).
DOI: [10.1089/ten.1999.5.421](https://doi.org/10.1089/ten.1999.5.421)
- [10] Zhang H. L., Chen Z. Q.: Fabrication and characterization of electrospun PLGA/MWNTs/ hydroxyapatite biocomposite scaffolds for bone tissue engineering. *Journal of Bioactive and Compatible Polymers*, **25**, 241–259 (2010).
DOI: [10.1177/0883911509359486](https://doi.org/10.1177/0883911509359486)
- [11] Cao X., Dong H., Li C. M., Lucia L. A.: The enhanced mechanical properties of a covalently bound chitosan-multiwalled carbon nanotube nanocomposite. *Journal of Applied Polymer Science*, **113**, 466–472 (2009).
DOI: [10.1002/app.29984](https://doi.org/10.1002/app.29984)
- [12] Curtin W. A., Heldon B. W.: CNT-reinforced ceramics and metals. *Materials Today*, **11**, 44–49 (2004).
DOI: [10.1016/S1369-7021\(04\)00508-5](https://doi.org/10.1016/S1369-7021(04)00508-5)
- [13] Sheikh F. A., Kanjwal M. A., Macossay J., Barakat N. A. M., Kim H. Y.: A simple approach for synthesis, characterization and bioactivity of bovine bones to fabricate the polyurethane nanofiber containing hydroxyapatite nanoparticles. *Express Polymer Letters*, **6**, 41–53 (2012).
DOI: [10.3144/expresspolymlett.2012.5](https://doi.org/10.3144/expresspolymlett.2012.5)
- [14] Tan Q., Zhang K., Gu S., Ren J.: Mineralization of surfactant functionalized multi-walled carbon nanotubes (MWNTs) to prepare hydroxyapatite/MWNTs nanohybrid. *Applied Surface Science*, **255**, 7036–7039 (2009).
DOI: [10.1016/j.apsusc.2009.03.036](https://doi.org/10.1016/j.apsusc.2009.03.036)
- [15] Fathi M. H., Azam F.: Novel hydroxyapatite/tantalum surface coating for metallic dental implant. *Materials Letters*, **61**, 1238–1241 (2007).
DOI: [10.1016/j.matlet.2006.07.013](https://doi.org/10.1016/j.matlet.2006.07.013)
- [16] Yang J., Yao Z., Tang C., Darvell B. W., Zhang H., Pan L., Liu J., Chen Z.: Growth of apatite on chitosan-multiwall carbon nanotube composite membranes. *Applied Surface Science*, **255**, 8551–8555 (2009).
DOI: [10.1016/j.apsusc.2009.06.013](https://doi.org/10.1016/j.apsusc.2009.06.013)
- [17] Ye Y-M., Huang C-P., Wang Q., Li Q-L., Chen Z-Q., Bao C-Y.: Biomimetic synthesis of a novel HA/corn-cob composite. *Applied Surface Science*, **255**, 548–551 (2008).
DOI: [10.1016/j.apsusc.2008.06.056](https://doi.org/10.1016/j.apsusc.2008.06.056)
- [18] Li F., Feng Q. L., Cui F. Z., Li H. D., Schubert H.: A simple biomimetic method for calcium phosphate coating. *Surface and Coatings Technology*, **154**, 88–93 (2002).
DOI: [10.1016/S0257-8972\(01\)01710-8](https://doi.org/10.1016/S0257-8972(01)01710-8)
- [19] Zhang H.: Electrospun poly (lactic-co-glycolic acid)/multiwalled carbon nanotubes composite scaffolds for guided bone tissue regeneration. *Journal of Bioactive and Compatible Polymers*, **26**, 347–362 (2011).
DOI: [10.1177/0883911511413450](https://doi.org/10.1177/0883911511413450)
- [20] Varma H. K., Yokogawa Y., Espinosa F. F., Kawamoto Y., Nishizawa K., Nagata F., Kameyama T.: Porous calcium phosphate coating over phosphorylated chitosan film by a biomimetic method. *Biomaterials*, **20**, 879–884 (1999).
DOI: [10.1016/S0142-9612\(98\)00243-9](https://doi.org/10.1016/S0142-9612(98)00243-9)
- [21] Yang C. R., Wang Y. J., Chen X. F., Zhao N. R.: Biomimetic fabrication of BCP/COL/HCA scaffolds for bone tissue engineering. *Materials Letters*, **59**, 3635–3640 (2005).
DOI: [10.1016/j.matlet.2005.07.022](https://doi.org/10.1016/j.matlet.2005.07.022)
- [22] Varma H. K., Yokogawa Y., Espinosa F. F., Kawamoto Y., Nishizawa K., Nagata F., Kameyama T.: In-vitro calcium phosphate growth over functionalized cotton fibers. *Journal of Materials Science: Materials in Medicine*, **10**, 395–400 (1999).
DOI: [10.1023/A:1008970913107](https://doi.org/10.1023/A:1008970913107)
- [23] Jakobsen R. J., Brown L. L., Hutson T. B., Fink D. J., Veis A.: Intermolecular interactions in collagen self-assembly as revealed by Fourier transform infrared spectroscopy. *Science*, **220**, 1288–1290 (1983).
DOI: [10.1126/science.6857249](https://doi.org/10.1126/science.6857249)
- [24] Linde A.: Dentin mineralization and the role of odontoblasts in calcium transport. *Connective Tissue Research*, **33**, 163–170 (1995).
DOI: [10.3109/03008209509016997](https://doi.org/10.3109/03008209509016997)
- [25] Li L., Li G., Wang Y., Jiang J.: Apatite formation on poly (vinyl alcohol)-coated poly (ϵ -caprolactone) films by incubation in simulated body fluids. *Applied Surface Science*, **255**, 7734–7738 (2009).
DOI: [10.1016/j.apsusc.2009.04.154](https://doi.org/10.1016/j.apsusc.2009.04.154)
- [26] Lee J. H., Rim N. G., Jung H. S., Shin H.: Control of osteogenic differentiation and mineralization of human mesenchymal stem cells on composite nanofibers containing poly[lactic-co-(glycolic acid)] and hydroxyapatite. *Macromolecular Bioscience*, **10**, 173–182 (2010).
DOI: [10.1002/mabi.200900169](https://doi.org/10.1002/mabi.200900169)

Rod like attapulgite/poly(ethylene terephthalate) nanocomposites with chemical bonding between the polymer chain and the filler

L. Chen, K. Liu, T. X. Jin, F. Chen, Q. Fu*

Department of Polymer Science and Materials, State Key Laboratory of Polymer Materials Engineering, Sichuan University, 610065 Chengdu, China

Received 7 December 2011; accepted in revised form 16 February 2012

Abstract. Poly(ethylene terephthalate) (PET) nanocomposites containing rod-like silicate attapulgite (AT) were prepared via *in situ* polymerization. It is presented that PET chains identical to the matrix have been successfully grafted onto simple organically pre-modified AT nanorods (MAT) surface during the *in situ* polymerization process. The covalent bonding at the interface was confirmed by Fourier transform infrared spectroscopy (FTIR) and thermogravimetric analysis (TGA). The content of grafted PET polymer on the surface of MAT was about 26 wt%. This high grafting density greatly improved the dispersion of fillers, interfacial adhesion as well as the significant confinement of the segmental motion of PET, as compared to the nanocomposites of PET/pristine AT (PET/AT). Owing to the unique interfacial structure in PET/MAT composites, their thermal and mechanical properties have been greatly improved. Compared with neat PET, the elastic modulus and the yield strength of PET/MAT were significantly improved by about 39.5 and 36.8%, respectively, by incorporating only 2 wt % MAT. Our work provides a novel route to fabricate advanced PET nanocomposites using rod-like attapulgite as fillers, which has great potential for industrial applications.

Keywords: polymer composites, poly(ethylene terephthalate), attapulgite, interfacial structure, mechanical property

1. Introduction

Poly(ethylene terephthalate) (PET) is a semicrystalline polymer with excellent chemical resistance, thermal stability, and spinnability. Due to its low cost and high performance, PET is in widespread use in our modern life, ranging from textile fibers, films, bottles containers and food packaging materials to engineering plastics, etc. However, numerous shortcomings such as low rate of crystallization, long cycle times for injection moulding, low melt strength and low distortion temperature limit its application [1, 2]. To meet the practical needs and improve its performance, the addition of inorganic filler into PET matrix has been a research focus, and dramatic enhancements in properties such as

their mechanical, gas barrier property and thermal property can be achieved [3–13]. These enhancements result from homogeneous dispersion of nanoparticles in polymer matrix and the interaction between the nanoparticles and PET matrix. The *in situ* polymerization technique is particularly attractive, which enables to exercise control over both the polymer architecture and the final structure of the composites.

Recently various nanoparticles have been applied in the preparation of PET nanohybrids via *in situ* polymerization or melt mixing, including layered silicates montmorillonite (MMT) [3–6], spherical silica [7, 8], carbon nanotube [9–11] and so on. Specially, PET/layered clay composites have attracted much

*Corresponding author, e-mail: qiangfu@scu.edu.cn
© BME-PT

attention. However, intercalation technology used in preparing PET/MMT composites makes the polymerization process complicated and expensive. Moreover, obtaining high exfoliation level of MMT in PET matrix still remains a great challenge.

Attapulgite (AT) is a crystalloid, hydrous magnesium-aluminum silicate mineral, which is received as a randomly oriented network of densely packed rods. A fibrillar single crystal is the structural unit, with 20–30 nm in diameter and 0.5–2.0 μm in length [14–16]. Owing to the low price, relatively high surface area, good mechanical strength and thermal stability, AT is attracting more and more attention in the preparation of polymer/clay composites [17–20]. The preparation of PET/AT has been also explored, and a silylation modification of AT was carried out via the reaction of silane coupling agents with the silanol groups on AT surface [21, 22]. In this route, the pre-modification was complicated and the improvement of mechanical properties was limited, moreover, the thermal stability of organic modifier must be taken into consideration.

In this work, we present a novel way to prepare PET composites using rod-like AT as filler, in which AT was first acid treated to produce more silanol groups on its surface, then 4, 4'-methylenebis(phenyl isocyanate) (MDI) was grafted on AT surface. Nanorods of raw AT and MDI modified AT (MAT) were incorporated into the PET matrix by *in situ* polymerization. It was assumed that during the *in situ* polymerization process, the high reactivity isocyanate groups on MAT surface can react with ethylene glycol followed by PET chain growth, resulting in the formation of PET chains identical to the polymer matrix grafted on MAT nanorods surface. It is demonstrated that PET chains are linked on MAT surface through covalent bond, which improves the dispersion and interface adhesion between MAT and PET matrices, leading to a greatly improvement of PET properties.

2. Experimental section

2.1. Materials

Attapulgite clay (purity greater than 95%, specific surface area 400–500 m^2/g) was supplied by Autobang International Co. (Xuyi County, Jiangsu, China). Terephthalic acid (TPA), 4, 4'-methylenebis(phenyl isocyanate) (MDI) were purchased from

commercial sources. Ethylene glycol (EG), Sb_2O_3 , triphenyl phosphite (TPP), hydrochloric acid, acetone, phenol, tetrachloroethane, trifluoroacetic acid, and dichloromethane were purchased from Kelong Co. (Chengdu, China), all reagents were used as received.

2.2. Functionalization of AT nanorod

AT nanorod was firstly activated for 1 h in 5 M HCl solution at 80°C to introduce more active hydroxyl groups on the surface. After exhaustive washing with deionized water to pH neutrality, the activated nanorod was dried and ground. Then it was re-dispersed it in dry acetone to form a 5 wt% suspension, excess MDI was added to the suspension with vigorous stirring and ultrasonic treatment. The mixture was refluxed at 80°C for 1 h to complete the reaction between isocyanate and hydroxyl groups. The grafted nanorod was centrifuged at 4000 rpm, and washed for 4–5 times with acetone to completely remove ungrafted MDI, then dried in a vacuum oven at 70°C *in vacuo* for 24 h. The dried cake was ground and screened through a 200 mesh sieve to obtain MDI grafted nanorod (MAT).

2.3. Preparation of PET composites

PET/AT and PET/MAT composites were prepared by *in situ* polymerization. A given amount of MAT was first mixed with EG (124 mL, 2.25 mol). Then the suspension was poured into a home-made autoclave together with TPA (249 g, 1.5 mol), Sb_2O_3 and TPP (Sb_2O_3 as catalyst, TPP as stabilizer). With stirring, the temperature was gradually increased to 100°C, kept at this temperature for 30 min to let the remaining high reactivity isocyanate groups on MAT surface react with hydroxyl group of EG. Then the mixture was heated under reflux for 2 h at 230°C for direct esterification. After excess EG and water were distilled off, the mixture was heated to 280°C for condensation polymerization. The production was extruded from the autoclave by compressed nitrogen and cut into pellets. The pure PET and PET/AT were also prepared by the same method. PET composites with 1, 2 wt% AT and 1, 2 wt% MAT loading were labeled PET/1AT, PET/2AT, PET/1MAT and PET/2MAT, respectively. Finally, samples for mechanical test were obtained by melt-pressing the pellets at 265°C and 5.0–8.0 MPa

between two iron flats using a hot-press, followed by quenching into ice-water to obtain a film without crystallization.

To investigate the interfacial structure and to estimate the grafting yield of PET/MAT, successive centrifugation/redissolution cycles [7] were employed to separate the nanorod from physically absorbed polymer. PET/2MAT (30 g) were dissolved in 150 mL mixture of phenol and tetrachloroethane (1/1, w/w). The solution was centrifuged at 11 000 rpm for 30 min, redissolved the obtained centrifugate in the above mixed solvent, and then separated again by centrifugation. This centrifugation/redissolution procedure was repeated 5 times. The resulting solid materials were washed extensively with ethanol to remove the solvent and dried at 80°C under vacuum for 24 h. AT was also separated from PET/2AT composites by the same procedure. The filler from PET/2MAT and PET/2AT was labeled IS-MAT and IS-AT, respectively.

2.4. Characterization

The intrinsic viscosity ($[\eta]$) was determined at 25°C in an Ubbelohde viscometer with the mixture of 50/50 (wt/wt) phenol/1,1,2,2-tetrachloroethane as solvent. Prior to intrinsic viscosity test, the solution was filtered to remove the small amount of insoluble components.

FTIR was employed to characterize chemical structure of various nanorod. The sample was coated on a KBr plate, and the spectra were recorded between 400 and 4000 cm^{-1} on a Nicolet-560 FTIR spectrometer. The thermal stability was studied by Thermal gravimetric analysis (TGA) test, conducted at WRT-2P Shanghai Scale Factory, from 50 to 800°C at nitrogen atmosphere with the heating of 20°C/min. For SEM investigation, PET nanocomposites samples were cryo-fractured in liquid nitrogen and investigated on an Inspect SEM instrument (FEI) with an acceleration voltage of 20 kV.

The thermal analysis of the samples was conducted using a PerkinElmer DSC Pyris-1. Under nitrogen atmosphere, the samples of about 5.0 mg were heated from room temperature to 300°C and held for 5 min to eliminate the thermal history, then cooled down to 30°C and heated again at the rate of 10°C/min.

Dynamic Mechanical Analysis (DMA) test were conducted on a TA Company Q800, in tensile mode. Tests were performed at a frequency of 1 Hz with a

temperature sweep from 40 to 120°C at a ramp rate of 3°C/min. Static force of 0.01 N, 25.0 μm of setting amplitude, 135% of force track were applied to the samples with size of on samples 15.3 mm \times 5.5 mm \times 0.4 mm. A total of 3 tests were performed for each batch of material. Tensile tests were performed using an universal tensile testing machine (Instron 4302, USA) equipped with a 500 N load cell, with a cross-head speed of 10 mm/min at 23°C. The tensile samples were cut from the hot-pressed films, with dimensions of 50 \times 5 \times 0.4 mm. At least five samples were used for each measurement and the reported stress-strain curves below represent an average result.

3. Results and discussion

3.1. The interaction between PET and attapulgite

It is well known that the enhanced performance of polymer/clay nanocomposites originate from the nanoscale dispersion of these inorganic fillers and the interaction between fillers and polymer matrix. AT is highly anisotropic clay which is typically agglomerated in the as-received condition, thus appropriate organic modification is a crucial point in the design and preparation of polymer/AT nanocomposites. In this work, an aromatic diisocyanate (MDI) was used to capture hydroxyl groups on AT surface, and then the MDI-grafted AT (MAT) were introduced to the PET matrix via *in situ* polymerization. This AT organic modification and composites synthesis process allows PET chains get linked on the MAT nanorod surface forming a novel polymer grafting interface structures, which can be confirmed by FTIR spectroscopy, TGA test and sedimentation experiment as discussed below.

Figure 1 shows the FT-IR spectra of neat PET, AT, IS-AT, MAT and IS-MAT. The spectrum for the original AT (Figure 1b) reveals characteristic absorption bands at 3500 cm^{-1} (from O–H stretching) and 1030 cm^{-1} (for Si–O in-plane stretching). There is no much difference between spectra of raw AT and IS-AT (Figure 1c), except that there is a weak band at 1720 cm^{-1} that is attributed to the stretching resonance of PET carbonyl groups (Figure 1a), which indicates that there is still a little physically absorbed PET on AT surface that cannot be removed completely. While, in comparison with the spectrum of raw AT, the characteristic absorption for isocyanate

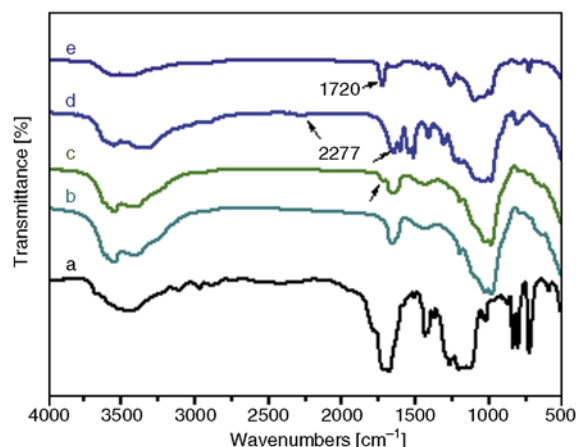


Figure 1. FTIR spectra for the (a) neat PET, (b) pristine AT, (c) IS-AT (AT isolated from PET/2AT nanocomposites), (d) MAT, and (e) IS-MAT (AT isolated from PET/2MAT nanocomposites)

groups at 2277 cm^{-1} is clearly identified in the spectrum of MAT (Figure 1d); urethane bands at 1648 , 1511 , and 1309 cm^{-1} , assigned to CO (urethane I), NH (urethane II), and CNH (urethane III), respectively, are also clearly identified. These characteristic bands indicate a covalent link between the isocyanate molecules and the AT. For the FTIR spectra of IS-MAT (Figure 1e), the characteristic absorption of C=O stretching vibration in the ester carbonyl group at 1720 cm^{-1} is very strong compared with Figure 1b, the bands at 1579 , 1409 and 729 cm^{-1} are due to in-plane and out-of-plane vibrations of the benzene rings, and the bands around 1263 and 1100 cm^{-1} result from vibrations of the ester group (Figure 1a). Since both IS-MAT and IS-AT are prepared by the same procedure, these results verified that some PET molecules had been grafted onto MAT surface through chemical bonding rather than physical absorption. The proposed mechanism for the grafting polymerization is illustrated in Figure 2.

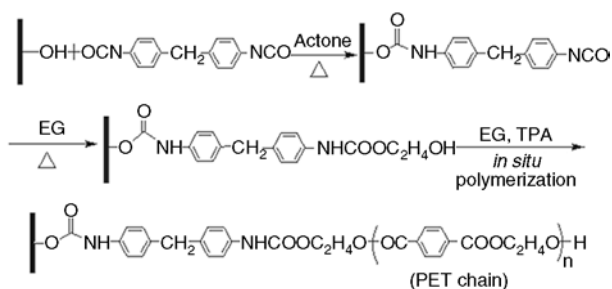


Figure 2. The reaction route of surface functionalization of AT and synthesis of PET nanocomposites by *in situ* polymerization in the presence of MAT nanorod

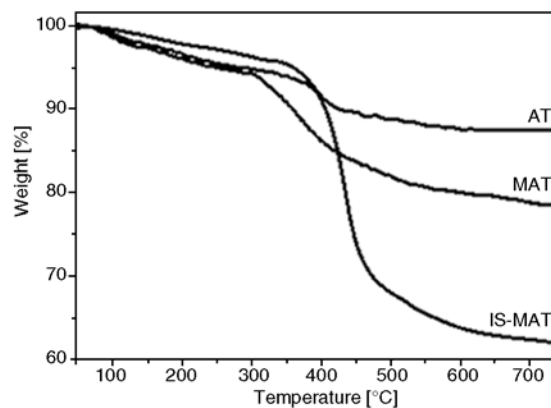


Figure 3. TGA curves of as-received AT; surface grafting with MDI (MAT); isolated nanorods from PET/2MAT composites (IS-MAT)

The amount of diisocyanate and PET polymer chains grafted onto the AT surface has been determined by thermogravimetric analysis (TGA) test. The weight loss curves for AT and MAT are presented in Figure 3. By extracting the mass loss of AT, we can calculate the mass fraction of organic component. Analysis of the curves indicates that 8.9 wt% (relative to the weight of dry original nanoparticles) of the MDI molecules has been grafted onto the surface of the nanorod, and about 26 wt% PET polymer has been grafted on MAT during the *in situ* polymerization. Compared with the amount of grafted MDI mass, the grafting PET polymer mass is relatively low, that may because the covalent graft PET chains on the surface of nanorod decreases the mobility of reactive end-groups, which reduces the opportunity to react in the polycondensation process and results in low molecular weight of grafted PET chains [7]. The aromatic structure of the grafting molecules makes the MAT exhibiting a higher onset temperature of thermal decomposition (near 300°C). This is necessary for the *in situ* preparation of PET nanocomposites which is carried out at high temperature (280°C) [4, 23].

Finally, the evidence for improved dispersion of MAT in PET matrix and the interfacial bonding between the MAT and the PET can be further proved by examining the freeze-fractured cross-sections surfaces of PET/2AT and PET/2MAT composite. Figures 4a, 4b show the fracture surfaces of the PET composites loaded with 2 wt% raw AT, the nonuniform dispersion of AT that agglomerated massively in bundles in PET matrix can be clearly observed. Due to the lack of strong bonds holding

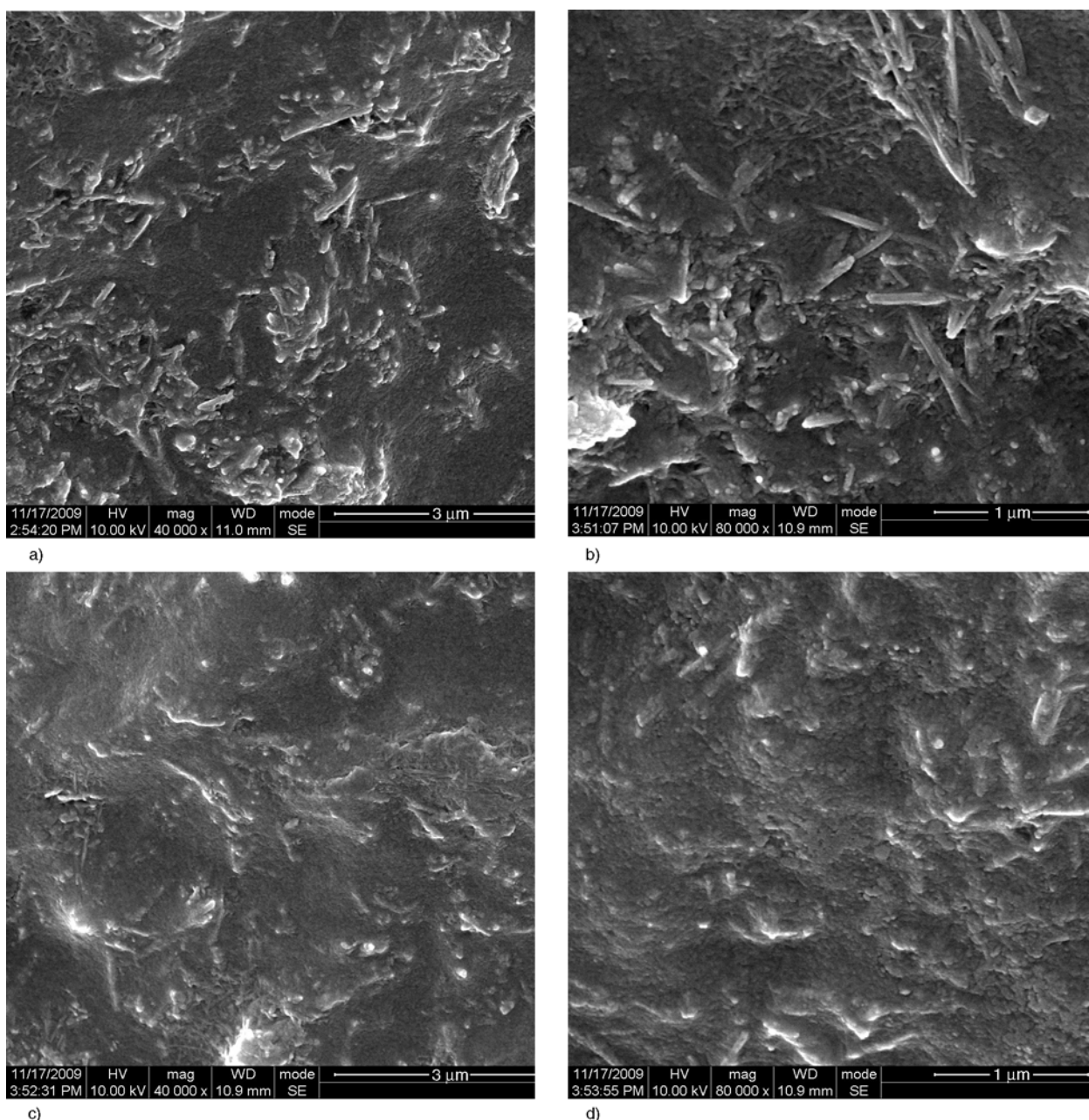


Figure 4. SEM images of (a, b) PET/AT, (c, d) PET/MAT nanocomposites with 2 wt% nanorods loading, scale bar is 3 μm and 1 μm , respectively

the PET polymer at the AT surface, many debonded AT nanorods are visible at the amplified image (Figure 4b). In contrast to pristine AT, MAT can be homogeneously dispersed in PET matrix that individual MAT can be easily identified without aggregation, and the interfacial boundary between MAT and PET matrix is nearly indiscernible as shown in Figures 4c, 4d, suggesting that their surfaces are most likely coated by a layer of PET polymer. It can be demonstrated from SEM images that the polymer covalently grafted PET/MAT composites dramatically improve the nanorod dispersion and greatly

enhance the interfacial adhesion between the nanorod and PET matrix.

3.2. Thermal properties

Generally, the introduction of inorganic fillers into polymer matrices can improve the thermal stability of polymer. The decomposition temperatures measured at 5% (T_d) and residues at 600°C (R_c) are summarized in Table 1, which indicates a moderate increase in the thermal stability of the nanocomposites. The thermal decomposition (T_d) of the PET nanocomposites were 3–7°C higher than that of

Table 1. Thermal properties of neat PET and PET nanocomposites

Sample	η_0 [dL/g]	η^* [dL/g]	T_g [°C]	T_c [°C]	T_m (°C)	T_d [°C]	R_c [650°C, wt%]
NPET	0.73	0.61	81.1	182	247	404.7	11.4
PET/1AT	0.69	0.54	83.0	190	246	407.8	14.2
PET/2AT	0.74	0.56	83.3	192	246	410.2	14.9
PET/1MAT	0.73	0.60	85.6	194	249	409.4	15.7
PET/2MAT	0.70	0.62	86.1	197	251	412.0	17.3

η_0 , η^* represent intrinsic viscosity of neat PET and PET/AT composites before and after hot-pressing respectively; T_g values were obtained from dynamic mechanical analysis (DMA); T_c and T_m values were obtained from differential scanning calorimetry (DSC) tests.

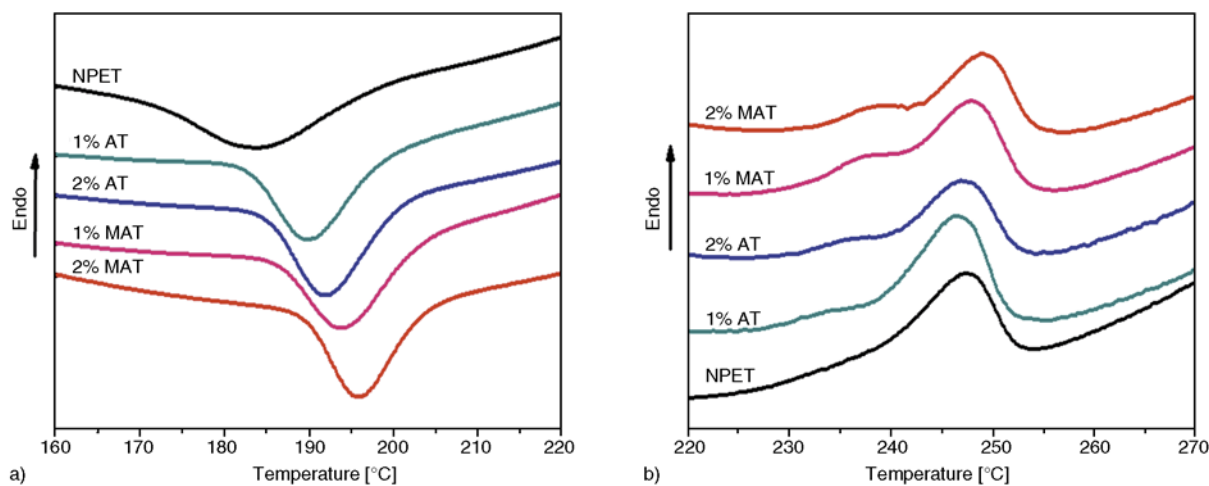
neat PET, the residue content of the PET nanocomposites at 600°C is larger than that of neat PET, and the greater the clay content is, the larger the residue content is. Compared with PET/AT, PET/MAT composites have enhanced thermal stability. The particle-matrix interfacial interaction and ‘barrier effect’, which limits volatilization of products and thermal transport during polymers decomposition, have been suggested as the two main reasons for the improved thermal stability in polymer nanocomposites [20]. Therefore, it is reasonable to assume that the better dispersion and stronger interfacial interaction for PET/MAT result in the enhanced thermal stability of PET/MAT, as compared with the neat PET and PET/AT.

The thermal stability was also investigated by comparing the change of intrinsic viscosity for neat PET, PET/AT and PET/MAT during hot-press forming. As shown in Table 1, an obvious decrease of the intrinsic viscosity can be observed for all samples during hot-press forming. Compared with neat PET or PET/MAT, a larger decrease for PET/AT indicates that it undergoes a stronger degradation. Similar phenomena are also reported in other polymer/clay systems [24, 25]. It is believed that the

hydroxyl groups on the edge of clay platelet can act as Brønsted acidic sites to accelerate PET degradation [26]. AT is clay with a large amount of silanol group on the surface of nanorods compared with MMT, as the Figure 1a FTIR curve shows. That may be the main reason why PET/AT exhibited more severe degradation during hot-press process. For PET/MAT, MDI reacts with the hydroxyl groups on AT surface, and can reduce the amount of acidic sites. As a result, PET/MAT shows a slower degradation compared with PET/AT.

Pristine PET is a well-known semi-crystallization polymer with a character of low rate of crystallization. The effect of AT and MAT on PET crystallization and melting behaviors were examined by the DSC cooling and heating scans, respectively, as shown in Figure 5.

Figure 5a shows the crystallization curves of pure PET and PET nanocomposites, the T_c of PET differs among the samples and so does the width of the crystallization peak. One observes a remarkably increased T_c , that is from 182°C of neat PET to 190, 192°C of nanocomposites with 1,2 wt% AT, and to 194, 197°C with 1,2 wt% MAT, respectively. The higher T_c and the narrower width of the crystalline

**Figure 5.** DSC curves for neat PET, PET nanocomposites during (a) cooling and (b) heating

peaks observed in the nanocomposites can be explained by the nucleation effect of the nanorods on the PET [27]. It is demonstrated that both AT and functionalized MAT serve as nucleating agents for PET to accelerate the rate of crystallization, while, MAT seems to be a much more efficient nucleating agent for PET compared with AT. The apparent better nucleation effect of MATs in PET matrix is possibly due to the good dispersion of MAT in PET matrix, resulting in larger surface area serving as the nucleation sites. At the same time, the PET chains grafted on the surface of MAT nanorods via MDI can enhance the interaction with the PET matrix greatly. The two factors result in that MAT has a higher nucleating activity than AT and can further accelerate the crystallization rate of PET.

Figure 5b depicts the heating runs of pure PET and PET nanocomposites. There are two melting endotherms that could be observed in each PET nanocomposite sample. It is suggested that the lower one represents the melting of imperfect or smaller crystals, and the higher one represents more perfect bigger crystallites [28, 29]. It is interesting that with the content of AT or MAT increasing from 1 to 2 wt%, the melting peak that is located at the low temperature becomes more distinct and increscent. Moreover, the melting peak (T_m) of the PET/AT sample located at higher temperature shows a little decrease compared with that of neat PET, in contrast, the PET/MAT samples showed the reverse trend, whose melting peak showed 2–4°C increase.

The explanation of this phenomenon is that although the well-dispersed AT or MAT could act as nucleate agent to accelerated the process of PET crystallization, the growth of the crystallites would be restricted, resulting in imperfect or smaller crystals, and the

distribution of crystallites is broader than that of neat PET. With the increase of nanorods content, the spherulites become smaller and less perfect, so multi-melting peak shows up and become more visible, and the T_m of PET/AT decrease to lower temperature. However, the T_m of PET/MAT increased with the content of MAT and higher than that of neat PET. In this case, in the molten state, the segments of the PET molecules can easily interact with the nanorods with grafted PET chains on the surface, then crystallization nuclei developed, which results in some crystallites near the MAT nanorods surface. The intimate adhesion between MAT and PET matrix resulted in the decrease of PET chain mobility, which may have confined the movement of PET crystallite chains. Therefore, higher temperature is needed to provide chain segments with enough energy to start moving, and the melt temperature increases. This may be the main reason of the increases of T_m values in despite of smaller crystal size.

3.3. Mechanical properties

Particle networks and interfacial interactions are often cited as the two primary factors that dominate the mechanical properties of polymer nanocomposites [30]. Dynamic mechanical analysis (DMA) is an effective tool to characterize the interface of filled polymer systems, especially its damping spectra.

The dynamic storage modulus, E' , are drawn in Figure 6a as a function of temperature. The E' value decreases with increasing temperature, and increases with nanorod content. It is clear that, the E' values of the PET/MAT are much higher than that of PET/AT composites over the entire temperature range. The

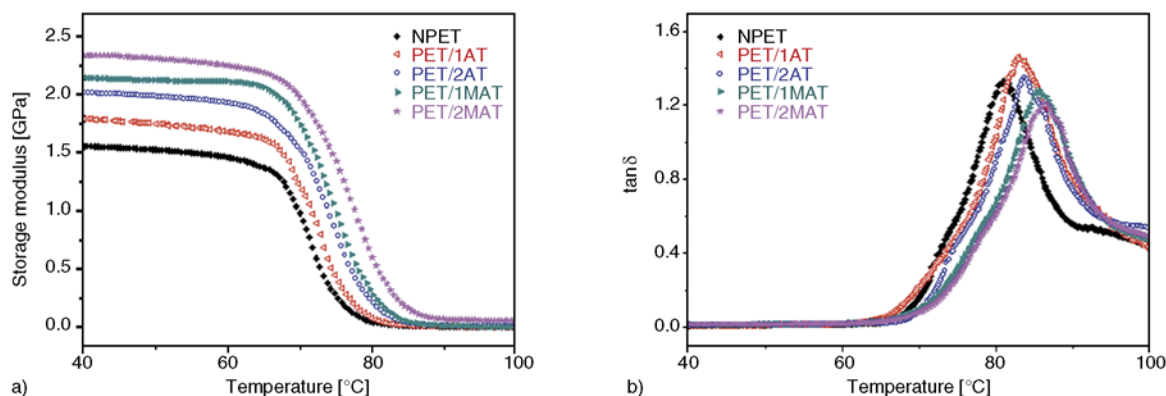


Figure 6. DMA diagrams for neat PET and PET nanocomposites. (a) curves of storage modulus versus temperature and (b) curves of $\tan \delta$ versus temperature.

E' values of all samples at 40 and 80°C are also listed in Table 2. The addition of nanorod significantly increases the value of E' , and this increase is more obvious at higher temperatures. It indicates that the segmental motions of PET chains are restricted by the AT nanorod through physical or chemical interactions. Moreover, MAT with the good dispersion and interfacial interaction in PET/MAT significantly restricts the segmental movements, which results in higher E' values compared with PET/AT. By adding only 2 wt% of MAT, about 47% improvement of storage modulus has been achieved at 40°C compared with pure PET.

The DMA curves of the $\tan \delta$ versus temperature for all samples are presented in Figure 6b. Generally, The T_g values can be extracted from the peak in the $\tan \delta$ curves or loss modulus peak temperatures. The temperatures were extracted as T_g from the $\tan \delta$ curves in our study and listed in Table 1. It is interesting to note that the incorporation of AT lead to about 2°C increase of T_g values. While for the PET/MAT system, a more obvious increase in T_g values can be found. It increases from 81.1°C for neat PET to 85.6°C for PET/1MAT and further increases to 86.1°C for PET/2MAT.

The glass transition temperatures of the polymer matrix depend on the free volume of the polymer. This temperature provides an indirect indication of the dispersion of nanoparticles in the matrix and the particle-matrix interaction, though other factors may also affect this transition. The enhanced T_g values reflects the strength of interfacial interaction and the microstructure of polymer nanocomposites [9, 20]. From the $\tan \delta \sim T$ curves, the T_g of the PET/AT shift slightly to higher temperature as AT loading increases which indicates that the pristine AT nanorods can limit the motion of the PET molecular chains in some extent. In terms of PET/MAT, the higher increase in T_g values indicate a stronger interfacial interaction between the MAT nanorod

and the PET matrix. The direct attachment of PET chains onto MAT nanorod surface makes polymer chains more rigid, and their segmental movements are significantly restricted. With the increase of MAT content in PET films, the number of confined chains increases and therefore the larger elevation in T_g is a natural result.

The enhancement of mechanical properties can be also proved by the tensile testing. The stress-strain curves and mechanical properties of pure PET and the PET nanocomposites films are shown in Figure 7 and Table 2. For comparison, the composites reinforced with as-received AT are also included. Compare with pure PET, PET nanocomposites have higher tensile strength and tensile modulus. However, the enhancing effect is much pronounced in the case of the PET/MAT. The tensile strength of the PET/1MAT is significantly improved by 28% from 44.8 to 57.3 MPa, and the tensile modulus is improved by 17.8% from 1.57 to 1.85 GPa, relative to neat PET. While with 2.0 wt% MAT loading, the tensile strength and initial modulus are further enhanced to 62.5 MPa and 2.14 GPa, which corresponds to a 39.5 and 36.8% enhancement compared to pure PET, respectively.

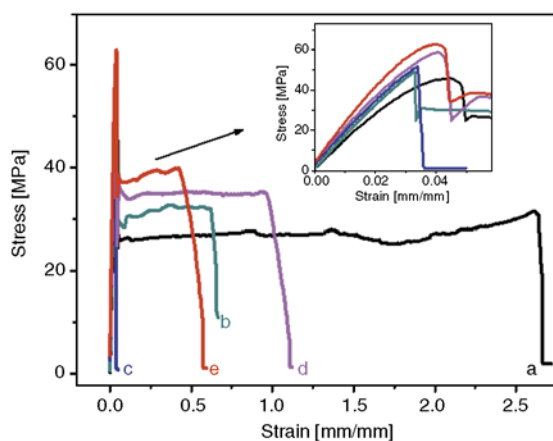


Figure 7. Stress-strain curves for (a) neat PET, (b) PET/1AT, (c) PET/2AT, (d) PET/1MAT and (e) PET/2MAT nanocomposites

Table 2. Mechanical properties from DMA and tensile test

Sample	E' [MPa]		Tensile modulus [GPa]	Tensile stress [MPa]	Elongation at break [mm/mm]
	40°C	80°C			
NPET	1553	47	1.57±0.06	44.8±1.7	2.95±0.56
PET/1AT	1790	77	1.69±0.08	48.3±2.1	0.62±0.18
PET/2AT	2015	277	1.78±0.12	50.6±3.0	—*
PET/1MAT	2140	307	1.85±0.07	58.3±2.3	1.16±0.34
PET/2MAT	2287	440	2.14±0.09	62.5±2.8	0.66±0.12

*PET/2AT composite shows a brittle-rupture tensile behavior, and its elongation at break is not listed.

It has to be noted that the elongation at break for the PET nanocomposites decreased with the introduction of AT and MAT nanorod. PET/2AT composite shows a brittle-rupture tensile behavior, and its elongation at break is not listed in Table 2. It indicates that the nanocomposites became somewhat brittle compared with pure PET. As shown in Figure 7, PET/AT exhibits brittle-rupture behavior with 2 wt% loading, which results from the poor dispersion of pristine AT and the weak interfacial interaction between pristine AT and PET. However, PET/MAT shows higher values of the elongation at break than that of PET/AT. By comparison, the higher value of the elongation at break of PET/MAT should be attributed to the better dispersion of MAT nanorod and stronger interfacial bonding. Many reported results have suggested that the formation of covalent bonding between nanoparticle fillers and polymer matrix, which lead to a more effective stress transfer, thus could improve the mechanical properties of polymer composites. For PET/MAT composites, the MAT nanorod is chemically bonded with PET chains, enabling a more efficient stress transfer from the PET matrix to the nanorod. It can be concluded that the good dispersion of MAT in the PET matrix and the strong interfacial adhesion lead to the significant enhancement of the mechanical properties of PET nanocomposites.

4. Conclusions

In this work, we presented a novel route to fabricate advanced PET nanocomposites using rod-like attapulgite as filler, where AT nanorod is chemically modified to be well dispersed in PET matrix and to possess a strong interaction with the matrix polymer. As confirmed by FTIR and TGA tests, the raw AT has been successfully functionalized in two steps: direct chemical attachment of MDI to the nanorod surface; then the isocyanate groups on surface of MAT nanorod react with EG during the *in situ* polymerization, resulting in PET chains grafted onto the MAT nanorod surface. The resulting interface structure is conducive for the dispersion of MAT nanorod and the increase of interfacial adhesion with the matrix polymer. The existence of MAT could enhance the thermal stability and accelerate the crystallization rate of PET. As expected, the high grafting density leads to efficient load

transfer from the PET matrix to the nanorod, resulting in significant enhancement of the mechanical properties of the PET/MAT even having a small quantity of the MAT compare with pure PET or PET/AT.

Acknowledgements

We would like to express our great thanks to the National Natural Science Foundation of China for financial support (21034005, 51121001).

References

- [1] Scheirs J., Long T. E.: Modern polyesters. Wiley, New York (2003).
- [2] Fakirov S.: Handbook of thermoplastic polyesters. Wiley-VCH, Weinheim (2002).
- [3] Tsai T-Y., Li C-H., Chang C-H., Cheng W-H., Hwang C-L., Wu R-J.: Preparation of exfoliated polyester/clay nanocomposites. *Advanced Materials*, **17**, 1769–1773 (2005).
DOI: [10.1002/adma.200401260](https://doi.org/10.1002/adma.200401260)
- [4] Chang J-H., Kim S. J., Joo Y. L., Im S.: Poly(ethylene terephthalate) nanocomposites by *in situ* interlayer polymerization: The thermo-mechanical properties and morphology of the hybrid fibers. *Polymer*, **45**, 919–926 (2004).
DOI: [10.1016/j.polymer.2003.11.037](https://doi.org/10.1016/j.polymer.2003.11.037)
- [5] Pegoretti A., Kolarik J., Peroni C., Migliaresi C.: Recycled poly(ethylene terephthalate)/layered silicate nanocomposites: Morphology and tensile mechanical properties. *Polymer*, **45**, 2751–2759 (2004).
DOI: [10.1016/j.polymer.2004.02.015](https://doi.org/10.1016/j.polymer.2004.02.015)
- [6] Costache M. C., Heidecker M. J., Manias E., Wilkie C. A.: Preparation and characterization of poly(ethylene terephthalate)/clay nanocomposites by melt blending using thermally stable surfactants. *Polymers for Advanced Technology*, **17**, 764–771 (2006).
DOI: [10.1002/pat.752](https://doi.org/10.1002/pat.752)
- [7] Yao X., Tian X., Xie D., Zhang X., Zheng K., Xu J., Zhang G., Cui P.: Interface structure of poly(ethylene terephthalate)/silica nanocomposites. *Polymer*, **50**, 1251–1256 (2009).
DOI: [10.1016/j.polymer.2009.01.008](https://doi.org/10.1016/j.polymer.2009.01.008)
- [8] Ke Y-C., Wu T-B., Xia Y-F.: The nucleation, crystallization and dispersion behavior of PET–monodisperse SiO₂ composites. *Polymer*, **48**, 3324–3336 (2009).
DOI: [10.1016/j.polymer.2007.03.059](https://doi.org/10.1016/j.polymer.2007.03.059)
- [9] Lee H-J., Oh S-J., Choi J-Y., Kim J. W., Han J., Tan L-S., Baek J-B.: *In situ* synthesis of poly(ethylene terephthalate) (PET) in ethylene glycol containing terephthalic acid and functionalized multiwalled carbon nanotubes (MWNTs) as an approach to MWNT/PET nanocomposites. *Chemistry of Materials*, **17**, 5057–5064 (2005).
DOI: [10.1021/cm051218t](https://doi.org/10.1021/cm051218t)

- [10] May-Pat A., Avilés F., Toro P., Yazdani-Pedram M., Cauich-Rodríguez J. V.: Mechanical properties of PET composites using multiwalled carbon nanotubes functionalized by inorganic and itaconic acids. *Express Polymer Letters*, **6**, 96–106 (2012).
DOI: [10.3144/expresspolymlett.2012.11](https://doi.org/10.3144/expresspolymlett.2012.11)
- [11] Jin S. H., Park Y-B., Yoon K. H.: Rheological and mechanical properties of surface modified multiwalled carbon nanotube-filled PET composite. *Composites Science and Technology*, **67**, 3434–3441 (2007).
DOI: [10.1016/j.compscitech.2007.03.013](https://doi.org/10.1016/j.compscitech.2007.03.013)
- [12] Kim H-U., Bang Y. H., Choi S. M., Yoon K. H.: Morphology and mechanical properties of PET by incorporation of amine-polyhedral oligomeric silsesquioxane. *Composites Science and Technology*, **68**, 2739–2747 (2008).
DOI: [10.1016/j.compscitech.2008.05.020](https://doi.org/10.1016/j.compscitech.2008.05.020)
- [13] Imai Y., Nishimura S., Abe E., Tateyama H., Abiko A., Yamaguchi A., Aoyama T., Taguchi H.: High-modulus poly(ethylene terephthalate)/expandable fluorine mica nanocomposites with a novel reactive compatibilizer. *Chemistry of Materials*, **14**, 477–479 (2002).
DOI: [10.1021/cm010408a](https://doi.org/10.1021/cm010408a)
- [14] Galan E.: Properties and applications of palygorskite-sepiolite clays. *Clay Minerals*, **31**, 443–453 (1996).
- [15] Murray H. H.: Traditional and new applications for kaolin, smectite, and palygorskite: A general overview. *Applied Clay Science*, **17**, 207–221 (2000).
DOI: [10.1016/S0169-1317\(00\)00016-8](https://doi.org/10.1016/S0169-1317(00)00016-8)
- [16] Frost R. L., Mendelovici E.: Modification of fibrous silicates surfaces with organic derivatives: An infrared spectroscopic study. *Journal of Colloid and Interface Science*, **294**, 47–52 (2006).
DOI: [10.1016/j.jcis.2005.07.014](https://doi.org/10.1016/j.jcis.2005.07.014)
- [17] Wang L., Sheng J.: Preparation and properties of polypropylene/org-attapulgite nanocomposites. *Polymer*, **46**, 6243–6249 (2005).
DOI: [10.1016/j.polymer.2005.05.067](https://doi.org/10.1016/j.polymer.2005.05.067)
- [18] Pan H., Chen D.: Preparation and characterization of waterborne polyurethane/attapulgite nanocomposites. *European Polymer Journal*, **43**, 3766–3772 (2007).
DOI: [10.1016/j.eurpolymj.2007.06.031](https://doi.org/10.1016/j.eurpolymj.2007.06.031)
- [19] Pan Y., Xu Y., An L., Lu H., Yang Y., Chen W., Nutt S.: Hybrid network structure and mechanical properties of rodlike silicate/cyanate ester nanocomposites. *Macromolecules*, **41**, 9245–9258 (2008).
DOI: [10.1021/ma800819s](https://doi.org/10.1021/ma800819s)
- [20] An L., Pan Y., Shen X., Lu H., Yang Y.: Rod-like attapulgite/polyimide nanocomposites with simultaneously improved strength, toughness, thermal stability and related mechanisms. *Journal of Material Chemistry*, **18**, 4928–4941 (2008).
DOI: [10.1039/B805849K](https://doi.org/10.1039/B805849K)
- [21] Yuan X., Li C., Guan G., Liu X., Xiao Y., Zhang D.: Synthesis and characterization of poly(ethylene terephthalate)/attapulgite nanocomposites. *Journal of Applied Polymer Science*, **103**, 1279–1286 (2007).
DOI: [10.1002/app.25207](https://doi.org/10.1002/app.25207)
- [22] Yuan X., Li C., Guan G., Xiao Y., Zhang D.: Thermal stability of surfactants with amino and imido groups in poly(ethylene terephthalate)/clay composites. *Journal of Applied Polymer Science*, **109**, 4112–4120 (2008).
DOI: [10.1002/app.28431](https://doi.org/10.1002/app.28431)
- [23] Gilman J. W., Awad W. H., Davis R. D., Shields J., Harris R. H., Davis C., Morgan A. B., Sutto T. E., Callahan J., Trulove P. C., DeLong H. C.: Polymer/layered silicate nanocomposites from thermally stable trialkylimidazolium-treated montmorillonite. *Chemistry of Materials*, **14**, 3776–3785 (2002).
DOI: [10.1021/cm011532x](https://doi.org/10.1021/cm011532x)
- [24] Leszczyńska A., Njuguna J., Pielichowski K., Banerjee J. R.: Polymer/montmorillonite nanocomposites with improved thermal properties: Part II. Thermal stability of montmorillonite nanocomposites based on different polymeric matrixes. *Thermochimica Acta*, **454**, 1–22 (2007).
DOI: [10.1016/j.tca.2006.11.003](https://doi.org/10.1016/j.tca.2006.11.003)
- [25] Matayabas J. J. Jr., Turner S. R.: Nanocomposite technology for enhancing the gas barrier of polyethylene terephthalate. in ‘Polymer-clay nanocomposites’ (eds.: Pinnavaia T. J., Beall G. W.) Wiley, New York, 207–228 (2000).
- [26] Xu X., Ding Y., Qian Z., Wang F., Wen B., Zhou H., Zhang S., Yang M.: Degradation of poly(ethylene terephthalate)/clay nanocomposites during melt extrusion: Effect of clay catalysis and chain extension. *Polymer Degradation and Stability*, **94**, 113–123 (2009).
DOI: [10.1016/j.polymdegradstab.2008.09.009](https://doi.org/10.1016/j.polymdegradstab.2008.09.009)
- [27] Calcagno C. I. W., Mariani C. M., Teixeira S. R., Mauler R. S.: The effect of organic modifier of the clay on morphology and crystallization properties of PET nanocomposites. *Polymer*, **48**, 966–974 (2007).
DOI: [10.1016/j.polymer.2006.12.044](https://doi.org/10.1016/j.polymer.2006.12.044)
- [28] Chen Z., Luo P., Fu Q.: Preparation and properties of organo-modifier free PET/MMT nanocomposites via monomer intercalation and *in situ* polymerization. *Polymers for Advanced Technology*, **20**, 916–925 (2009).
DOI: [10.1002/pat.1336](https://doi.org/10.1002/pat.1336)
- [29] Kong Y., Hay J. N.: Multiple melting behaviour of poly(ethylene terephthalate). *Polymer*, **44**, 623–633 (2003).
DOI: [10.1016/S0032-3861\(02\)00814-5](https://doi.org/10.1016/S0032-3861(02)00814-5)
- [30] Rao Y. Q., Pochan J. M.: Mechanics of polymer-clay nanocomposites. *Macromolecules*, **40**, 290–296 (2007).
DOI: [10.1021/ma061445w](https://doi.org/10.1021/ma061445w)

Modifying the electrical behaviour of polypropylene/carbon nanotube composites by adding a second nanoparticle and by annealing processes

H. Palza*, C. Garzón, O. Arias

Departamento de Ingeniería Química y Biotecnología, Facultad de Ciencias Físicas y Matemáticas, Universidad de Chile, Beauchef 861, Casilla 277, Santiago, Chile

Received 28 December 2011; accepted in revised form 24 February 2012

Abstract. The effect of different nanoparticles on the geometrical percolation transition of multi-wall carbon nanotubes (CNT) in polypropylene (PP) composites was studied. Our results show that the electrical conductivity of PP/CNT composites (around 2 vol%) can be tuned depending on the characteristic of the third component. Non-conductive layered silica fillers disrupt the CNT percolated network reducing the electrical conductivity of the composite. Spherical nanoparticles otherwise, either copper metal or silica-based, decrease the percolation threshold down to 0.5 vol% of CNT. These results cannot be explained by previous theories about the effect of a second particle on the electrical behaviour of polymer/CNT composites such as the interparticle bridging or the excluded volume. The effect of annealing in the melt was further analyzed and our results show that depending on the concentration and the type of filler, the electrical conductivity of the composites can be increased several orders of magnitude.

Keywords: nanocomposites, hybrid composite materials, metal nanoparticles, clay, carbon nanotubes

1. Introduction

The production of electrical conductive plastic materials seems to be one of the most important applications of polymer/carbon nanotube (CNT) composites in commodity materials such as polyolefins. The reason is the extremely low amount of filler needed to obtain the geometrical percolation threshold in these systems as compared with other nano or microfillers [1]. Motivated by the good results in this field, researchers have tried to decrease further the percolation transition by adding to polymer/CNT composites a third component, such as another polymer or a second particle [2–4]. A larger confinement of CNT has been reported as the driving force for the decrease in the percolation threshold in these hybrid composite materials [2, 3, 5].

By adding clay particles into epoxy/single wall carbon nanotube (SWCNT) composites, Liu and Grunlan [4] found that the electrical conductivity percolation threshold of CNT can be reduced by a factor of five. SWCNTs appear to have an affinity for clay causing a more exfoliated and a better networked state in the composites explaining partially the results [4]. The excluded volume created by the micron-scale clay clusters forming a segregated network of nanotubes can also explain these conductivity improvements [4]. In PP/CNT composites, the addition of micro-particles of CaCO₃ results in a significant reduction in the electrical resistivity that was explained by the concept of effective concentration similar to the excluded volume theory [5]. After incorporation of the inert micro-filler into the

*Corresponding author, e-mail: hpalza@ing.uchile.cl
© BME-PT

composite, CaCO_3 will hold up certain space increasing the effective concentration of CNT (volume percentage) and in this way the probability of connecting with each other. Similar results were reported by the same authors using other fillers (e.g. talc and wollastonite) and polymer matrices (e.g. polyoxymethylene and polyamide) [5]. This theory is further supported by the results from Kotaki *et al.* [6] in epoxy/clay/vapour grown carbon fiber hybrid composite materials. Despite the above mentioned results, a higher electrical percolation threshold in PP/clay/CNT hybrid composite materials than in PP/CNT composites has been reported [7]. The disruption of the interconnecting conduction paths from the CNT because of the clay was stated as the reason for this drop in the conductivity.

An interesting novel hybrid composite material based on PP/CNT composites was developed by Liang *et al.* [8]. The addition of small amount of silver metal nanoparticles promoted significantly the electrical properties of the resulting material [8]. The mechanism proposed for this improvement was the anchoring of Ag particles among CNT clusters facilitating the electron transfer through the carbon filler. In this way, CNT act as bridges for individual silver particles, or vice versa, yielding high electrical conductivities and decreasing the percolation threshold. This model is supported by the results of Balik and coworkers [2, 3] studying hybrid composite materials composed of blend matrices with carbon fiber and graphite particles. In particular, carbon fiber can bridge distant and unconnected graphite particles increasing the overall conductivity of the system. However, the above mentioned authors did not perform experiments with non-conductive particles of similar characteristics. Therefore, the need of a second conductive particle has not been proved in this context.

The above mentioned shows that the effect of a third component on the electrical performance of polymer/CNT composites, forming a hybrid composite material, is not completely understood justifying further investigations. In this article, we analyze how the type of particle can tune the geometrical electrical percolation of polypropylene/CNT composites. In particular, layered-clay, spherical copper metal, and spherical silica particles of different diameters were studied. Our results show that the final conductivity of the hybrid composite mate-

rial depends on the particle aspect ratio and that models such as excluded volume and interparticle bridge are not able to explain the whole experimental evidence. The effect of annealing in the melt on the conductivity of the samples was further studied.

2. Experimental

A commercial grade polypropylene from Petroquim S.A. (Chile) (PH1310) with a melt flow rate ($230^\circ\text{C}/2.16\text{ kg}$) of $13\text{ g}/10\text{ min}$ (Norm ASTM D-1238/95) was used as matrix. The multiwalled carbon nanotubes (MWCNT) were kindly supplied by Bayer Material Science AG (Germany) (Baytubes C150P). Based on the datasheet information provided by Bayer, they are characterized by a purity higher than 95 wt%, number of walls between 2 and 15, an outer mean diameter of 13–16 nm, an inner mean diameter of 4 nm, length between 1 and $>10\text{ }\mu\text{m}$, and a bulk density around $150\text{ kg}/\text{m}^3$. The montmorillonite clay filler is a Cloisite 15A from Southern Clay Product Inc. (USA) with a cation exchange capacity (CEC) of 125 [meq/100 g of clay]. The copper nanoparticles (CuNP) with an average particle size of 5 nm as measured by high resolution transmission electron microscopy (TEM) were supplied by Versus Co. Ltd. (Chile).

Spherical silica nanoparticles of 100 nm were synthesized by the sol-gel method using a two-stage mixed semi-batch method, as previously reported [9]. In the first stage, Solutions A and B were prepared. For Solution A, 0.5 M of tetraethylortosilicate (TEOS) was dissolved in 22 mL of ethanol whereas in Solution B, 0.2 M of aqueous ammonia solution was added to 23 mL of ethanol and 2 mL of water. Solution B was then added dropwise to Solution A. The resulting mixture was allowed to react for 60 minutes at 40°C under a N_2 atmosphere. In the second stage, Solutions A and B were again prepared and added to the reactor containing the solution and the particles prepared in the first stage. The solutions were separated by centrifugation (10.000 rpm, 20 minutes) and washed three times with ethanol. For the 10 nm spherical particles a similar procedure was carried out but adding 23 mL of ethanol and 55 mL of TEOS in Solution A and 23.5 mL of ethanol, 54 mL of water and 2.2 mL of ammonia for Solution B. The nanoparticles were then calcined for 4 hours at 450°C and dried for 6 hours at 100°C .

The composites and the master batch for clay filler were prepared by using a Brabender Plasticorder (Brabender, Germany) internal mixer at 190°C and a speed of 110 rpm. For PP/CNT composites, predetermined amounts of the nanofiller, antioxidant and neat polymer were mixed under nitrogen atmosphere in order to obtain the composites with filler content ranges from 0.5 to 4 vol%. First, a half of polymer pellets (around 1 cm size) with the antioxidant (powder) were added to the mixer operated at 75 rpm. After 3 minutes approximately for melt the polymer, the filler was added during 2 minutes. Finally, the rest of polymer pellets was added and the speed of the mixer was raised a 110 rpm for 10 minutes. Therefore, the total mixing time was around 16 minutes. For the hybrid materials, first the polymer was added to the mixer followed by the proper amount of CNT as above explained and afterwards, the desired amount of the second nanoparticle to prepare hybrid materials was added. In this case, the total time for the mixing was around 20 minutes. To analyse the effect of mixing time on the electrical behaviour of PP/CNT composites, several times were tested in the mixer but not effect was detected in the electrical behaviour. For PP/CNT/clay hybrid composites a commercial polypropylene grafted with maleic anhydride (Polybond 3200, Chemtura, USA) was further used as compatibilizer. In this case, a master batch containing a mixture of silica layered particles and the compatibilizer with a weight ratio of 1:3 was prepared under the same conditions as explained above.

Transmission electron microscopy (TEM) images were made in a Philips (The Netherlands) model CM 100 at 80 kV. Ultrathin sections of about 70 nm were obtained by cutting the samples with an Ultracut Reichert-Jung (Germany) microtome equipped with a Diatome diamond knife. For the electric resistivity, different megohmmeters (Megger BM11 with a highest voltage of 1200 V and AEMC 1060 with a highest voltage of 5000 V) were used depending on the conductivity of the samples. With this set-up the standard two-points method was used. These values were compared with those coming from a commercial four-points methods (Jandel RM3-AR, Multiheight Probe[®]), and not relevant differences were detected. For each electrical value displayed in this contribution, at least three samples were prepared and four measurements for each one were carried out. In general, differences around one order of magnitude were detected in the non-percolated samples having low conductivity values ($\sim 10^{-9}$ S/cm). For percolated samples otherwise the experimental error for conductivities was less than 50%. For annealing tests, the samples were putted in a hot-press at 190°C for 30 minutes without pressure. For these tests, samples of 50×10 mm² and a thickness of 1 mm were used.

3. Results and discussion

3.1. Polypropylene/CNT composites

Figure 1a displays a representative image of a composite of polypropylene with 2.4 vol% of multiwalled carbon nanotubes (CNT). The CNT aggre-

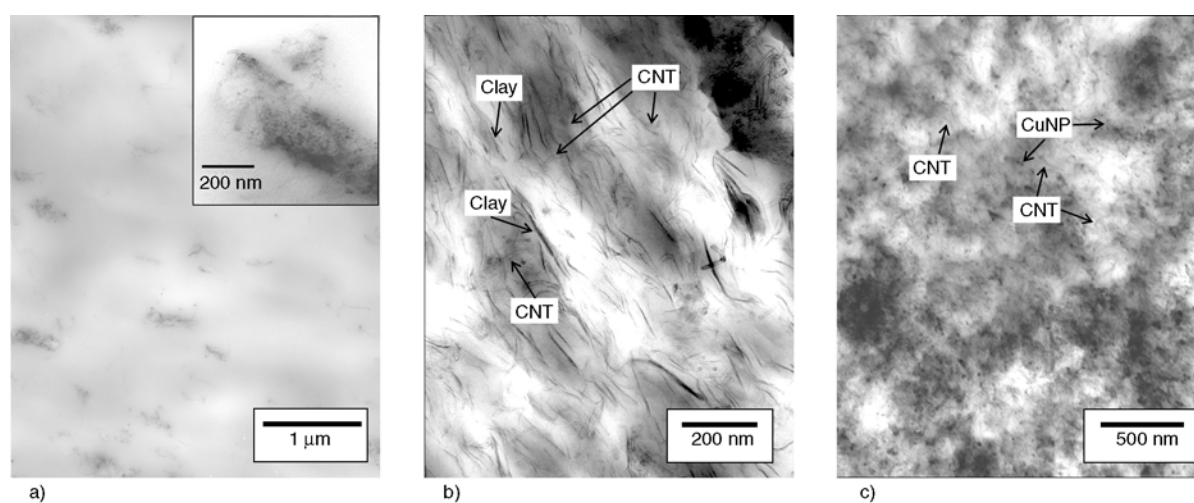


Figure 1. Representative TEM images of some samples studied: a) polypropylene/CNT composites with 2.4 vol% of filler; b) polypropylene with 2.4 vol% of CNT and 5.5 vol% of clay; and c) polypropylene with 2.4 vol% of CNT and 10 vol% of copper nanoparticles (CuNP)

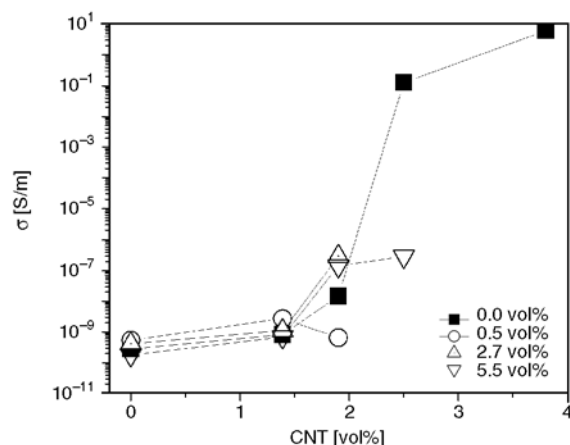


Figure 2. Effect of clay particles on the electrical conductivity of polypropylene/CNT composites

gate forming secondary structures with sizes around 400 nm that are well distributed into the polymer matrix. Together with these agglomerates, isolated CNT can also be found as reported previously [10, 11]. In the in-set of Figure 1a, there is an image at larger magnification showing the characteristic morphology of isolated CNT by regular resolution TEM. The lateral wall of the tubes are clearly observed because the higher electron density (the (002) lattice image) whereas the top/bottom part of the tubes cannot be detected appearing as transparent. Although it is not observed by our TEM images, the secondary structures can be continuously interconnected through the polymer by means of isolated CNTs forming a network. This hypothesis is confirmed observing Figure 2 where the electrical conductivity is plotted against the CNT concentration. At concentrations higher than 2 vol% a drastic increase in the conductivity of the composites is displayed because of the presence of a continue conduction path of CNT through the polymer matrix [1, 12]. Based on this information, a set of hybrid composite materials containing different concentrations of CNT and either copper metal or silica nanoparticles, were prepared and characterized in order to discuss the effect of a second nanoparticle on the electrical behaviour of PP/CNT composites.

3.2. Layered particles

There are several articles confirming that high aspect ratio particles, such as layered clays, increase the electrical conductivity of PP/CNT composites. However, our results show that well dispersed layered fillers do not raise the conductivity as observed

in Figure 2. Moreover, with 5.5 vol% of clay, the layered filler drastically reduces the conductivity of the composites showing a disruption of the CNT network. The restrictions that layered fillers cause on the CNT network can be further observed by TEM images as displayed in Figure 1b. In this figure, clay appears as dense layered particles contrary to CNT where the lateral walls are only observed as discussed previously. Therefore, a reduction in the volume available for CNT dispersion due to the clays is not the only effect of these layered fillers. High aspect ratio clay particles can also hinder the interconnection between CNT acting as a wall between them. In this way, based on our results and those from previous literature, we can say that depending on the concentration of clay and its dispersion, two processes compete having opposite consequences: 1) decrease in the free volume available for CNT dispersion increasing the electrical conductivity, as reported previously; and 2) disruption of the CNT network decreasing the conductivity, as our results support.

3.3. Conductive spherical particles

Motivated by the recent results obtained by Liang *et al.* [8] and Balik and coworkers [2, 3] showing that a conductive second nanoparticle can increase the electrical conductivity of polymer/CNT composites, we added copper metal nanoparticles (CuNP) to PP/CNT composites. Figure 1c show a representative image of this hybrid composite material where the black-spot represent the CuNP. If the dispersion of these CuNP in the hybrid composite material is compared with that from PP/CuNP composite [13], a drastic decrease in the agglomeration level is observed when CNT are presented. In particular, Figure 1c display well dispersed individual CuNP instead of agglomerated structure as in PP/CuNP composites [13]. Our results could be explained based on the conclusion of Liu *et al.* [4] regarding the larger affinity of CNT to clay particles improving its dispersion. In this way, CuNP could have larger affinity to CNT than with PP producing a better dispersion of the inorganic filler in the hybrid composite material. The latter is supported by the recent publications about in-situ synthesis of CuNP onto CNT [14, 15].

Figure 3 shows that by adding spherical conductive particles the overall conductivity of the composite

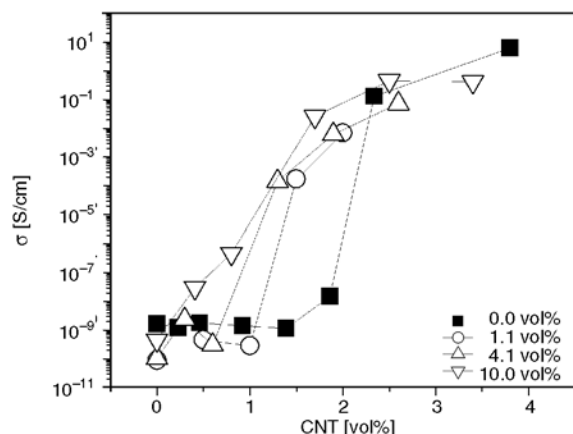


Figure 3. Effect of copper metal nanoparticles on the electrical conductivity of polypropylene/CNT composites

is increased and the percolation threshold is reduced by a factor of two. Moreover, the conductivity depends on the amount of CuNP in the material. An interesting characteristic of these novel hybrid materials is that the electrical conductivity when they are percolated is similar to those obtained from the composites with CNT.

3.4. Non-conductive spherical particles

Based on our results and previous articles, metal particles acting as bridge between CNT, or vice versa, is a plausible mechanism to explain the enhanced electrical conductivity in this kind of hybrid composite materials. However, the addition of non-conductive fillers to PP/CNT composites as similar as CuNP is the only way to confirm this bridge-theory. In this context, two silica particles of 10 and 100 nm were synthesized by the sol-gel method. Particles of 10 nm represent the isolated CuNP whereas those of 100 nm are prepared as secondary structures of CuNP in PP matrices are of this order of magnitude in size [13].

Figure 4 shows the results of adding 10 vol% of non-conductive silica particles to PP/CNT composites where it is also displayed the results from hybrid composite materials prepared with CuNP. Results from Figure 4 clearly show that non-conductive fillers are able to increase drastically the conductivity of the composite reducing the percolation threshold by a factor of two. The effect of these non-conductive filler is size-dependent as 10 nm particles render larger enhancements to the electrical conductivity than 100 nm particles. Noteworthy,

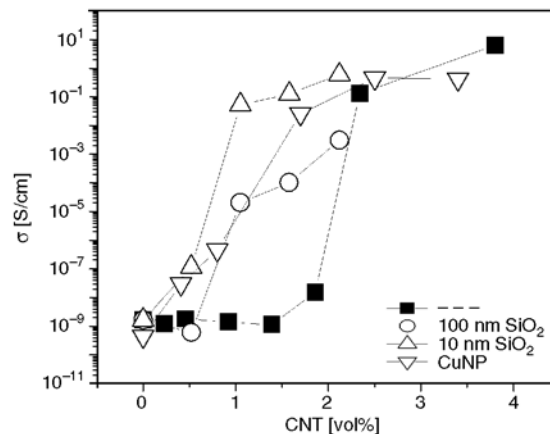


Figure 4. Effect of adding 10 vol% of different nanoparticles to the electrical conductivity of polypropylene/CNT composites

the improvement in conduction by these fillers is similar to that caused by CuNP ruling out the hypothesis that conductive particles can act as a bridge between CNT or vice versa. A plausible mechanism explaining these findings is the increased effective concentration of CNT in the polymer matrix as spherical particles can reduce the available volume for filler dispersion as discussed previously for other fillers.

Therefore, based on the information displayed in Figure 2, 3 and 4, we can conclude that the effect of a second nanoparticle on the electrical conductivity of PP/CNT composites can be explained by two complementary and competitive mechanisms: 1) the excluded volume theory and 2) the disruption of the CNT network by the filler. Layered clay fillers disrupt the geometrical percolation of the composite reducing the conductivity whereas spherical particles reduce the free volume for CNT dispersion increasing the effective concentration and the electrical conductivity of the composite.

3.5. Annealing effect

It is well known that the conductivity of polymer/CNT composites can be increased by annealing at temperatures higher than the melting temperature of the matrix [16, 17]. These changes in conductivity are related with the non-equilibrium state of CNT in high viscous matrices under these quiescent conditions [18] driven by either the entropic forces of self-organization [19] or the high attractive interparticle potential [20–22] overcoming its limited Brownian motion. These processes together with the filler re-

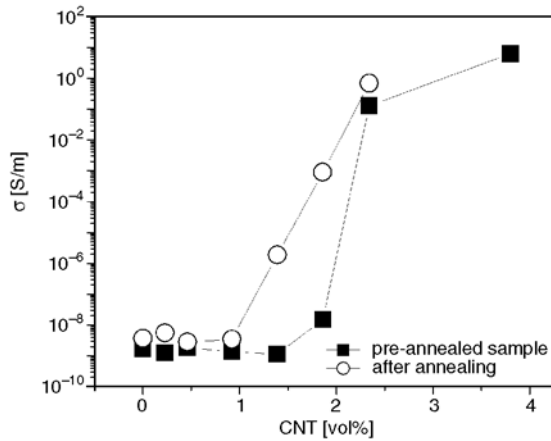


Figure 5. Effect of annealing (30 minutes at 190°C) on the electrical conductivity of polypropylene/CNT composites

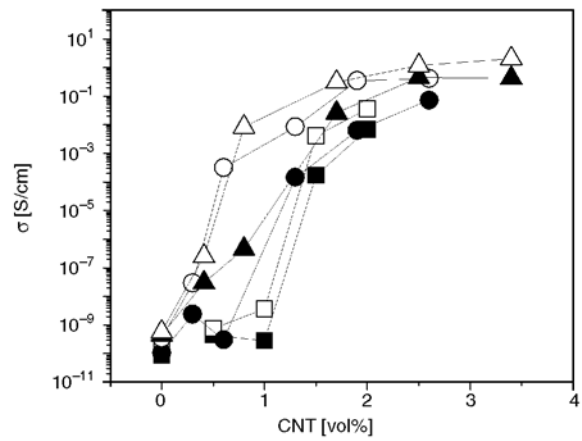


Figure 6. Effect of annealing (30 minutes at 190°C) on the electrical conductivity of polypropylene/CNT/copper nanoparticle (CuNP) hybrid composite materials. Square: 1,1 vol% of CuNP; circle: 4,1 vol% of CuNP; and triangle: 10 vol% of CuNP. Black symbols represent pre-annealed samples whereas white symbols represent the annealed samples.

arrangements due to relaxation of polymer chains at high temperatures, can form conductive agglomerates from the initially dispersed CNT [16, 22–24]. Independent of the mechanism, under annealing the mean distance between CNT, or its clusters, decreases causing enhanced conductivities [17]. This hypothesis regarding agglomeration of CNT under annealing, although at higher pressure, has been recently observed by TEM images [11].

Figure 5 displays the effect of annealing on the electrical behaviour of PP/CNT composites. As discussed above, at high temperatures the composites increase the electrical conductivity due to a rearrangement of CNT decreasing its mean distance [17]. Although this tendency is well known in polymer/CNT composites, the effect of a second nanoparticle on this behaviour has not been reported. Regarding layered particles as second filler, our results (not shown) indicate that there is no a significant effect of annealing on the conductivities of PP/CNT composites and changes in the same range as the experimental error are mainly measured. However, when spherical particles are used, more interesting results are observed as the effect will depend on the particle size and its concentration. Figure 6 displays the effect of annealing on the electrical conductivity of PP/CNT/CuNP hybrid composite materials where the data from non-annealed samples are also displayed for comparison. Similar to PP/CNT composites, annealing process is able to increase the conductivity of the samples but the final effect depends on the amount of the second filler. At low CuNP concentration, a softly increase

(in the range of the experimental error) is mainly observed independent of the amount of CNT. These increases are lower than those obtained from PP/CNT meaning that similar to layered fillers, low CuNP content reduces or hinders the re-arrangement processes of CNT.

The effect of annealing in PP/CNT/silica nanoparticle hybrid composites is displayed in Figure 7. Our results indicate that the annealing effect depends on the size of the second filler as samples with particles of 10 nm do not show any effect whereas sam-

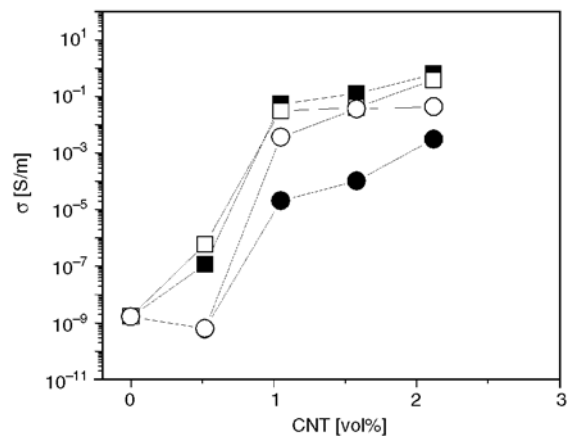


Figure 7. Effect of annealing (30 minutes at 190°C) on the electrical conductivity of polypropylene/CNT hybrid composite materials with 10 vol% of silica nanoparticles. Square: 10 nm particles and circle: 100 nm particles. Black symbols represent pre-annealed samples whereas white symbols represent the annealed samples.

ples with particles of 100 nm display strong increases in conductivities. Regarding samples with 10 nm particles, there are two plausible theories about the lack of annealing effect: 1) nanoparticles hinder the re-arrangement of CNT similar to that discussed in the case of CuNP and clay; and 2) the presence of a second nanoparticle already improves the conductivity of the pre-annealed sample and therefore to increase even more the conductivity is not possible. The latter is based on the fact that these hybrid composite materials have the highest conductivities when compared with the other samples. On the other hand, the difference observed between samples with CuNP and samples with silica nanoparticles of 10 nm can be related with the agglomeration processes in the former system as reported previously [13].

4. Conclusions

The effect of a second nanoparticle on the electrical behaviour of polypropylene/CNT materials was studied. Our results show that the final conductivity of the hybrid composite depends on the characteristic of the second filler. In particular, layered fillers disrupt the geometrical percolation decreasing the conductivity of the sample whereas nano-spheres could reduce the available volume for CNT dispersion decreasing the electrical percolation threshold. Furthermore, conductive CuNP and non-conductive silica nanoparticles have the same effect ruling out the bridge theory as reported previously. Regarding annealing effect, polypropylene/CNT composites and hybrid composite materials with high amount of the second filler show relevant increases in the electrical conductivity with time. However, layered fillers and low concentration of spherical nanoparticles hinder the re-arrangement of CNT avoiding the annealing effect at high temperatures.

Acknowledgements

The authors gratefully acknowledge the financial support of CONICYT, projects FONDECYT 1110078. It is also expressed the thanks to Dr. W. Sierralta for the TEM images and to Dr. R. Quijada for the support during this research.

References

[1] Moniruzzaman M., Winey K. I.: Polymer nanocomposites containing carbon nanotubes. *Macromolecules*, **39**, 5194–5205 (2006).
DOI: [10.1021/ma060733p](https://doi.org/10.1021/ma060733p)

[2] Thongruang W., Spontak R. J., Balik C. M.: Bridged double percolation in conductive polymer composites: An electrical conductivity, morphology and mechanical property study. *Polymer*, **43**, 3717–3725 (2002).
DOI: [10.1016/S0032-3861\(02\)00180-5](https://doi.org/10.1016/S0032-3861(02)00180-5)

[3] Thongruang W., Spontak R. J., Balik C. M.: Correlated electrical conductivity and mechanical property analysis of high-density polyethylene filled with graphite and carbon fiber. *Polymer*, **43**, 2279–2286 (2002).
DOI: [10.1016/S0032-3861\(02\)00043-5](https://doi.org/10.1016/S0032-3861(02)00043-5)

[4] Liu L., Grunlan J. C.: Clay assisted dispersion of carbon nanotubes in conductive epoxy nanocomposites. *Advanced Functional Materials*, **17**, 2343–2348 (2007).
DOI: [10.1002/adfm.200600785](https://doi.org/10.1002/adfm.200600785)

[5] Bao H-D., Guo Z-X., Yu J.: Effect of electrically inert particulate filler on electrical resistivity of polymer/multi-walled carbon nanotube composites. *Polymer*, **49**, 3826–3831 (2008).
DOI: [10.1016/j.polymer.2008.06.024](https://doi.org/10.1016/j.polymer.2008.06.024)

[6] Kotaki M., Wang K., Toh M. L., Chen L., Wong S. Y., He C.: Electrically conductive epoxy/clay/vapor grown carbon fiber hybrids. *Macromolecules*, **39**, 908–911 (2006).
DOI: [10.1021/ma0522561](https://doi.org/10.1021/ma0522561)

[7] Bao S. P., Liang G. D., Tjong S. C.: Positive temperature coefficient effect of polypropylene/carbon nanotube/montmorillonite hybrid nanocomposites. *IEEE Transactions Nanotechnology*, **8**, 729–736 (2009).
DOI: [10.1109/TNANO.2009.2023650](https://doi.org/10.1109/TNANO.2009.2023650)

[8] Liang G. D., Bao S. P., Tjong S. C.: Microstructure and properties of polypropylene composites filled with silver and carbon nanotube nanoparticles prepared by melt-compounding. *Materials Science and Engineering B*, **142**, 55–61 (2007).
DOI: [10.1016/j.mseb.2007.06.028](https://doi.org/10.1016/j.mseb.2007.06.028)

[9] Palza H., Vera J., Wilhelm M., Zapata P.: Spherulite growth rate in polypropylene/silica nanoparticle composites: Effect of particle morphology and compatibilizer. *Macromolecular Materials and Engineering*, **296**, 744–751 (2011).
DOI: [10.1002/mame.201000405](https://doi.org/10.1002/mame.201000405)

[10] Hu G., Zhao C., Zhang S., Yang M., Wang Z.: Low percolation thresholds of electrical conductivity and rheology in poly(ethylene terephthalate) through the networks of multi-walled carbon nanotubes. *Polymer*, **47**, 480–486 (2006).
DOI: [10.1016/j.polymer.2005.11.028](https://doi.org/10.1016/j.polymer.2005.11.028)

[11] Alig I., Skipa T., Lellinger D., Pötschke P.: Destruction and formation of a carbon nanotube network in polymer melts: Rheology and conductivity spectroscopy. *Polymer*, **49**, 3524–3531 (2008).
DOI: [10.1016/j.polymer.2008.05.037](https://doi.org/10.1016/j.polymer.2008.05.037)

[12] Alig I., Lellinger D., Dudkin S. M., Pötschke P.: Conductivity spectroscopy on melt processed polypropylene–multiwalled carbon nanotube composites: Recovery after shear and crystallization. *Polymer*, **48**, 1020–1029 (2007).
DOI: [10.1016/j.polymer.2006.12.035](https://doi.org/10.1016/j.polymer.2006.12.035)

- [13] Delgado K., Quijada R., Palma R., Palza H.: Polypropylene with embedded copper metal or copper oxide nanoparticles as a novel plastic antimicrobial agent. *Letters in Applied Microbiology*, **53**, 50–54 (2011). DOI: [10.1111/j.1472-765X.2011.03069.x](https://doi.org/10.1111/j.1472-765X.2011.03069.x)
- [14] Wang P., Huang B., Wei J., Qin X., Yao S., Zhang Q.: Preparation of Cu nanoparticles on carbon nanotubes by solution infusion method and calcining in ambient atmosphere. *Materials Letters*, **61**, 5255–5257 (2007). DOI: [10.1016/j.matlet.2007.04.041](https://doi.org/10.1016/j.matlet.2007.04.041)
- [15] Wu H-Q., Wei X-W., Shao M-W., Gu J-S., Qu M-Z.: Synthesis of copper oxide nanoparticles using carbon nanotubes as templates. *Chemical Physics Letters*, **364**, 152–156 (2002). DOI: [10.1016/S0009-2614\(02\)01301-5](https://doi.org/10.1016/S0009-2614(02)01301-5)
- [16] Cipriano B. H., Kota A. K., Gershon A. L., Laskowski C. J., Kashiwagi T., Bruck H. A., Raghavan S. R.: Conductivity enhancement of carbon nanotube and nanofiber-based polymer nanocomposites by melt annealing. *Polymer*, **49**, 4846–4851 (2008). DOI: [10.1016/j.polymer.2008.08.057](https://doi.org/10.1016/j.polymer.2008.08.057)
- [17] Palza H., Kappes M., Hennrich F., Wilhelm M.: Morphological changes of carbon nanotubes in polyethylene matrices under oscillatory tests as determined by dielectrical measurements. *Composites Science and Technology*, **71**, 1361–1366 (2011). DOI: [10.1016/j.compscitech.2011.05.010](https://doi.org/10.1016/j.compscitech.2011.05.010)
- [18] Obrzut J., Douglas F. J., Kharchenko S. B., Migler K. B.: Shear-induced conductor-insulator transition in melt-mixed polypropylene-carbon nanotube dispersions. *Physical Review B*, **76**, 195420/1–195420/9 (2007). DOI: [10.1103/PhysRevB.76.195420](https://doi.org/10.1103/PhysRevB.76.195420)
- [19] Skipa T., Lellinger D., Saphiannikova M., Alig I.: Shear-stimulated formation of multi-wall carbon nanotube networks in polymer melts. *Physica Status Solidi B*, **246**, 2453–2456 (2009). DOI: [10.1002/pssb.200982265](https://doi.org/10.1002/pssb.200982265)
- [20] Kharchenko S. B., Douglas J. F., Obrzut J., Grulke E. A., Migler K. B.: Flow-induced properties of nanotube-filled polymer materials. *Nature Materials*, **3**, 564–568 (2004). DOI: [10.1038/nmat1183](https://doi.org/10.1038/nmat1183)
- [21] Hobbie E. K., Fry D. J.: Nonequilibrium phase diagram of sticky nanotube suspensions. *Physical Review Letters*, **97**, 036101/1–036101/4 (2006). DOI: [10.1103/PhysRevLett.97.036101](https://doi.org/10.1103/PhysRevLett.97.036101)
- [22] Huang Y. Y., Ahir S. V., Terentjev E. M.: Dispersion rheology of carbon nanotubes in a polymer matrix. *Physical Review B*, **73**, 125422/1–125422/9 (2006). DOI: [10.1103/PhysRevB.73.125422](https://doi.org/10.1103/PhysRevB.73.125422)
- [23] Skipa T., Lellinger D., Böhm W., Saphiannikova M., Alig I.: Influence of shear deformation on carbon nanotube networks in polycarbonate melts: Interplay between build-up and destruction of agglomerates. *Polymer*, **51**, 201–210 (2010). DOI: [10.1016/j.polymer.2009.11.047](https://doi.org/10.1016/j.polymer.2009.11.047)
- [24] Pujari S., Rahatekar S. S., Gilman J. W., Koziol K. K., Windle A. H., Burghardt W. R.: Orientation dynamics in multiwalled carbon nanotube dispersions under shear flow. *Journal of Chemistry Physics*, **130**, 214903/1–214903/9 (2009). DOI: [10.1063/1.3139446](https://doi.org/10.1063/1.3139446)

The micellization and dissociation transitions of thermo-, pH- and sugar-sensitive block copolymer investigated by laser light scattering

Y. C. Tang*, J. H. Wu, J. X. Duan

College of Chemistry and Materials Science, Anhui Normal University, 241000 Wuhu, China

Received 5 December 2011; accepted in revised form 25 February 2012

Abstract. A triple-stimuli responsive polymer, poly(3-acrylamidophenylboronic acid)-b-poly(N-isopropylacrylamide) (PAAPBA-b-PNIPAM), has been synthesized by reversible addition-fragmentation chain transfer polymerization. Temperature, pH, and fructose induced micellization and dissociation transition of block copolymer was investigated by a combination of static and dynamic laser light scattering. PAAPBA-b-PNIPAM copolymer self-assembles into micelles with PAAPBA block as core and PNIPAM as shell in lower pH aqueous solution at room temperature. Increasing the temperature causes the micelle to shrink due to the dehydration of PNIPAM segments at pH 6.2. After the elevation of solution pH from 6.2 to 10.0, the increase in the hydrophilicity of PAAPBA block leads to an expulsion of unimers from micelles. In addition, the fructose addition further enhances the dissociation of micelles. Our experiments demonstrate that the micelle to unimer transition process proceeds via the step-by-step sequential expulsion of individual chains.

Keywords: smart polymers, PAAPBA-b-PNIPAM, micelle dissociation, laser light scattering

1. Introduction

Stimuli-responsive block copolymers have attracted considerable interest over the past decades because of their potential applications in drug delivery, biosensors, and nanotechnology [1]. This kind of polymers can self-assemble into micelles or so-called inverse micelles with desirable morphologies and properties in response to external stimuli, such as pH, ionic strength, and temperature. In recent papers, some examples of triple-stimuli responsive copolymers were described, which would independently modulate their response to each stimulus, as well as precisely regulate release profile during the combined effect of multiple stimuli [2–6]. Among various chemical and physical stimuli, phenylboronic acid (PBA) is a well known ligand

that can form reversible covalent complexes with 1,2-cis-diol compounds, such as fructose in aqueous solution [7, 8]. Based on this interaction, PBA functionalized polymers have been used for sugar sensing and drug delivery systems [9]. In particular, such polymers can potentially be developed into a self-regulating insulin delivery system to treat diabetes, where the more significant problem is the difficulty of controlling the insulin dosage. An insulin overdose can cause a low blood sugar level that may result in severe hypoglycemia [10, 11]. To this end, a lot of sugar-sensitive linear copolymers [12, 13], latices [14], capsules [15–17], and hydrogels [18–21] were synthesized. For example, Kataoka *et al.* [8] synthesized a hydrogel composed of poly(*N*-isopropylacrylamide) (PNIPAM) with PBA groups,

*Corresponding author, e-mail: tycang@mail.ahnu.edu.cn
© BME-PT

which shows an on-off regulation of insulin release in response to glucose stimulation at physiological pH.

Controlled radical polymerization methods, such as atom-transfer radical polymerization (ATRP) and reversible addition-fragmentation chain transfer (RAFT) polymerization enabling the facile synthesis of a wide range of functional copolymers with controllable block lengths [22], have been used to synthesize boronic acid-containing block copolymers. Well-defined boronic acid homo- and block copolymers were synthesized via ATRP [23–25] or RAFT [26] polymerization of styrenic boronic ester and subsequent post-polymerization deprotection of the boronic ester. Recently, Sumerlin and coworkers [3, 27] reported the synthesis of well-defined PAAPBA-*b*-PNIPAM block copolymers via direct RAFT polymerization of unprotected AAPBA and NIPAM. Such copolymer is capable of forming micelles or reverse micelles depending on the temperature, pH, and glucose concentration. However, these studies mainly focused on the characterization of their equilibrium self-assembled structures. Much less has been explored on the dissociation behavior of PAAPBA-*b*-PNIPAM micelles.

The study of the dissociation process of polymeric micelle is of fundamental importance for various applications, such as in dispersant technology and controlled drug release [28]. Polymeric micelles are expected to grow or dissolve primarily via Aniansson-Wall (AW) mechanism [29]. This mechanism, which allows change of the aggregation number only in steps consisting of addition or subtraction of individual chains into/out of the micelle, is found to have the lowest activation free energy. However, Zhang *et al.* [30] proposed that increasing the hydrophobic block length in block copolymers can transform the mechanism from unimer insertion/expulsion to micelle fusion/fission. Consequently, the micellization and dissociation of polymer has attracted considerable attention both in experimental and theoretical investigations [31–34].

In the present work, we prepared PAAPBA-*b*-PNIPAM block copolymer by direct RAFT polymerization. The micellization and dissociation transition of PAAPBA-*b*-PNIPAM in aqueous solution was systematically investigated by laser light scattering (LLS) in response to temperature, pH, and fructose.

Our aim is to understand the dissociation behavior of micelles upon external stimuli.

2. Experimental section

2.1. Materials

3-Aminophenylboronic acid was purchased from Alfa Aesar (Tianjin, China), and used as received. N-isopropylacrylamide (NIPAM, Aldrich, Shanghai, China) was recrystallized from a benzene/*n*-hexane mixture. Other chemicals were purchased from Shanghai Chemical Reagent Co. (Shanghai, China). Tetrahydrofuran (THF) was distilled from a purple sodium benzophenone ketyl solution. Acryloyl chloride, methanol and triethylamine were dried over CaCl₂ and distilled. 4,4'-Azobis(isobutyronitrile) (AIBN) was purified by recrystallization from methanol. Phosphate-buffered saline (PBS, ionic strength 0.02 M) with various pH values was prepared by dissolving KH₂PO₄, Na₂HPO₄ and Na₃PO₄ in Milli-Q water with a resistivity of 18.3 MΩ·cm. RAFT agent S-1-dodecyl-S'-(α , α' -dimethyl- α'' -acetic acid) trithiocarbonate (CTA) was synthesized as described in the literature [35]. AAPBA, PAAPBA and PAAPBA-*b*-PNIPAM were synthesized according to the literature methods [3, 27]. The polydispersity indices (M_w/M_n) of PAAPBA and PAAPBA-*b*-PNIPAM determined by Gel Permeation Chromatography (GPC) are 1.05 and 1.28, respectively.

2.2. Preparation of the micellar solutions

PAAPBA-*b*-PNIPAM (2.0 mg) dissolved in 2 mL methanol was added to 100 mL water under stirring at a constant rate by an SP100i syringe pump. The methanol was removed by evaporation under reduced pressure. For the fructose sensitivity experiments, fructose was added to the polymer solutions. The pH of solution was adjusted to desired value by adding PBS stock solution with the final concentration of the block copolymer of 2.0×10^{-5} g/mL. Each solution was incubated overnight at room temperature with continuous stirring and then was filtered through 0.45 μ m Millipore Millex-LCR filter to remove dust before the LLS measurement.

2.3. Characterizations

2.3.1. LLS measurements

All LLS measurements were conducted on an ALV/DLS/SLS-5022F spectrometer with a multi- τ digi-

tal time correlation (ALV5000, Germany) and a cylindrical 22 mW UNIPHASE He-Ne laser ($\lambda_0 = 632$ nm) as the light source. In static LLS [36], the weight-average molar mass (M_w) and the root-mean-square radius of gyration $\langle R_g^2 \rangle_z^{1/2}$ (or written as $\langle R_g \rangle$) were obtained in a very solution from the angular dependence of the absolute excess time-average scattering intensity, known as the Rayleigh ratio $R_{vv}(q)$ as shown by Equation (1):

$$\frac{KC}{R_{vv}(q)} \approx \frac{1}{M_w} \left(1 + \frac{1}{3} \langle R_g^2 \rangle_z q^2 \right) \quad (1)$$

where $K = 4\pi^2 n^2 (dn/dC)^2 / (N_A \lambda_0^4)$ and $q = 4\pi n \sin(\theta/2) / \lambda_0$ with C , dn/dC , N_A , and λ_0 being concentration of the polymer, the specific refractive index increment, the Avogadro's number, and the wavelength of light, respectively. In dynamic LLS [37], the Laplace inversion of each measured intensity-intensity time correlation function $G^{(2)}(q, t)$ in the self-beating mode can lead to a line-width distribution $G(\Gamma)$. For a diffusive relaxation, Γ is related to the translational diffusion coefficient D by $(\Gamma/q^2)_{C \rightarrow 0, q \rightarrow 0} \rightarrow D$, so that $G(\Gamma)$ can be converted into translational diffusion coefficient distribution $G(D)$ and further into hydrodynamic radius distribution $f(R_h)$ via the Stokes-Einstein equation, $R_h = k_B T / (6\pi\eta D)$, where k_B , T , and η are the Boltzmann constant, the absolute temperature, and the solvent viscosity, respectively. All DLS measurements were performed at a scattering angle (θ) of 20° . The refractive index increment (dn/dC) value of micelle was measured by using a differential refractometer developed by Wu and Xia [38].

2.3.2. GPC, NMR and TEM analyses

The polydispersity indices of PAAPBA and PAAPBA-b-PNIPAM were determined by GPC (Waters 1515, Waters Corporation, USA) using monodisperse polystyrene as the calibration standard and THF as the eluent with a flow rate of 1.0 mL/min. The proton nuclear magnetic resonance ($^1\text{H-NMR}$) spectra were recorded on a Bruker DMX-300 NMR spectrometer (Switzerland), using CD_3OD as solvent and tetramethylsilane as an internal standard. The morphology of micelle was characterized by transmission electron microscopy (TEM). Samples were collected on a TEM grid and conducted using a Tecnai G2 20 S-TWIN (Holland) microscope with an accelerating voltage of 200 kV.

3. Results and discussion

3.1. Synthesis and characterization of PAAPBA-b-PNIPAM copolymer

Polymeric boronic acids are difficult to characterize by GPC because of extremely hygroscopic property [26]. Therefore, the compositions of PAAPBA and PAAPBA-b-PNIPAM are determined from $^1\text{H-NMR}$ spectra. In the spectrum of PAAPBA-CTA (Figure 1a), the characteristic signals of both PAAPBA and CTA can be clearly observed. By calculating the intensity ratio of the signal at $\delta = 6.9\text{--}7.8$ ppm to that at $\delta = 1.16\text{--}1.26$ ppm, which are assigned to phenyl protons in PAAPBA segment and methylene protons ($-(\text{CH}_2)_{10}-$) in CTA, respectively, the degree of polymerization (DP) of PAAPBA is evaluated to be 23. From Figure 1b, the DP of PNIPAM block is determined to be 220 by comparing the intensity ratio of the signals of phenyl protons in PAAPBA and isopropyl protons in PNIPAM ($\delta = 4.0$ ppm).

3.2. Thermo-responsive property of PAAPBA-b-PNIPAM micelles

PNIPAM is one of the most popular thermo-responsive polymers, which undergoes a reversible phase transition at a lower critical solution temperature (LCST) around 32°C in water [39]. PNIPAM is soluble in water at temperature below its LCST, while PAAPBA is water insoluble in acidic or natural solution. Therefore, PAAPBA-b-PNIPAM chains can self-assemble to form a core-shell structure micelle with a hydrophobic core composed of PAAPBA and hydrophilic shell composed of PNIPAM in the lower pH solution at room temperature. To eliminate the effect of hydrophobic dodecyl group at the end of PAAPBA-b-PNIPAM chain on the self-assembly, the trithiocarbonate end-group of copolymer is cleaved by radical induced termination reaction with AIBN [40]. Figure 2 shows typical hydrodynamic radius distributions $f(R_h)$ of PAAPBA-b-PNIPAM. Only one unimodal distribution is observed at 20 and 37°C , respectively. At 20°C , an average hydrodynamic radius ($\langle R_h \rangle$) 65 nm is calculated by CONTIN analysis; correspondingly, the average radius of gyration ($\langle R_g \rangle$) of the scattering objects is 59 nm by static light scattering. It is known that the $\langle R_g \rangle / \langle R_h \rangle$ value can reveal the conformation of polymer chains or structure of particles. For random coil, hyper-branched cluster or micelle, and uniform sphere, $\langle R_g \rangle / \langle R_h \rangle$ is 1.5–1.8, 1.0–1.2, and

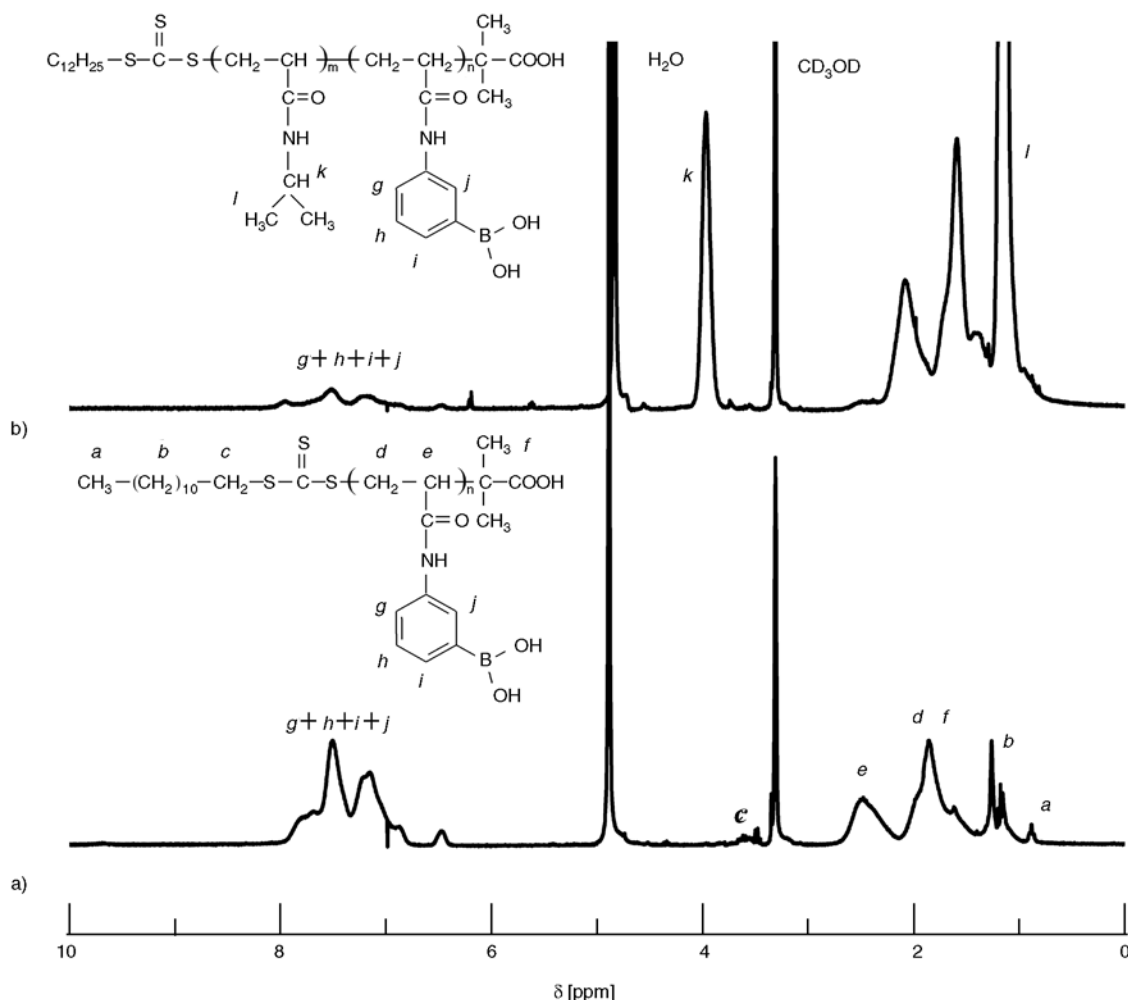


Figure 1. ^1H NMR spectra of (a) PAAPBA-CTA and (b) PAAPBA-b-PNIPAM in CD_3OD

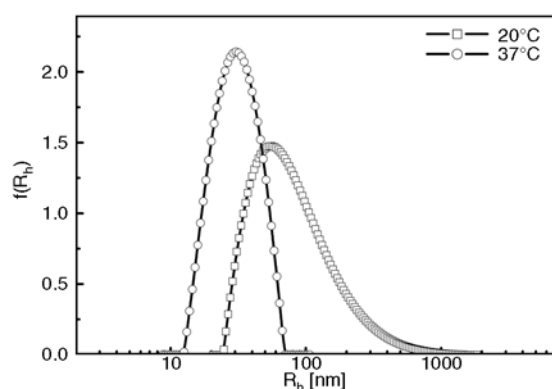


Figure 2. Typical hydrodynamic radius distribution $f(R_h)$ of PAAPBA-b-PNIPAM micelles (pH 6.2) at 20 and 37°C, respectively

~ 0.774 , respectively [41]. The ratio of $\langle R_g \rangle / \langle R_h \rangle$ is 0.91 at 20.0°C, indicating that PAAPBA-b-PNIPAM block copolymer forms micelles. However, the contour length of PAAPBA-b-PNIPAM chain is estimated to be ~ 61 nm by $L = Nl$, where N is the total

number of units, and the length per unit $l = 0.25$ nm. Considering that the chains cannot be fully stretched in solution, their size should be much less than 61 nm. We thus tentatively ascribe the formation of large irregular micelles. As the temperature increases to 37°C, the $f(R_h)$ becomes narrow with $\langle R_h \rangle = 28$ nm, suggesting the collapse of micelles. We note that besides the micelles in solution, there must be a small amount of free PAAPBA-b-PNIPAM chains, which are usually not detectable in the presence of micelles by DLS [42]. The actual morphology of the micelles has been obtained by TEM observation (Figure 3), which clearly reveals the presence of irregular micelles with average diameters of 50–65 nm at 20°C and spherical micelles with average diameters of 20–30 nm at 37°C, respectively. The micelle sizes estimated from TEM were systematically smaller than those obtained by dynamic LLS, which is reasonable considering that the for-

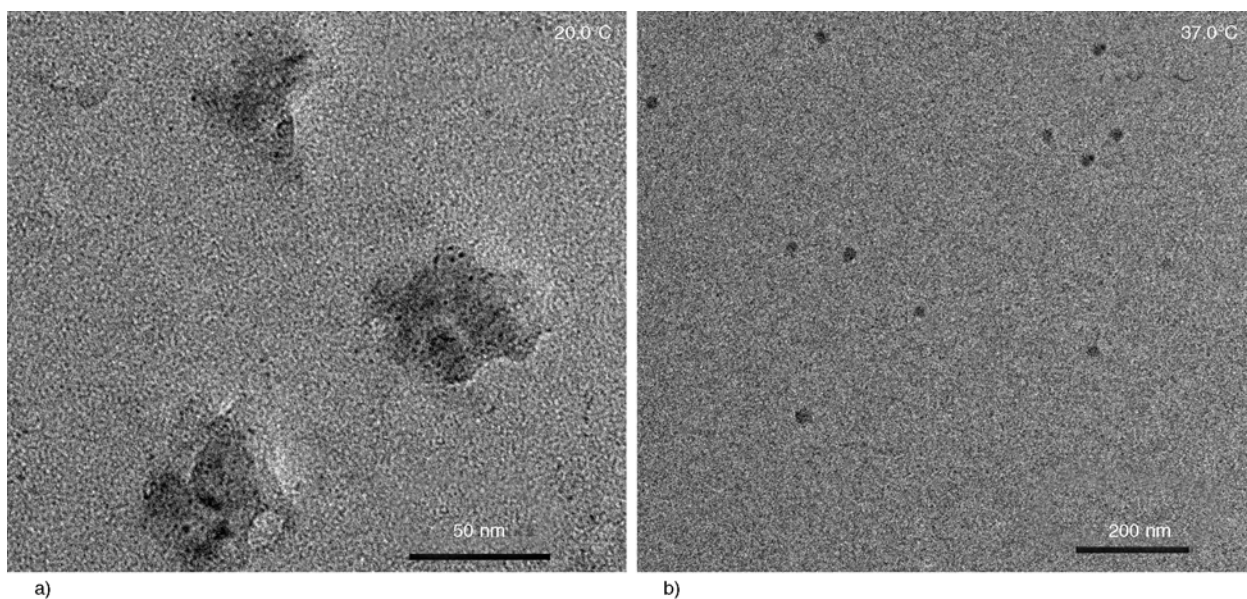


Figure 3. TEM images of PAAPBA-b-PNIPAM micelles (pH 6.2) at (a) 20°C and (b) 37°C, respectively

mer reflects conformations in the dry state, while the later reports the intensity-average dimensions of micelles in solution.

Figure 4 shows the temperature dependence of $\langle R_h \rangle$ and $\langle R_g \rangle$ of PAAPBA-b-PNIPAM micelles at pH 6.2, where almost all of the boronic acid groups would be in the uncharged form [13]. Note that LLS measurements were carried out after the solution temperature reached equilibrium. At $T < 30.0^\circ\text{C}$, both $\langle R_h \rangle$ and $\langle R_g \rangle$ slightly decrease with temperature, whereas the apparent molar mass ($M_{w,a}$) remains nearly constant (inset of Figure 4), indicating micelles gradual shrink. In the range of $30.0\text{--}34.0^\circ\text{C}$, the sharp decrease of $\langle R_h \rangle$ and $\langle R_g \rangle$ is the result of shrink and collapse of PNIPAM shell. On the contrary, $M_{w,a}$ increases from 1.05 to $1.52 \cdot 10^7$ g/mol. As we know

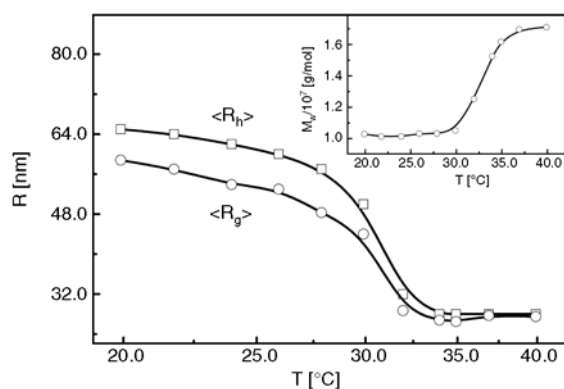


Figure 4. Temperature dependence of average hydrodynamic radius ($\langle R_h \rangle$) and average radius of gyration ($\langle R_g \rangle$) of PAAPBA-b-PNIPAM micelles at pH 6.2. The inset shows the temperature dependence of apparent molar mass ($M_{w,a}$).

that, the intrachain collapse and the interchain association compete with each other in the PNIPAM phase transition. The latter can cause significant change in $M_{w,a}$. For instance, if two micelles are associated, $M_{w,a}$ of new aggregates is nearly double that of micelles. Therefore, the small increase of $M_{w,a}$ might reflect that some free PAAPBA-b-PNIPAM chains in solution insert or small aggregates incorporate into the micelles. At the temperature above 34.0°C , $\langle R_h \rangle$ and $\langle R_g \rangle$ slightly decrease to a constant value, and $M_{w,a}$ gradually levels off. The facts show that both the intrachain contraction of PNIPAM segments and individual chain inserted into the micelles stop. Note that no precipitation occurs even when the solution was heated up to 40.0°C for 20 h, indicating that the micelles are stable.

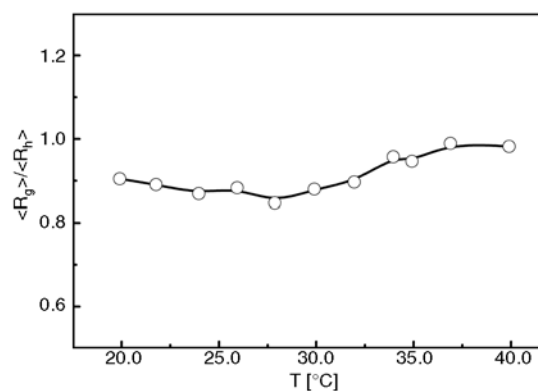


Figure 5. Temperature dependence of the ratio of average radius of gyration to average hydrodynamic radius ($\langle R_g \rangle / \langle R_h \rangle$) of PAAPBA-b-PNIPAM micelles at pH 6.2

Figure 5 shows that the ratio of $\langle R_h \rangle / \langle R_g \rangle$ is ~ 0.90 – 0.99 in the range of 20.0 – 40.0°C , further indicating that PAAPBA-*b*-PNIPAM block copolymer forms micelles at all temperatures investigated. By meticulously analyzing the ratio change, we discover it slightly increases from 0.85 to 0.99 at 28.0 – 40.0°C . The collapse of PNIPAM block causes the micellar shell density increase, which is responsible for the increase of $\langle R_h \rangle / \langle R_g \rangle$ value.

3.3. The dissociation behavior of PAAPBA-*b*-PNIPAM micelles upon pH and fructose stimulation

There is an equilibrium between the different states of a phenylboronic acid derivative. As shown in Figure 6, with an increase in pH value, the neutral PBA can be ionized by combining with OH^- to form a relatively hydrophilic but unstable phenylborate anion. Worth noticing is that the charged phenylborate can form a more favorable charged and stable phenylborate ester by complex with 1,2-cis-diol such as glucose in aqueous medium, and further addition of diol induces the shift of the equilibrium in the direction of increasing phenylborate ester [8, 9, 18]. Consequently, the water solubility of a polymer with PBA residues is tunable by changes in both pH and diol concentration.

Figure 7a shows pH dependence of $f(R_h)$ of PAAPBA-*b*-PNIPAM micelles in the absence of

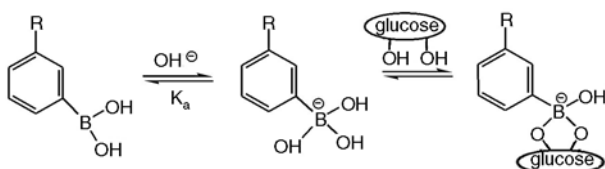


Figure 6. Complexation equilibrium between PBA derivative and 1,2-diol

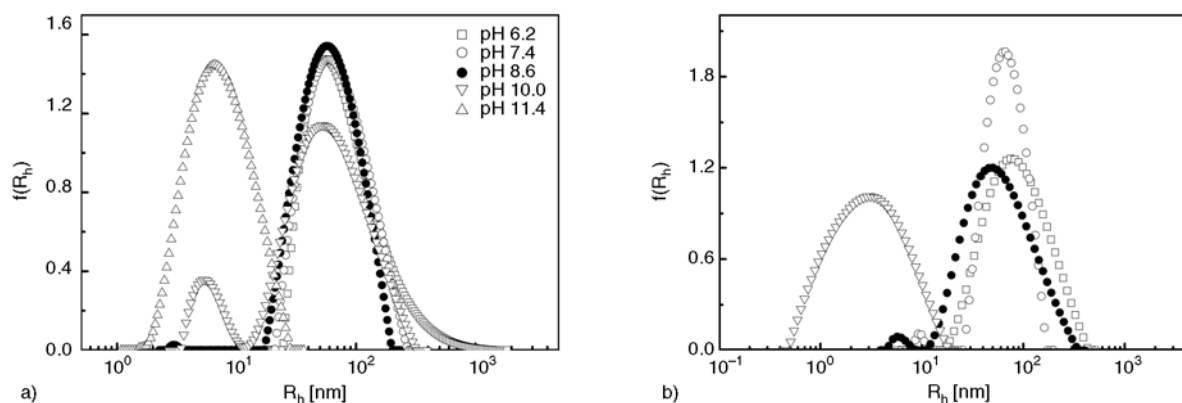


Figure 7. pH dependence of hydrodynamic radius distributions ($f(R_h)$) of PAAPBA-*b*-PNIPAM copolymer in (a) the absence and (b) the presence of fructose ($C_{\text{fructose}} = 1.0 \text{ mg/mL}$) at 20°C

fructose at 20.0°C . Compared with the micelles at pH 6.2 , the $f(R_h)$ for the micelles at pH 7.4 do not markedly change. Interestingly, a bimodal distribution can be observed at pH 8.6 and 10.0 , respectively. The big peak at ~ 59 nm corresponding to the copolymer micelles is almost independent of pH, suggesting that the micelle size remains unchanged. The new peak located at ~ 3 nm is attributed to free chains of PAAPBA-*b*-PNIPAM. This bimodal distribution strongly suggests the coexistence of micelles and PAAPBA-*b*-PNIPAM free chains. As pH increases to 10.0 , the $f(R_h)$ of the micelles decreases, while the scattering intensity of unimers increases. When the pH value is adjusted to 11.4 , we find only one peak located at ~ 5 nm, implying the complete dissociation of micelles. Since the pK_a of AAPBA in PAAPBA-*b*-PNIPAM copolymer is around 8.2 [9, 10], phenylboronic acid group is partially charged, and completely charged at pH 8.6 and 10.0 , respectively [19]. As a result, more individual chains are dissociated from the copolymer micelles at higher pH. Note that even if pH is increased up to 10.0 , which is much higher than the pK_a of PAAPBA, the micelles do not dissociate completely. Wang *et al.* [9] have reported that the micelles containing AAPBA block disassemble at pH 11.3 . This can be ascribed to the unique core-shell structure of micelles, where phenylborate moieties are spatially trapped in the micellar core. In the ionization process of PBA, the concentration of anionic charges in the immediate vicinity of phenylborates is increased and thus further dissociation of phenylborates is impeded. So much more OH^- in the solution is needed to further ionize PBA groups in the inner core [9, 10].

The effect of fructose on the dissociation behavior of PAAPBA-b-PNIPAM micelles is studied by adding fructose ($C_{\text{fructose}} = 1.0 \text{ mg/mL}$) to above copolymer solution with different pH values. As shown in Figure 7b, one similar unimodal distribution is observed at pH 6.2 along with the peak shifting to the right direction, indicated that the micelles are swollen. At pH 7.4 and 8.6, some PAAPBA-b-PNIPAM chains are dissociated from micelles, reflecting in a new peak; especially, at pH 10.0, only one peak with $R_h \sim 3 \text{ nm}$ appears, suggesting that micelles are disappeared from the solution. As discussed above, the ionized PBA group number increases with pH, and the charged PBA is thermodynamically favorable to bind with fructose to form phenylborate esters. As a result, the hydrophilicity of the micellar core increases with the addition of fructose, resulting in swelling and gradual disaggregation of the micelles.

Figure 8 shows the variation of R_h of PAAPBA-b-PNIPAM micelles with or without fructose under different pH, where R_h is corresponding to the peak shown in Figure 7. Clearly, increasing pH dramatically decreases R_h with the addition of fructose. On the other hand it causes R_h relatively small change in the absence of fructose. At pH 6.2 and 7.4, the presence of fructose increases the hydrophilicity of copolymer, and leads to the micelles swelling, reflecting in R_h increase, respectively. However, the R_h decreases at pH 8.4. Ge *et al.* [19] reported that the size of NIPAM-co-AAPBA microgel decreases with the addition of glucose. They attributed that glucose forms bidentate complexes with boronic acid groups and cross-links the segments between two chemical cross-linking sites,

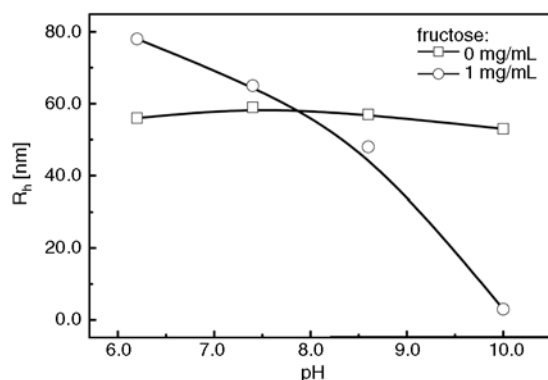


Figure 8. pH dependence of hydrodynamic radius (R_h) of PAAPBA-b-PNIPAM micelles (corresponding to the peaks shown in Figure 7) with and without fructose at 20.0°C

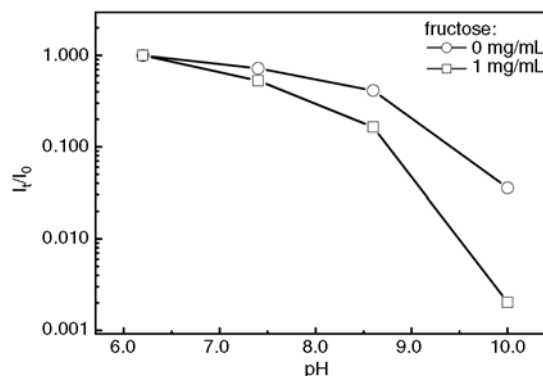


Figure 9. pH dependence of the relative scattering intensities (I_t/I_0) for PAAPBA-b-PNIPAM copolymer with and without fructose at 20.0°C, where I_0 represents the scattering intensity at pH 6.2, and I_t represents the scattering intensity at the specific pH.

leading the microgels to shrink. It should be pointed out that fructose can only form mono (boronate) complexes with PBA group [18, 43]. Accordingly, the decrease in the micellar size is maybe because of the dissociation of unimer chains out of micelles. Figure 9 shows pH dependence of the relative scattering intensities (I_t/I_0) for PAAPBA-b-PNIPAM micelles with and without fructose at 20.0°C, where I_0 represents the scattering intensity of micelles at pH 6.2 in the absence of fructose, and I_t represents the scattering intensity at the specific pH. It is well known that the scattering intensity is proportional to the square of the mass of a scattering object. The transition between micelles and individual chains can cause a significant change of I_t . For the micelle solution without fructose, the ratio of I_t/I_0 decreases as pH increase. In addition, this tendency becomes more significant when fructose is added. This further demonstrates that the addition of fructose is in favor of the formation of hydrophilic fructose phenylborate esters and promotes the swelling and then dissociation of the micelles. As fructose is added to pH 10.0 solution, the effective solubility of PAAPBA segment leads to the complete dissociation of micelles.

In the present work, both the number and aggregation number (i.e. $M_{w,a}$) of micelles reduction can induce the scattering intensity to decrease. We think that the reduction of $M_{w,a}$ leads to both the ratio of I_t/I_0 and the R_h of micelles decrease in the presence of fructose. As for the changes in R_h and the ratio of I_t/I_0 with increasing pH in the absence of fructose, these are because of the simultaneous

swelling and dissociation of micelles. Namely, the unimers are gradually expelled out of the micelles with the increase of pH and the addition of fructose. Furthermore, in the term of PAAPBA-*b*-PNIPAM structure, the DP of PAAPBA and PNIPAM block is 23 and 220, respectively. The diblock copolymers with longer shell-block lengths have a lower potential barrier for chain expulsion from micelles, which promotes more rapid chain exchange between micelles and solution [28, 30]. Accordingly, our results confirm that the micelle to unimer transformation process proceeds mainly via the unimer expulsion mechanism.

4. Conclusions

PAAPBA-*b*-PNIPAM block copolymers have been successfully synthesized by direct RAFT polymerization. Micelles self-assembled from PAAPBA-*b*-PNIPAM exhibit temperature-, pH- and fructose-sensitivity. Increasing the temperature to the LCST of PNIPAM leads to the micelles collapse. Adjustment of the solution pH from 6.2 to 10.0 at 20°C can result in the progressive dissociation of the micelles. Moreover, the addition of fructose increases the level of micelle dissociation. At pH 10.0 and the concentration of fructose 1 mg/mL, the micelles completely dissociate to unimers. These results reveal that the main route of micelle dissociation involves step-by-step expulsion of unimers, namely, the dissociation of micelle via A-W mechanism. Owing to its property of the multiple micellization and dissociation transitions, PAAPBA-*b*-PNIPAM holds great promise in designing stimuli-induced controlled release supports.

Acknowledgements

The financial support of the Natural Science Foundation of Anhui Province, China (11040606M61) and the Natural Science Foundation of the Anhui Higher Education Institutions of China (KJ2011A137, KJ2012A126) are gratefully acknowledged.

References

- [1] Rapoport N.: Physical stimuli-responsive polymeric micelles for anti-cancer drug delivery. *Progress in Polymer Science*, **32**, 962–990 (2007).
DOI: [10.1016/j.progpolymsci.2007.05.009](https://doi.org/10.1016/j.progpolymsci.2007.05.009)

- [2] Xia F., Ge H., Hou Y., Sun T., Chen L., Zhang G., Jiang L.: Multiresponsive surfaces change between superhydrophilicity and superhydrophobicity. *Advanced Materials*, **19**, 2520–2524 (2007).
DOI: [10.1002/adma.200602334](https://doi.org/10.1002/adma.200602334)
- [3] Roy D., Cambre J. N., Sumerlin B. S.: Triply-responsive boronic acid block copolymers: Solution self-assembly induced by changes in temperature, pH, or sugar concentration. *Chemical Communication*, 2106–2108 (2009).
DOI: [10.1039/b900374f](https://doi.org/10.1039/b900374f)
- [4] Yu Y-Y., Tian F., Wei C., Wang C-C.: Facile synthesis of triple-stimuli (photo/pH/thermo) responsive copolymers of 2-diazo-1,2-naphthoquinone-mediated poly(*N*-isopropylacrylamide-*co*-*N*-hydroxymethylacrylamide). *Journal of Polymer Science Part A: Polymer Chemistry*, **47**, 2763–2773 (2009).
DOI: [10.1002/pola.23357](https://doi.org/10.1002/pola.23357)
- [5] Klaikherd A., Nagamani C., Thayumanavan S.: Multi-stimuli sensitive amphiphilic block copolymer assemblies. *Journal of the American Chemical Society*, **131**, 4830–4838 (2009).
DOI: [10.1021/ja809475a](https://doi.org/10.1021/ja809475a)
- [6] Jin Q., Lv L-P., Liu G-Y., Xu J-P., Ji J.: Phenylboronic acid as a sugar- and pH-responsive trigger to tune the multiple micellization of thermo-responsive block copolymer. *Polymer*, **51**, 3068–3074 (2010).
DOI: [10.1016/j.polymer.2010.04.061](https://doi.org/10.1016/j.polymer.2010.04.061)
- [7] Kataoka K., Miyazaki H., Okano T., Sakurai Y.: Sensitive glucose-induced change of the lower critical solution temperature of poly[*N,N*-(dimethylacrylamide)-*co*-3-(acrylamido)-phenylboronic acid] in physiological saline. *Macromolecules*, **27**, 1061–1062 (1994).
DOI: [10.1021/ma00082a028](https://doi.org/10.1021/ma00082a028)
- [8] Kataoka K., Miyazaki H., Bunya M., Okano T., Sakurai Y.: Totally synthetic polymer gels responding to external glucose concentration: Their preparation and application to on-off regulation of insulin release. *Journal of the American Chemical Society*, **120**, 12694–12695 (1998).
DOI: [10.1021/ja982975d](https://doi.org/10.1021/ja982975d)
- [9] Wang B., Ma R., Liu G., Liu X., Gao Y., Shen J., An Y., Shi L.: Effect of coordination on the glucose-responsiveness of PEG-*b*-(PAA-*co*-PAAPBA) micelles. *Macromolecular Rapid Communications*, **31**, 1628–1634 (2010).
DOI: [10.1002/marc.201000164](https://doi.org/10.1002/marc.201000164)
- [10] Matsumoto A., Ikeda S., Harada A., Kataoka K.: Glucose-responsive polymer bearing a novel phenylborate derivative as a glucose-sensing moiety operating at physiological pH conditions. *Biomacromolecules*, **4**, 1410–1416 (2003).
DOI: [10.1021/bm034139o](https://doi.org/10.1021/bm034139o)
- [11] Ravaine V., Ancla C., Catargi B.: Chemically controlled closed-loop insulin delivery. *Journal of Controlled Release*, **132**, 2–11 (2008).
DOI: [10.1016/j.jconrel.2008.08.009](https://doi.org/10.1016/j.jconrel.2008.08.009)

- [12] Jin X., Zhang X., Wu Z., Teng D., Zhang X., Wang Y., Wang Z., Li C.: Amphiphilic random glycopolymer based on phenylboronic acid: Synthesis, characterization, and potential as glucose-sensitive matrix. *Biomacromolecules*, **10**, 1337–1345 (2009). DOI: [10.1021/bm8010006](https://doi.org/10.1021/bm8010006)
- [13] Shiomori K., Ivanov A. E., Galaev G. Y., Kawano Y., Mattiasson B.: Thermoresponsive properties of sugar sensitive copolymer of *N*-isopropylacrylamide and 3-(acrylamido)phenylboronic acid. *Macromolecular Chemistry and Physics*, **205**, 27–34 (2004). DOI: [10.1002/macp.200300019](https://doi.org/10.1002/macp.200300019)
- [14] Cannizzo C., Amigoni-Gerbier S., Larpent C.: Boronic acid-functionalized nanoparticles: Synthesis by microemulsion polymerization and application as a re-usable optical nanosensor for carbohydrates. *Polymer*, **46**, 1269–1276 (2005). DOI: [10.1016/j.polymer.2004.11.052](https://doi.org/10.1016/j.polymer.2004.11.052)
- [15] Levy T., Déjugnat C., Sukhorukov G. B.: Polymer microcapsules with carbohydrate-sensitive properties. *Advanced Functional Materials*, **18**, 1586–1594 (2008). DOI: [10.1002/adfm.200701291](https://doi.org/10.1002/adfm.200701291)
- [16] De Geest B. G., Jonas A. M., Demeester J., De Smedt S. C.: Glucose-responsive polyelectrolyte capsules. *Langmuir*, **22**, 5070–5074 (2006). DOI: [10.1021/la053368o](https://doi.org/10.1021/la053368o)
- [17] Lapeyre V., Renaudie N., Dechezelles J-F., Saadaoui H., Ravaine S., Ravaine V.: Multiresponsive hybrid microgels and hollow capsules with a layered structure. *Langmuir*, **25**, 4659–4667 (2009). DOI: [10.1021/la9003438](https://doi.org/10.1021/la9003438)
- [18] Zhang Y., Guan Y., Zhou S.: Synthesis and volume phase transitions of glucose-sensitive microgels. *Biomacromolecules*, **7**, 3196–3201 (2006). DOI: [10.1021/bm060557s](https://doi.org/10.1021/bm060557s)
- [19] Ge H., Ding Y., Ma C., Zhang G.: Temperature-controlled release of diols from *N*-isopropylacrylamide-*co*-acrylamidophenylboronic acid microgels. *The Journal of Physical Chemistry B*, **110**, 20635–20639 (2006). DOI: [10.1021/jp060914t](https://doi.org/10.1021/jp060914t)
- [20] Chen W., Pelton R., Leung V.: Solution properties of polyvinylamine derivatized with phenylboronic acid. *Macromolecules*, **42**, 1300–1305 (2009). DOI: [10.1021/ma802402z](https://doi.org/10.1021/ma802402z)
- [21] Liu P., Luo Q., Guan Y., Zhang Y.: Drug release kinetics from monolayer films of glucose-sensitive microgel. *Polymer*, **51**, 2668–2675 (2010). DOI: [10.1016/j.polymer.2010.04.011](https://doi.org/10.1016/j.polymer.2010.04.011)
- [22] McCormick C. L., Lowe A. B.: Aqueous RAFT polymerization: Recent developments in synthesis of functional water-soluble (co)polymers with controlled structures. *Accounts of Chemical Research*, **37**, 312–325 (2004). DOI: [10.1021/ar0302484](https://doi.org/10.1021/ar0302484)
- [23] Qin Y., Cheng G., Sundararaman A., Jäkle F.: Well-defined boron-containing polymeric lewis acids. *Journal of the American Chemical Society*, **124**, 12672–12673 (2002). DOI: [10.1021/ja020773i](https://doi.org/10.1021/ja020773i)
- [24] Qin Y., Sukul V., Pagakos D., Cui C., Jäkle F.: Preparation of organoboron block copolymers via ATRP of silicon and boron-functionalized monomers. *Macromolecules*, **38**, 8987–8990 (2005). DOI: [10.1021/ma051615p](https://doi.org/10.1021/ma051615p)
- [25] Kim K. T., Cornelissen J. J. L. M., Nolte R. J. M., van Hest J. C. M.: A polymersome nanoreactor with controllable permeability induced by stimuli-responsive block copolymers. *Advanced Materials*, **21**, 2787–2791 (2009). DOI: [10.1002/adma.200900300](https://doi.org/10.1002/adma.200900300)
- [26] Cambre J. N., Roy D., Gondi S. R., Sumerlin B. S.: Facile strategy to well-defined water-soluble boronic acid (co)polymers. *Journal of the American Chemical Society*, **129**, 10348–10349 (2007). DOI: [10.1021/ja074239s](https://doi.org/10.1021/ja074239s)
- [27] Roy D., Cambre J. N., Sumerlin B. S.: Sugar-responsive block copolymers by direct RAFT polymerization of unprotected boronic acid monomers. *Chemical Communications*, **23**, 2477–2479 (2008). DOI: [10.1039/b802293c](https://doi.org/10.1039/b802293c)
- [28] Li Z., Dormidontova E. E.: Kinetics of diblock copolymer micellization by dissipative particle dynamics. *Macromolecules*, **43**, 3521–3531 (2010). DOI: [10.1021/ma902860j](https://doi.org/10.1021/ma902860j)
- [29] Aniansson E. A. G., Wall S. N.: Kinetics of step-wise micelle association. Correction and improvement. *Journal of Physical Chemistry*, **79**, 857–858 (1975). DOI: [10.1021/j100575a019](https://doi.org/10.1021/j100575a019)
- [30] Zhang J., Xu J., Liu S.: Chain-length dependence of diblock copolymer micellization kinetics studied by stopped-flow pH-jump. *Journal of Physical Chemistry Part B*, **112**, 11284–11291 (2008). DOI: [10.1021/jp803700n](https://doi.org/10.1021/jp803700n)
- [31] Halperin A., Alexander S.: Polymeric micelles: Their relaxation kinetics. *Macromolecules*, **22**, 2403–2412 (1989). DOI: [10.1021/ma00195a069](https://doi.org/10.1021/ma00195a069)
- [32] Dormidontova E. E.: Micellization kinetics in block copolymer solutions: Scaling model. *Macromolecules*, **32**, 7630–7644 (1999). DOI: [10.1021/ma9809029](https://doi.org/10.1021/ma9809029)
- [33] Nyrkova I. A., Semenov A. N.: On the theory of micellization kinetics. *Macromolecular Theory and Simulations*, **14**, 569–585 (2005). DOI: [10.1002/mats.200500010](https://doi.org/10.1002/mats.200500010)
- [34] Zhu Z., Xu J., Zhou Y., Jiang X., Armes S. P., Liu S.: Effect of salt on the micellization kinetics of pH-responsive abc triblock copolymers. *Macromolecules*, **40**, 6393–6400 (2007). DOI: [10.1021/ma070978h](https://doi.org/10.1021/ma070978h)

- [35] Lai J. T., Filla D., Shea R.: Functional polymers from novel carboxyl-terminated trithiocarbonates as highly efficient RAFT agents. *Macromolecules*, **35**, 6754–6756 (2002).
DOI: [10.1021/ma020362m](https://doi.org/10.1021/ma020362m)
- [36] Berne B. J., Pecora R.: *Dynamic light scattering*. Wiley, New York (1976).
- [37] Chu B., *Laser light scattering*. Academic Press, New York (1991).
- [38] Wu C., Xia K-Q.: Incorporation of a differential refractometer into a laser light-scattering spectrometer. *Review of Scientific Instruments*, **65**, 587–590 (1994).
DOI: [10.1063/1.1145121](https://doi.org/10.1063/1.1145121)
- [39] Winnik F. M.: Fluorescence studies of aqueous solutions of poly(N-isopropylacrylamide) below and above their LCST. *Macromolecules*, **23**, 233–242 (1990).
DOI: [10.1021/ma00203a040](https://doi.org/10.1021/ma00203a040)
- [40] Perrier S., Takolpuckdee P., Mars C. A.: Reversible addition–fragmentation chain transfer polymerization: End group modification for functionalized polymers and chain transfer agent recovery. *Macromolecules*, **38**, 2033–2036 (2005).
DOI: [10.1021/ma047611m](https://doi.org/10.1021/ma047611m)
- [41] Douglas J. F., Roovers J., Freed K. F.: Characterization of branching architecture through ‘universal’ ratios of polymer solution properties. *Macromolecules*, **23**, 4168–4180 (1990).
DOI: [10.1021/ma00220a022](https://doi.org/10.1021/ma00220a022)
- [42] Troll K., Kulkarni A., Wang W., Darko C., Koumba A. M. B., Laschewsky A., Müller-Buschbaum P., Papadakis C. M.: The collapse transition of poly(styrene-*b*-(*N*-isopropyl acrylamide)) diblock copolymers in aqueous solution and in thin films. *Colloid and Polymer Science*, **286**, 1079–1092 (2008).
DOI: [10.1007/s00396-008-1871-5](https://doi.org/10.1007/s00396-008-1871-5)
- [43] Alexeev V. L., Sharma A. C., Goponenko A. V., Das S., Lednev I. K., Wilcox C. S., Finegold D. N., Asher S. A.: High ionic strength glucose-sensing photonic crystal. *Analytical Chemistry*, **75**, 2316–2323 (2003).
DOI: [10.1021/ac030021m](https://doi.org/10.1021/ac030021m)

Response surface analysis of structural, mechanical, and permeability properties of polyethylene/ Na^+ -montmorillonite composites, prepared by slurry-fed melt intercalation

S. I. S. Shahabadi^{1,2*}, H. Garmabi¹

¹Mahshahr Campus, Amirkabir University of Technology, Mahshahr, Iran

²Department of Polymer Engineering and Color Technology, Amirkabir University of Technology, No. 242, Hafez Ave., Tehran, Iran

Received 30 December 2011; accepted in revised form 27 February 2012

Abstract. Samples were produced by injecting Na^+ -montmorillonite (Na^+ -MMT) slurry into a co-rotating twin-screw extruder. Na^+ -MMT was modified inside the extruder, in an *in-situ* process, and blended with the LDPE/LLDPE in melt state. Three different types of alkyl ammonium salt (ALAMS) were used as modifier to study the effect of chemical composition and chain length of ALAMS on the dispersion of nanoparticles. Also, the effect of nanoclay content on structural, mechanical, and permeability properties of the samples was investigated. To translate the data into intelligible trends, response surface method was utilized to analyze the effects of the factors on the results. Moreover, transmission electron microscopy was implemented to observe the dispersion of nanoclay platelets. The results suggested that the chain length of ALAMS dramatically affects its ability to modify nanoclay platelets. What is more, while nanoclay increase deteriorates nanoparticles dispersion, it brings about better mechanical and gas barrier properties. The improvement in the properties was higher than those of nanocomposites prepared by conventional method. By studying the effects of feeding rate on nanoclay dispersion, we proved that unlike conventional melt intercalation, water-assisted melt intercalation is controlled by diffusion rather than shear stress. In the end, we proposed a mechanism for this process.

Keywords: nanocomposites, nanoclay slurry, melt intercalation, polyethylene

1. Introduction

Low density polyethylene (LDPE) and linear low density polyethylene (LLDPE) blends have gained remarkable attention in packaging film industries. Although these two polymers and their blends are among the most multi-purpose polymers, their lack of strength and stiffness along with poor heat resistance are problematic [1]. To eliminate these drawbacks and to prepare materials with improved properties, varieties of inorganic nanoparticles have been added to these polymers, among which nanoclay platelets have gained special interest [2, 3].

This special interest is an outgrowth of two particular characteristics of nanoclay particles: first is the ability to disperse into individual layers, the second is the ability to engineer their surface chemistry through ion exchange reactions [4, 5]. When compared to their unloaded counterparts, polymeric nanocomposites demonstrate drastic improvements in physical and mechanical properties. Adding nanoclay also brings forth better gas barrier and flame retardancy properties [6, 7]. There are various methods to prepare nanocomposites, among which melt intercalation has attracted a lot of attention. Melt

*Corresponding author, e-mail: sis.shahabadi@gmail.com

intercalation involves annealing, mainly under shear stress, a mixture of polymer and nanoclay particles above the softening point of the polymer. Owing to the absence of organic solvents, this method is environmentally benign and also compatible with current industrial process, such as extrusion and injection molding [8]. A major modification to melt intercalation method was carried out by Korbee and Van Geenen [9], in which the pristine nanoclay particles and PA6 pellets were introduced into the extruder, and water was then injected directly into the extruder downstream. After interactions with the melt compound, water was evacuated further downstream via a vacuum pump. The presence of water weakens the interaction between the nanoclay platelets and brings forth an increase in the gallery spacing. In case of high surface energy polymers, e.g., polyamides, water can also reduce matrix viscosity and thus add to the chain mobility. Both of these effects facilitate polymer chain penetration between the nanoclay platelets. This modification makes the need for the use of nanoclay modifiers unnecessary for high surface energy polymers. Even if the use of modifiers is unavoidable, i.e., in case of hydrophobic polymers like polyolefins, this method still brings about improved, if not similar, results and offers *in-situ* nanoclay modification, which is less cumbersome and costly than pre-modification process and provides us with more process flexibility and less health hazard [10].

Water-assisted melt intercalation can be employed in three different ways: slurry injection, solution injection, and water injection. According to Molajvadi and Garmabi [11], using slurry injection for nanocomposite production would result in the best mechanical properties. Plus, this method can be used to produce nanocomposites from a wide range of polymers and modifiers. But, it requires slurry preparation process and higher amount of water; higher amount of injected water may cause technical problems. There is also a limit for nanoclay content, 5 wt%, and feeding rate, 2 kg/h in this study. Moreover, the slurry may even stick to the screw and cause other technical difficulties. Solution injection, on the other hand, requires relatively less amount of water. Because the modification process occurs in water [12], this method provides better chance for nanoclay modification [13]. The addition of more amount of nanoclay is possible and higher outputs

can be achieved. But, modifier solution process is required; and, this process is limited only to modifiers that are water-soluble under ambient conditions. Interestingly, water injection method does not need slurry nor solution preparation processes and requires less amount of water [14]. The addition of more amount of nanoclay is possible and higher outputs can be achieved. But, it brings forth lower chance for nanoclay modification. As a result, this method is best used only for high surface energy polymers [15, 16]. It should also be noted that the use of water in producing polymeric nanocomposites is not only limited to polymer/nanoclay composites; this method can be employed to produce polymeric composites from other particles as well [17]. Table 1 summarizes these findings, based on which we decided to utilize slurry injection method for this study.

The slurry-fed melt intercalation process has not been used to produce LDPE/LLDPE nanocomposites. In this study, Octadecyl trimethyl ammonium chloride (OTAC), dodecyl trimethyl ammonium chloride (DTAC), and dodecyl trimethyl ammonium bromide (DTAB) were used to study the effect of chemical composition and chain length of modifiers on the dispersion of nanoparticles. By comparing the results between DTAC- and DTAB-modified samples, the effect of chemical composition, chlorine or bromine, can be studied. Similarly, the comparison between DTAC- and OTAC-modified samples will show the effect of modifier chain length on the dispersion of nanoparticles. Table 2 presents some information regarding the three alkyl ammonium salt (ALAMS) types.

Furthermore, Hasegawa *et al.* [18] and Kato *et al.* [12] claimed that water-assisted melt intercalation process is quite different from conventional one: In conventional melt intercalation, polymer chains intercalate into the galleries of the stacked layered silicates and the silicate layers exfoliate into polymer matrix; this largely occurs under shear stress. On the other hand, in water-assisted process the exfoliated silicate layers in water are fixed into the polymer matrix without aggregation; this means that shear stress has no consequential role in the dispersion of the nanoparticles, and diffusion plays the important role. To examine this theory, we decided to study the effect of feeding rate on the nanoclay dispersion and the properties of samples.

Because, by changing feeding rate, we can change the imposed shear stress on and the residence time of the materials inside the extruder; the inverse relationship between the shear stress and the residence time should be noticed. To get a notion on how feeding rate affects the residence time of the materials,

the effect of feeding rate on the residence time of LDPE/LLDPE is gathered in Table 3. For this theory to hold true, i.e., the process is diffusion-controlled rather than shear-controlled, better nanoclay dispersion must emerge from lower feeding rates, i.e., higher residence time and higher chance for

Table 1. Schematic view, advantages, and disadvantages of the three different types of water-assisted melt intercalation

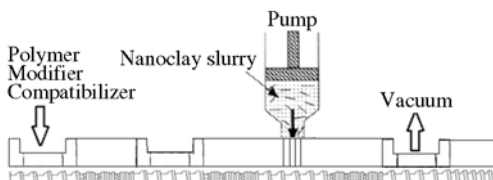
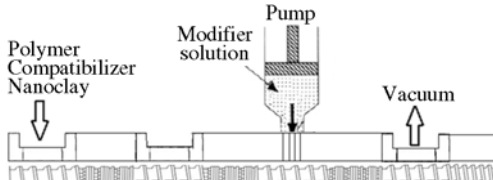
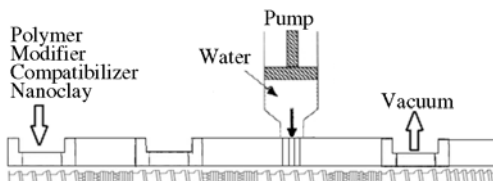
Method	Schematic view of the process and advantages	Disadvantages
slurry injection	 <p>1 – better nanoclay dispersion and mechanical properties 2 – can be used for a wide range of polymers and modifiers</p>	<p>1 – higher amount of water is needed 2 – nanoclay content limit in slurry (up to 5 wt%) 3 – slurry may stick to the screw 4 – slurry preparation process is needed 5 – only low outputs are available</p>
solution injection	 <p>1 – better chance for nanoclay modification 2 – better results than water injection 3 – less water is needed than slurry injection 4 – higher outputs and nanoclay contents are available</p>	<p>1 – more water is needed than water injection 2 – limited only to modifiers that are water-soluble under ambient conditions 3 – solution preparation process is needed</p>
water injection	 <p>1 – less amount of water is needed 2 – neither slurry nor solution preparation processes are needed 3 – higher outputs and nanoclay contents are available</p>	<p>1 – lower chance for nanoclay modification 2 – best suited for high surface energy polymers, for which no chemical modification is needed</p>

Table 2. General information of the studied ALAMS types

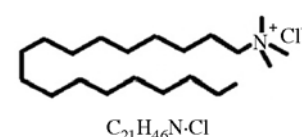
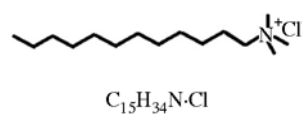
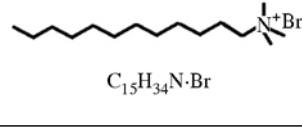
ALAMS type	Chemical Formula	More information
OTAC	 <p>$C_{21}H_{46}N \cdot Cl$</p>	<p>Synonyms: Steartrimonium chloride; Stearyl trimethyl ammonium chloride; Trimethyloctadecylammonium chloride; Aliquat 7 Molecular weight: 348.05 Soluble in hot water</p>
DTAC	 <p>$C_{15}H_{34}N \cdot Cl$</p>	<p>Synonyms: N,N,N-Trimethyl-1-dodecanaminium chloride; Trimethyl-1-dodecanaminium chloride; Lauryl trimethyl ammonium chloride; Laurtrimonium chloride Molecular weight: 263.89 Water soluble</p>
DTAB	 <p>$C_{15}H_{34}N \cdot Br$</p>	<p>Synonyms: Lauryltrimethylammonium bromide; Dodecyltrimethylammonium bromide; Laurtrimonium bromide Molecular weight: 308.34 Water soluble</p>

Table 3. The effect of feeding rate on the residence time of the LDPE/LLDPE blend

Feeding rate [kg/h]	Color change initiation time [s]	Color change termination time [s]	Average residence time [s]
1	180	350	265
1.5	110	240	175
2	96	152	124

diffusion. Lastly, the role of nanoclay content on the properties of the samples and nanoclay dispersion is worth studying.

For the sake of proper interpretation and integration of all the data, a designed set of experiments is required. By using experimental design, it will be much simpler to analyze the effects of the factors on the morphology, mechanical, and permeability properties of the samples, to observe the trends, and to draw conclusions. Among the variety of experimental designs, response surface method was best compatible with our experimental and material conditions.

For these reasons, in this study, we produced LDPE/LLDPE/nanoclay samples in a co-rotating twin-screw extruder equipped with slurry injection system from LDPE/LLDPE blends, polyethylene maleic anhydride (PEMA), three different types of ALAMS, and Na⁺-montmorillonite (Na⁺-MMT) dispersed in water. The objective of this paper is to analyze, by means of response surface method, the effect of three key factors, i.e., modifier type, feeding rate, and nanoclay content, on the structural, mechanical, and permeability properties of the samples.

2. Experimental

2.1. Materials

Low density polyethylene (LDPE, 2101TN47), density = 0.921 g/cm³, was kindly provided by Laleh Petrochemical Co. (Mahshahr, Khuzestan, Iran). Linear low density polyethylene (LLDPE, 0209AA), density = 0.920 g/cm³, was purchased from Amirkabir Petrochemical Co. (Mahshahr, Khuzestan, Iran). The melt flow index (MFI), measured at 190°C with 2.16 kg load, was 0.85 g/10 min for both LDPE and LLDPE. Maleic anhydride modified linear low density polyethylene (PEMA, Orevac[®]18302N), density = 0.912 g/cm³, with a maleic anhydride content of 0.2 wt% was supplied by Arkema Inc. (Paris, France) to be used as compatibilizer, the MFI of

PEMA used was 1.2 g/10 min. Na⁺-montmorillonite (Na⁺-MMT, Cloisite[®] Na⁺), density = 2.86 g/cm³, was purchased from Southern Clay Products (Gonzales, Texas, USA). The cation exchange capacity of Na⁺-MMT was 95 meq/100 g. Alkyl ammonium salts were purchased from Xiamen Pioneer Technology Inc. (Xiamen, Fujian, China). All the materials were used as received.

2.2. Design of experiments

Response surface methods are used to examine the relationship between one or more response variables and a set of factors. These methods are often employed after ‘vital few’ controllable factors are identified. In addition to process optimization, which is not discussed in this paper, these methods enable us to produce an approximate continuous surface for the discrete results. This will help us to integrate the effects of two factors into one 3D plot, making it easier to observe the trends and possible to detect the interaction between the factors. Among different response surface methods, Box-Behnken method was found to be best compatible with our experimental criteria [19–22].

We considered feeding rate, nanoclay content, and ALAMS type as ‘vital few’ controllable factors. The properties used as responses include: tensile-modulus increase, reduction in oxygen permeability, and *d*-spacing of nanoparticles in the samples. A quadratic model was used to approximate the responses continuously. Throughout this paper, samples will be named the way below:

- 1 – The letters indicate the ALAMS type. OC, DC, and DB will stand for OTAC, DTAC, and DTAB, respectively.
- 2 – The figure on the left-hand side of the forward slash will represent nanoclay content in [wt%].
- 3 – The figure on the right-hand side of the forward slash will represent feeding rate in [kg/h].

Note: Samples No. 7, 9, and 11 have exactly the same design and are for reproducibility analysis. The extra figure that is added to the end of their names is simply for distinction.

Example: DB5/1.5 is the name of the sample that contains 5 wt% nanoclay and has been prepared at 1.5 kg/h feeding rate with DTAB as nanoclay modifier.

The full list of the samples and their compositions is gathered in Table 4.

Table 4. Samples designs

Name	Nanoclay content ^a [wt%]	Feeding rate ^b [kg/h]	PEMA [wt%]	LDPE/LLDPE [wt%]	ALAMS type
1) OC1/1.5	1	1.5	2	97	OTAC
2) OC3/1	3	1	6	91	OTAC
3) OC3/2	3	2	6	91	OTAC
4) OC5/1.5	5	1.5	10	85	OTAC
5) DC1/1	1	1	2	97	DTAC
6) DC1/2	1	2	2	97	DTAC
7) DC3/1.5-1	3	1.5	6	91	DTAC
8) DC5/1	5	1	10	85	DTAC
9) DC3/1.5-2	3	1.5	6	91	DTAC
10) DC5/2	5	2	10	85	DTAC
11) DC3/1.5-3	3	1.5	6	91	DTAC
12) DB1/1.5	1	1.5	2	97	DTAB
13) DB3/1	3	1	6	91	DTAB
14) DB3/2	3	2	6	91	DTAB
15) DB5/1.5	5	1.5	10	85	DTAB
16) Reference	0	1.5	0	100	–

^ain the nanocomposite and the respective injected slurry

^bLDPE/LLDPE+PEMA+ALAMS, also identical to the rate of slurry injection.

2.3. Preparation of the samples using nanoclay slurry

Nanoclay slurry was prepared by dispersing Na⁺-MMT powder into distilled water using an overhead mechanical stirrer for 30, 60, and 90 minutes for 1, 3, and 5 wt% nanoclay contents, respectively. During the process, a magnetic stirrer was employed to prevent the slurry from being precipitated.

A lab-scale co-rotating intermeshing twin-screw extruder from Brabender DSE25 (Duisburg, Germany) was used to prepare samples. The screw diameter was 2.5 cm, its length/diameter was 32, and the distance between the two axes was 20.87 mm. Figure 1 shows the screw configuration and the order of mixing according to which the samples were prepared. LDPE/LLDPE uniform mixture with 60/40 ratio together with PEMA was added to the extruder through hopper using a granule feeder. ALAMS was first homogenously diluted in LDPE/LLDPE (60/40) powder and then added to the extruder through hopper using a powder feeder. The ratio of ALAMS to nanoclay equivalent was kept at 1.5:1. Because nanoclay content in the slurries and their respective samples were equal, the slurry injection rate was set equal to its respective feeding rate. The screw rotation speed was kept constant at 200 rpm. Temperature profile within the extruder for zones one to six was kept at 160, 170, 180, 185, 185, and 180°C, respectively. The residence times for the pure LDPE/LLDPE, measured by introducing black pel-

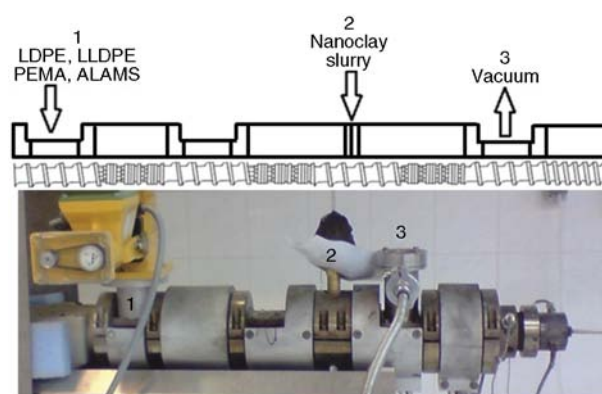


Figure 1. Schematic configuration of the screw and the order of mixing of the materials (top) the actual twin-screw extruder during sample preparation process (bottom)

lets into the extruder, are reported as the average time of initiation and termination of color change in the output. Residence time for each feeding rate was measured at least three times. Table 3 summarizes the average values of these results. The water was removed by vacuum in degassing section. The obtained strands were then pelletized.

2.4. Characterization

Tensile test measurements were performed on compression-molded sheets at room temperature using a tensile test machine (Z050, Zwick, Germany), based on ASTM-D638 [23], on dumbbell-shaped tensile bars of type I with a cross-head speed of 50 mm/min. At least three specimens of each sam-

ple were tested to establish testing reproducibility. For the sake of better response surface analysis, the average values of tensile modulus of the samples were normalized by the value of the reference, and the values are given for tensile-modulus increase in percent. The tensile modulus of the reference was $207 \pm 11.55 \text{ N/mm}^2$.

Nanoclay dispersion was investigated by X-ray diffraction (XRD) using a Holland Philips Xpert X-ray diffractometer with Co K α radiation ($\lambda = 1.789 \text{ \AA}$) generated at 40 kV and 30 mA, scanning from 1 to 12° at a step value of $0.02^\circ/\text{s}$ at room temperature. The compression-molded sheets at 190°C with 2 mm thickness were used for XRD studies.

The transmission electron microscopy (TEM) micrographs were obtained using a JEOL 2010F transmission electron microscope operating at an accelerating voltage of 120 kV. TEM samples for particle characterization were cryogenically cut into ultra thin sections (30–50 nm thick) with a diamond knife at a temperature of -40°C using a Reichert-Jung Ultra cut E microtome.

Oxygen permeability of the samples was measured using an apparatus illustrated in Figure 2. The oxygen pressure was set at 3 bars and the compression-molded films thickness was $350 \pm 30 \text{ }\mu\text{m}$. The oxygen purity was 99.99%. The rate of oxygen permeation was recorded during steady-state phase of the permeation process, according to $P = d \cdot (J/\Delta p)$, where J is the gas volumetric flow rate per unit area of the film, d is the thickness of the film, Δp is the pressure difference across the film, and P is permeability. To reduce error, the permeability of each

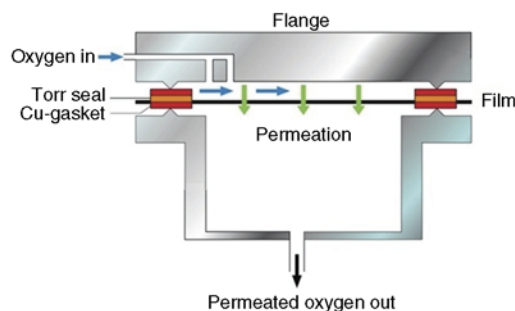


Figure 2. The schematic cross-section view of the apparatus used for oxygen permeability measurements

sample was then normalized by the permeability of the reference and reported as reduction in oxygen permeability in percent.

Nanoclay contents were measured by thermogravimetric analysis (TGA) under nitrogen at a flow rate of 20 mL/s using a Perkin Elmer Pyris-1 (USA) instrument. Measurements were conducted at 600°C with $10^\circ\text{C}/\text{min}$ heating rate.

3. Results

Mechanical and permeability measurements were performed to explore the effect of nanoparticles and their dispersion on the properties of the composites. Tensile-modulus increase, gas-permeability reduction, and d -spacing of nanoclay platelets in the samples are gathered in Table 5. It can be seen that the addition of nanoclay improved the tensile modulus and gas barrier properties of all the composites. The results also imply that the addition of water into the molten polymer had no damaging effect, i.e., hydrolysis, on the polymer.

Table 5. Physico-mechanical properties and nanoclay content of the samples

Specimen	Tensile-modulus increase [%]	Oxygen permeability reduction [%]	d -spacing [Å]	Nanoclay content [%]
OC1/1.5	33.9	18.3	80.0	0.76
OC3/1	84.2	31.8	40.2	2.91
OC3/2	42.4	22.5	33.5	2.79
OC5/1.5	93.4	41.0	18.8	4.57
DC1/1	22.2	10.9	13.9	0.80
DC1/2	12.3	7.7	13.9	0.78
DC3/1.5-1	31.2	15.4	13.1	2.75
DC5/1	47.4	24.4	12.1	4.73
DC3/1.5-2	35.9	16.0	13.2	2.67
DC5/2	41.5	17.2	12.0	4.57
DC3/1.5-3	32.0	17.1	13.2	2.81
DB1/1.5	13.9	7.4	13.9	0.78
DB3/1	17.1	12.9	13.0	2.62
DB3/2	15.3	9.1	13.0	2.56
DB5/1.5	22.0	13.6	12.0	4.52

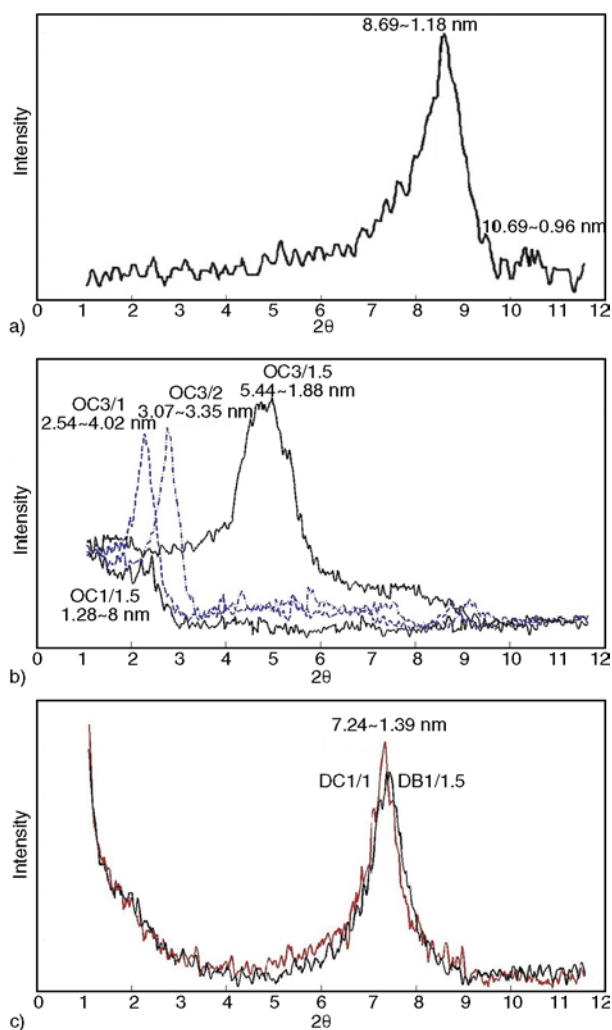


Figure 3. XRD patterns of Na⁺-MMT (a), samples prepared with OTAC (b), and DC1/1 and DB1/1.5 (c). The numbers indicate the angles and their corresponding *d*-spacing

Figure 3 shows XRD patterns of Na⁺-MMT (a), samples prepared with OTAC (b), and DC1/1 and DB1/1.5 (c). Na⁺-MMT has an intense diffraction peak at $2\theta = 8.69^\circ$ and a small peak at $2\theta = 10.69^\circ$ that correspond to basal spacing of 1.18 and 0.96 nm, respectively. This suggests that most of Na⁺-MMT were hydrated by one layer of water molecules between platelets. An increase in the *d*-spacing of nanoclay stacks results in 001 diffraction peak to shift to lower 2θ and to weaken in intensity.

To study the effect of ALAMS type on the dispersion of nanoparticles, mechanical, and gas barrier properties of the samples, surfaces of tensile-modulus increase, reduction in permeability, and *d*-spacing of nanoclay particles in the samples are plotted as a function of ALAMS type and feeding rate in Figure 4. As can be seen, OTAC produces the best

results, i.e., higher mechanical and permeability properties and also *d*-spacing. On the other hand, DTAC-modified samples demonstrate only slightly better results than DTAB-modified ones. An obvious interaction between ALAMS type and feeding rate can be observed in these graphs.

To better demonstrate the effect of feeding rate and nanoclay content on the dispersion of nanoparticles, mechanical, and gas barrier properties of the samples, surfaces of tensile-modulus increase, reduction in permeability, and *d*-spacing of nanoclay particles in the samples are plotted as a function of feeding rate and nanoclay content in Figure 5. As can be seen, nanoclay increase and feeding rate decrease cause both tensile modulus and reduction in permeability to rise. In a similar trend, feeding rate decrease causes the *d*-spacing of the nanoparticles to rise as well; nanoclay increase, however, causes the *d*-spacing of the nanoparticles to fall. Furthermore, no significant interaction between nanoclay content and feeding rate can be observed. To scrutinize the dispersion of nanoclay platelets, the compression-molded samples modified with OTAC were microtomed under liquid nitrogen, and the prepared thin sections were observed by TEM micrographs. The dark lines in Figure 6 are cross section of silicate layers, which show a homogeneous distribution of nanoclay platelets in the polymeric matrix. As can be seen, OC1/1.5 is largely exfoliated; whereas, other samples show some small stacks of nanoclay layers. Still, these samples show appropriate level of nanoclay dispersion, i.e., intercalated structure. All the samples show acceptable level of distribution and dispersion of silicate layers. The increase in nanoclay content and feeding rate causes the exfoliated structure to vanish and the intercalated structure to appear.

4. Discussion

4.1. The effect of ALAMS type

Mechanical and gas permeability properties of nanocomposites depend on many factors, including aspect ratio of nanoparticles, degree of nanoparticles dispersion in matrix, nanoparticles content, nanoparticles orientation, adhesion at nanoparticle-matrix interface, crystallinity etc. An increase in nanoclay content and improvement in its dispersion will enhance tensile modulus and reduce gas permeability.

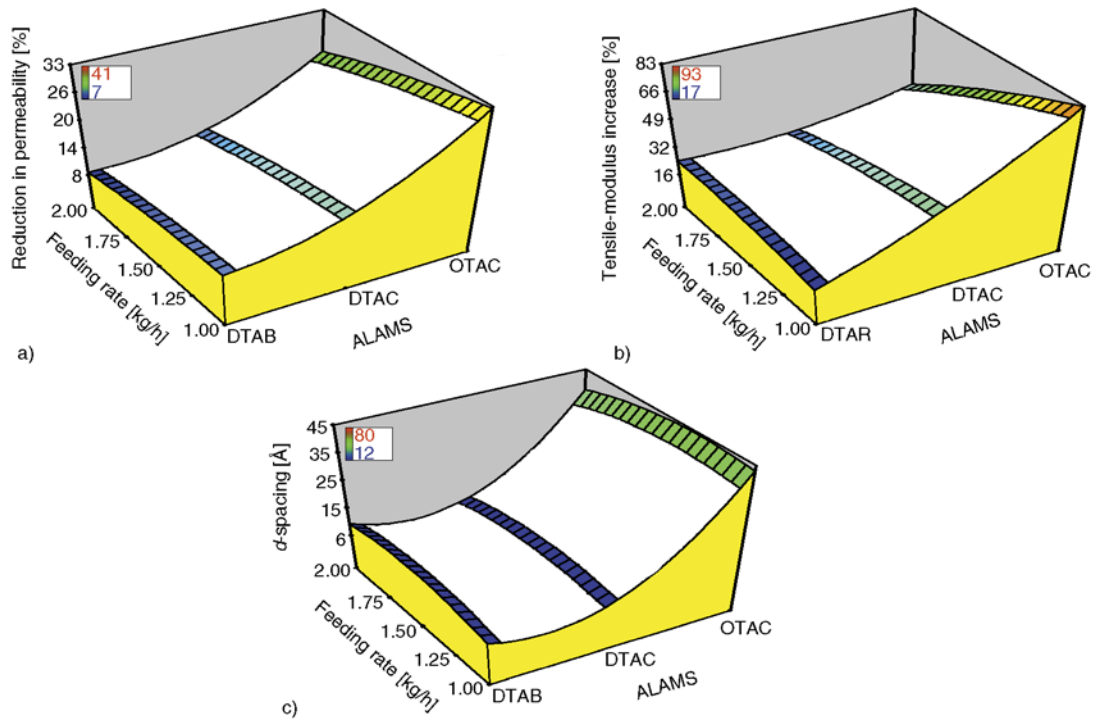


Figure 4. Response surfaces of (a) Reduction in permeability, (b) Tensile-modulus increase, (c) *d*-spacing for samples prepared with different ALAMS types as a function of feeding rate. The graphs are plotted for samples containing 3 wt% nanoclay and were altered manually for better clarification

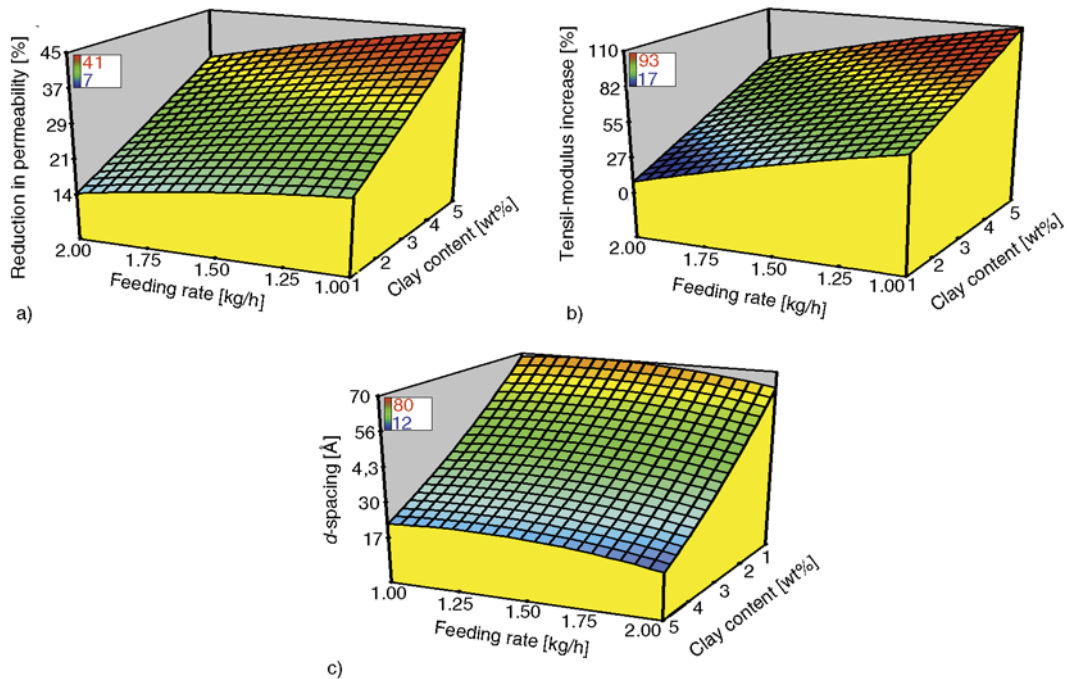


Figure 5. Response surfaces of (a) Reduction in permeability, (b) Tensile-modulus increase, (c) *d*-spacing as a function of feeding rate and clay content. The graphs are plotted for OTAC-modified samples. For clarification purposes, the graphs were altered manually and the axes of graph (c) are drawn in reverse order.

In Figure 4, a marked difference in *d*-spacing, mechanical, and permeability properties between OTAC-modified samples and samples modified with DTAC and DTAB can be observed. There are

few noticeable properties improvements in case of DTAC- and DTAB-modified samples. XRD results show that the *d*-spacings of nanoparticles in DTAC- and DTAB-modified samples are almost the same

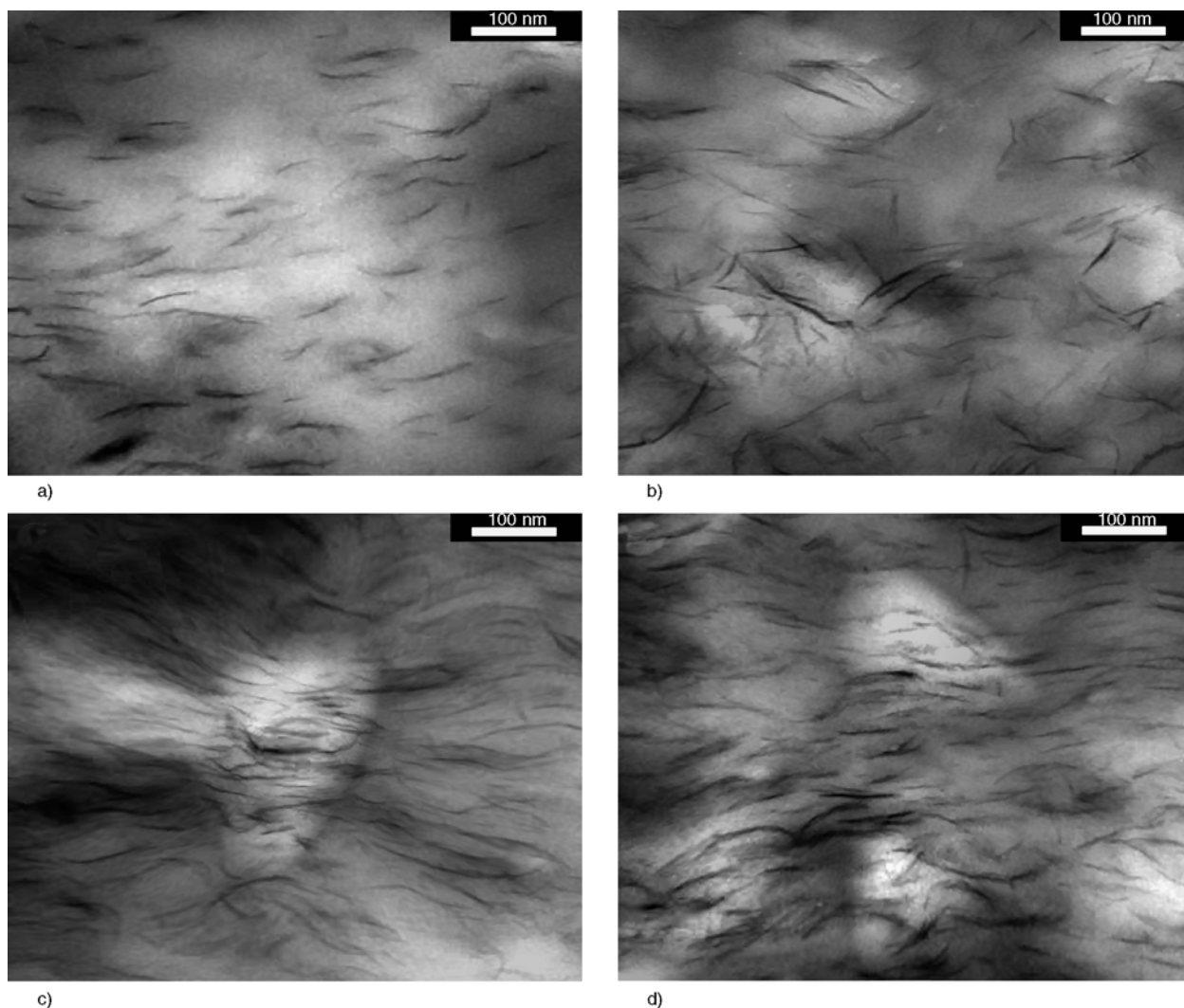


Figure 6. TEM micrographs of (a) OC1/1.5 (b) OC3/1, (c) OC3/2, (d) OC5/1.5

as that of pristine nanoclay, suggesting the samples to be close to microcomposites rather than nanocomposites. OTAC-modified samples, on the other hand, show a good rise in tensile modulus and perceptible improvement in gas barrier properties. The *d*-spacing increased as high as about 8nm, suggesting even the existence of exfoliated structure [24, 25] at low nanoclay contents, which is hard to achieve in case of polyolefins [26]. TEM micrographs also proved the existence of exfoliated structure for OC1/1.5 and intercalated structure for other OTAC-prepared samples. The similarity of the results for DTAC and DTAB suggests that the difference in halogen element, chlorine or bromine, barely changes the ALAMS ability to properly modify nanoclay platelets; on other hand, because chain length is the only difference between OTAC and DTAC, it can be concluded that chain length is the key factor.

Throughout this paper, we use the term ‘nanocomposite’ only to refer to OTAC-modified samples. Several factors can influence ALAMS ability to improve nanoclay dispersion, e.g., structure, density, number of alkyl tails, chain length, packing density, polymeric matrix etc. [27–29]. Very often, the effect of each of these factors may be influenced by other co-existing factors. For example, ALAMS with one alkyl tail was proved to produce better results in case of Nylon 6 [30]; whereas, ALAMS with two alkyl tails produced better results in case of PE [31]. Therefore, the effect of these factors on the dispersion of nanoparticles may vary depending on the specific material and processing conditions that are being investigated. Anyway, the effect of chain length on the interlayer spacing of nanoclay platelets has been the subject of several studies. In general, longer ALAMS chain length and higher

charge density of nanoclay is considered to result in further nanoclay interlayer spacing [32]. In a study on PE nanocomposites, Wang *et al.* [33] have found that the interlayer spacing increases with an increase in the size of ALAMS chain length; they also found that this parameter may change the degree of interaction between nanoclay and polyethylene. Balazs and coworkers [34, 35] have found that longer ALAMS chain length favors the layers separation by allowing the polymer to adopt more conformational degrees of freedom. According to Ginzburg *et al.* [36], for short ALAMS molecules, the polymer is unable to penetrate inside the gallery between nanoclay surfaces, and the equilibrium morphology becomes immiscible for most values of the Flory-Huggins parameter and nanoclay volume fraction. Only in case of large negative χ can such a composite become exfoliated.

The quality of nanoclay dispersion in a system is determined by the relationship between entropy and energy changes. During melt intercalation, the loss in entropy of polymer due to confinement in the gallery space can be reduced by an increase in interlayer spacing, which allows more conformational changes. The entropy change associated with the ALAMS length increases until nanoplatelets separation is equal to the fully extended length of the ALAMS chain [37]. Some of these studies, however, also suggested that there might be an optimum ALAMS chain length or nanoclay interlayer spacing, which results in optimum nanoclay dispersion. This notion has to be approached with care, since, as mentioned, specific polymer/nanoclay systems demonstrate specific characteristics; ergo, the value of this optimum spacing or the very existence of it may be dependent on the system that is being investigated. The interlayer distance also depends on the way the ALAMS chains organize themselves in the modified nanoclay [38]. One factor that directly affects ALAMS chain organization is ALAMS packing density inside nanoplatelets. This will be discussed in the next section.

4.2. The effect of feeding rate

As demonstrated by Figures 4–6, feeding rate increase had a detrimental effect on the dispersion of nanoclay particles in the samples. Considering the extruder as a plug reactor would suggest that the residence time is an important factor in this process.

Providing enough time for the OTAC to diffuse into water and react with nanoclay surface would ensure successful modification of nanoclay platelets, which leads to better stabilization of nanoclay platelets inside the matrix; thus, better dispersion can be achieved. This is the reason why samples prepared at higher feeding rates manifest lower d -spacing, gas barrier, and mechanical properties. Nonetheless, we should pay attention to the fact that lower feeding rate imposes lower shear stress on the materials inside the extruder. In conventional melt intercalation process, shear stress is vital for breaking down nanoclay agglomerates [39–41]. Interestingly, it seems that in this method the effect of shear stress is rather undermined. This finding shows that in water-assisted melt intercalation, the mechanism that affects the dispersion of nanoparticles is different from that of conventional melt intercalation. In other words, this process is diffusion-controlled rather than shear-controlled; this finding is in agreement with Hasegawa *et al.* [18] and Kato *et al.* [12] studies. We should, however, emphasize that one ought not to infer that higher shear stress does not have a positive effect on this process; but rather, shear stress effects, vis-à-vis residence time, are comparatively inconsequential. Moreover, the interaction between feeding rate and ALAMS type should be pointed out. The reason for this interaction to exist is that due to DTAC and DTAB inability to effectively modify nanoclay platelets, a change in feeding rate does not really affect the dispersion of nanoparticles in these samples; whereas, in case of OTAC-modified samples, feeding rate affects the dispersion through changing the residence time of materials inside the extruder. This is why an interaction between feeding rate and ALAMS type can be observed.

The effect of feeding rate on nanoclay dispersion can be further explained through ALAMS packing density inside nanoclay platelets; in this work, an increase in feeding rate decreased the average ALAMS packing density inside nanoplatelets. At low packing density, ALAMS chains have been considered to lie parallel to the silicate layer, in mono- or bi-layer formations, but, as packing density and/or chain length increases they are more likely to radiate away from nanoplatelets surface, organized in mono- or even a bi-molecular tilted ‘paraffinic’ formations. It is suggested that ALAMS

chains form liquid-like structures at low packing density or short ALAMS chain length. But, when the packing density and/or the chain length of ALAMS is within a certain range, the chains are not completely disordered but retain some orientational order similar to that in the liquid crystalline state; this increases the interlayer spacing of nanoclay particles [2].

Ginzburg *et al.* [36] showed that as ALAMS packing density increases, the miscibility between nanoclay platelets and polymer is improved and the resulting mixture can exhibit exfoliated structure for a range of nanoclay volume fractions. Similar conclusions have been drawn by Balazs and coworkers [34, 35] when they devised a theoretical model to study the effects of ALAMS packing density and chain length. Nonetheless, very high amounts of ALAMS packing density is suggested to make intercalation and exfoliation unfavorable, based on their model. This finding has been corroborated by Vaia and Giannelis [37] as well. They have also suggested that an optimal ALAMS packing density exists that favors optimum nanoclay dispersion.

4.3. The effect of nanoclay content

XRD results and TEM micrographs indicate that an increase in nanoclay content works to the detriment of nanoparticle dispersion. The decrease in the d -spacing of the nanoparticles at higher nanoclay content is a proof to this finding. TEM micrographs also show an increase in the existence of intercalated structure and disappearance of exfoliated structure as the nanoclay content increases. The reason for this finding is that at higher nanoclay contents, more OTAC must first diffuse into the slurry and then react with the nanoclay surface. This simply means more time is required for the cation exchange reaction to take place. Hence, at a given feeding rate, i.e., given residence time, an increase in nanoclay content decreases average ALAMS packing density inside nanoclay platelets. The other reason is the spatial hindrance imposed on nanoclay platelets by the surrounding nanoparticles. This hindrance is more profound at higher nanoclay contents and deteriorates the dispersion of the nanoparticles. Nevertheless, the effect of nanoclay content on gas barrier and mechanical properties of the samples is rather complicated. An increase in nanoclay content triggers two opposing trends: On the one

hand, nanoclay increase worsens its dispersion, which in turn works to the detriment of nanocomposite properties; on the other hand, the introduction of more rigid material, i.e., nanoclay, which has much higher modulus and almost zero gas permeability improves these properties. By taking a look at Figure 5a and 5b, it is obvious that the second trend is more dominant. In the end, it is interesting to mention that the increase in the tensile modulus and gas barrier properties of OTAC-modified nanocomposites prepared by slurry-fed melt intercalation are quite higher than those of the same nanocomposites prepared by conventional melt intercalation [42].

4.4. Permeability

Some would argue that the permeability properties of the OTAC-modified nanocomposites are poor and do not correspond to the expected values for a polymer nanocomposite. In response to this objection, it should be kept in mind that the films used in our barrier property measurements were compression-molded from which no noticeable nanoplatelets orientation can be achieved. Moreover, interfaces between different phases of nanocomposites, especially the polymers and the inorganic particles, could deteriorate the barrier properties by creating voids. Plus, adding nanoclay may alter polymer chains packing and increase free volume inside the matrix. Polymeric matrix polarity is also higher in case of composites. These reasons may lead to solubility enhancement in the matrix, which may work to the detriment of gas barrier properties of the composites. Lastly, our DSC results, not shown here, indicate that introducing nanoclay particles changes the crystallinity of the PE matrix. The effect of nanoclay on crystallinity behavior is complicated and requires to be addressed in another study. However, it is possible that this alteration in crystallinity may be in a way that causes the permeability to rise.

In this study, the permeability measurements were intended only to be used for comparative study of nanoclay dispersion in the samples; thus, the detailed study of permeability is not the focus of this paper. We, therefore, refuse to prove or disprove any of the mentioned probable causes because an all-inclusive elaboration on this subject will add considerable length to this paper. We, however, only demonstrate that how nanoparticles orientation

affects gas barrier properties by using model of Maksimov *et al.* [43]. This model, shown in Equation 1, is an empirical equation that relates the permeability of a composite with random nanoclay orientation to the permeability of a composite with nanoclay orientation perpendicular to the direction of diffusion. The relation has been stated as shown in Equation (1):

$$K_c = \frac{1}{3}[K_{\parallel} + 2K_m(1 - \phi)] \quad (1)$$

where K_c is the permeability of a composite with 3D random orientation, K_{\parallel} is the permeability of the composite when nanoplatelets are oriented normal to the direction of transversing gas. The second term on the right-hand side of the equation corresponds to the permeability of the composite when nanoplatelets are oriented parallel to the diffusion direction and it is assumed to be equal to the permeability of the matrix corrected for its volume fraction. After manipulation the equation can be written as shown in Equations (2–4):

$$\frac{K_{\parallel}}{K_m} = 3 \cdot \frac{K_c}{K_m} - 2(1 - \phi) \quad (2)$$

$$\phi = \frac{wt\%_f \cdot \rho_c}{100 \rho_f} \quad (3)$$

$$\frac{100}{\rho_c} = \frac{wt\%_f}{\rho_f} + \frac{wt\%_{LDPE}}{\rho_{LDPE}} + \frac{wt\%_{LLDPE}}{\rho_{LLDPE}} + \frac{wt\%_{PEMA}}{\rho_{PEMA}} \quad (4)$$

Here, ϕ is the volume fraction of nanoclay in the composites that can be calculated from Equation (3). The density of composite (ρ_c) can be calculated

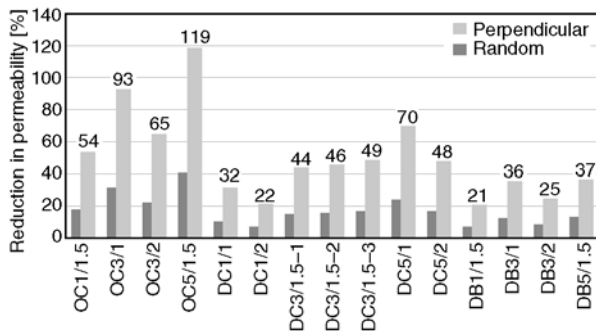


Figure 7. Estimated reduction in oxygen permeability for the hypothetical composites with nanoclay orientation perpendicular to diffusion direction (light color), compared to the results of the prepared samples (dark color)

from Equation (4), where ρ_f is nanoclay density, ρ_{LDPE} is LDPE density, ρ_{LLDPE} is LLDPE density, and ρ_{PEMA} is PEMA density. Based on Equation (2), gas permeability of composites with nanoplatelets normal to the diffusion direction can be estimated from composites with random orientation. This estimation offers an impression as to how nanoclay orientation affects gas barrier properties. The results are demonstrated in Figure 7; as can be seen, if our samples had nanoclay orientation completely normal to the diffusion direction, gas barrier property would be higher.

5. Mechanism

Figure 8 illustrates the schematic view of the four-step mechanism that we proposed to justify the role of water in the dispersion of nanoparticles during extrusion. Our proposed mechanism is as follow:

- (1) Nanoclay suspension is injected into the molten compound under high pressure. Molten compound consists of LDPE, LLDPE, PEMA, and OTAC.
- (2) During blending, nanoclay slurry would disperse in finer drops under shear field and OTAC would diffuse into the drops and would start a cation exchange reaction with the Na^+ cation, binding with silicate layers [12]; at the same time, water would begin to evaporate because of high compound temperature.
- (3) As water evaporates it also would get into finer drops and is dispersed more uniformly within the compound. The evaporated water is removed by vacuum [18].

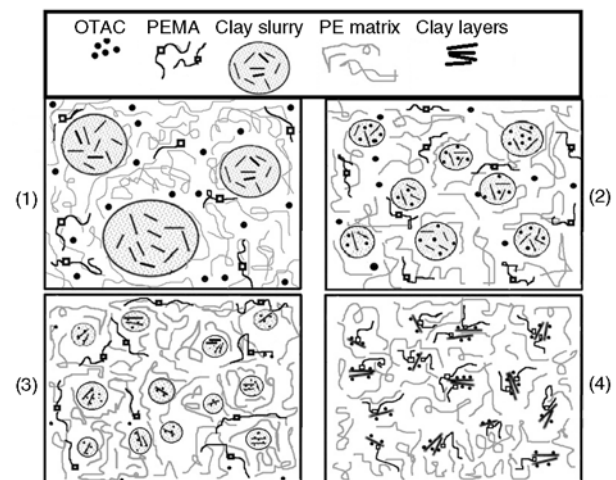


Figure 8. The schematic view of the four-step mechanism that illustrates the role of water in the dispersion of the nanoparticles

- (4) Finally, although water is completely evaporated, the silicate layers are stabilized by OTAC and are uniformly dispersed by PEMA. The layers are fixed and they maintain their formation, as proved by TEM micrographs.

In the end, it should be noted that LLDPE, due to being more elastic than LDPE, has greater segmental motion; as a result, LLDPE chains have to submit to larger entropy reduction to diffuse into nanoclay galleries. Plus, the amount of PEMA is not high in the matrix, compared to LDPE. Hence, nanoclay platelets must be largely intercalated by LDPE chains [42]. It is also probable that PEMA reacted with PE during the high temperature blending in air, forming a graft copolymer in which MA units are attached to the PE chains [44].

6. Conclusions

We prepared samples by injecting Na⁺-MMT slurry into a co-rotating twin-screw extruder, in a designed set of experiments based on response surface method. After investigating the effects of modifier type, feeding rate, and nanoclay content on the structural, mechanical, and permeability properties of the samples, we found out that (1) chain length and packing density of ALAMS modifiers were key factors in producing composites with better nanoclay dispersion and properties; (2) although high nanoclay content was proved to have a deleterious effect on nanoclay dispersion, it brought about an evident enhancement in mechanical and gas barrier properties for OTAC-modified nanocomposites: 93 and 41% enhancement in tensile modulus and oxygen permeability reduction were recorded, respectively; (3) an increase in residence time was more effective in producing better nanocomposites than an increase in shear stress.

Additionally, the existence of intercalated/exfoliated structures in the nanocomposites was proved by XRD and TEM. Interestingly, the improvement in the properties of the nanocomposites prepared in this work was higher than those of prepared with conventional method. Our study indicates that, contrary to conventional melt intercalation, water-assisted melt intercalation process is largely diffusion-controlled rather than shear-controlled. For this reason, a new mechanism was proposed to justify this finding and also to describe the role of water in the dispersion of nanoparticles.

Acknowledgements

The authors would like to express their gratitude to Dr. M. Ahmadi for his help on the TEM. S.I.S. Shahabadi would also like to thank Mr. Y. Kheyrikhah, Mr. M. Fayyazi, Mr. M. Javid Mehr, and Mr. O. Shojaee for their invaluable technical assistance during sample production. Partial financial support from the Iranian Nanotechnology Initiative is also gratefully appreciated.

References

- [1] Chrissopoulou K., Altintzi I., Anastasiadis S. H., Giannelis E. P., Pitsikalis M., Hadjichristidis N., Theophilou N.: Controlling the miscibility of polyethylene/layered silicate nanocomposites by altering the polymer/surface interactions. *Polymer*, **46**, 12440–12451 (2005). DOI: [10.1016/j.polymer.2005.10.106](https://doi.org/10.1016/j.polymer.2005.10.106)
- [2] Alexandre M., Dubois P.: Polymer-layered silicate nanocomposites: Preparation, properties and uses of a new class of materials. *Materials Science and Engineering R: Reports*, **28**, 1–63 (2000). DOI: [10.1016/S0927-796X\(00\)00012-7](https://doi.org/10.1016/S0927-796X(00)00012-7)
- [3] Paul D. R., Robeson L. M.: Polymer nanotechnology: Nanocomposites. *Polymer*, **49**, 3187–3204 (2008). DOI: [10.1016/j.polymer.2008.04.017](https://doi.org/10.1016/j.polymer.2008.04.017)
- [4] Giannelis E. P.: Polymer layered silicate nanocomposites. *Advanced Materials*, **8**, 29–35 (1996). DOI: [10.1002/adma.19960080104](https://doi.org/10.1002/adma.19960080104)
- [5] Ishida H., Campbell S., Blackwell J.: General approach to nanocomposite preparation. *Chemistry of Materials*, **12**, 1260–1267 (2000). DOI: [10.1021/cm990479y](https://doi.org/10.1021/cm990479y)
- [6] Kiliaris P., Papaspyrides C. D.: Polymer/layered silicate (clay) nanocomposites: An overview of flame retardancy. *Progress in Polymer Science*, **35**, 902–958 (2010). DOI: [10.1016/j.progpolymsci.2010.03.001](https://doi.org/10.1016/j.progpolymsci.2010.03.001)
- [7] Zhao C., Qin H., Gong F., Feng M., Zhang S., Yang M.: Mechanical, thermal and flammability properties of polyethylene/clay nanocomposites. *Polymer Degradation and Stability*, **87**, 183–189 (2005). DOI: [10.1016/j.polymdegradstab.2004.08.005](https://doi.org/10.1016/j.polymdegradstab.2004.08.005)
- [8] Ray S. S., Okamoto M.: Polymer/layered silicate nanocomposites: A review from preparation to processing. *Progress in Polymer Science*, **28**, 1539–1641 (2003). DOI: [10.1016/j.progpolymsci.2003.08.002](https://doi.org/10.1016/j.progpolymsci.2003.08.002)
- [9] Korbee R. A., Van Geenen A. A.: Process for the preparation of a polyamide nanocomposite composition. U.S. Patent 6350805, USA (1999).
- [10] Karger-Kocsis J.: Water-mediated dispersion of ‘nanofillers’ in thermoplastics: Is it the right way? *Express Polymer Letters*, **2**, 312 (2008). DOI: [10.3144/expresspolymlett.2008.37](https://doi.org/10.3144/expresspolymlett.2008.37)
- [11] Molajavadi V., Garmabi H.: Water assisted exfoliation of PA6/clay nanocomposites using a twin screw extruder: Effect of water contact time. *Journal of Applied Polymer Science*, **119**, 736–743 (2011). DOI: [10.1002/app.32766](https://doi.org/10.1002/app.32766)

- [12] Kato M., Matsushita M., Fukumori K.: Development of a new production method for a polypropylene-clay nanocomposite. *Polymer Engineering and Science*, **44**, 1205–1211 (2004).
DOI: [10.1002/pen.20115](https://doi.org/10.1002/pen.20115)
- [13] Sarikhani K., Abdollahi S., Garmabi H.: Preparation of PE nanocomposites using pristine nano clay via alkyl ammonium solution injection in a twin-screw extruder. *Journal of Applied Polymer Science*, **124**, 1344–1351 (2010).
DOI: [10.1002/app.35124](https://doi.org/10.1002/app.35124)
- [14] Fedullo N., Sclavons M., Bailly C., Lefebvre J.-M., Devaux J.: Nanocomposites from untreated clay: A myth? *Macromolecular Symposia*, **233**, 235–245 (2006).
DOI: [10.1002/masy.200690023](https://doi.org/10.1002/masy.200690023)
- [15] Yu Z.-Z., Hu G.-H., Varlet J., Dasari A., Mai Y.-W.: Water-assisted melt compounding of nylon-6/pristine montmorillonite nanocomposites. *Journal of Polymer Science Part B: Polymer Physics*, **43**, 1100–1112 (2005).
DOI: [10.1002/polb.20397](https://doi.org/10.1002/polb.20397)
- [16] Touchaleaume F., Soulestin J., Sclavons M., Devaux J., Cordenier F., Van Velthem P., Flat J. J., Lacrampe M. F., Krawczak P.: Efficient one-step melt-compounding of copolyetheramide/pristine clay nanocomposites using water-injection as intercalating/exfoliating aid. *Express Polymer Letters*, **5**, 1085–1101 (2011).
DOI: [10.3144/expresspolymlett.2011.106](https://doi.org/10.3144/expresspolymlett.2011.106)
- [17] Siengchin S., Karger-Kocsis J., Thomann R.: Nano-filled and/or toughened POM composites produced by water-mediated melt compounding: Structure and mechanical properties. *Express Polymer Letters*, **2**, 746–756 (2008).
DOI: [10.3144/expresspolymlett.2008.88](https://doi.org/10.3144/expresspolymlett.2008.88)
- [18] Hasegawa N., Okamoto H., Kato M., Usuki A., Sato N.: Nylon 6/Na–montmorillonite nanocomposites prepared by compounding Nylon 6 with Na–montmorillonite slurry. *Polymer*, **44**, 2933–2937 (2003).
DOI: [10.1016/S0032-3861\(03\)00215-5](https://doi.org/10.1016/S0032-3861(03)00215-5)
- [19] Box G. E. P., Behnken D. W.: Some new three level designs for the study of variables. *Technometric*, **2**, 455–475 (1960).
- [20] Box G. E. P., Draper N. R.: *Empirical model-building and response surface*. Wiley, New York (1987).
- [21] Khuri A. J., Cornell I. A.: *Response surface: Designs and analyses*. Marcel Dekker, New York (1987).
- [22] Montgomery D. C.: *Design and analysis of experiments*. Wiley, New York (1991).
- [23] ASTM D638: Standard test method for tensile properties of plastics. American society for testing and materials. Annual book of ASTM standard (1990).
- [24] Chin I.-J., Thurn-Albrecht T., Kim H.-C., Russell T. P., Wang J.: On exfoliation of montmorillonite in epoxy. *Polymer*, **42**, 5947–5952 (2001).
DOI: [10.1016/S0032-3861\(00\)00898-3](https://doi.org/10.1016/S0032-3861(00)00898-3)
- [25] Kim G.-M., Lee D.-H., Hoffmann B., Kressler J., Stöpelmann G.: Influence of nanofillers on the deformation process in layered silicate/polyamide-12 nanocomposites. *Polymer*, **42**, 1095–1100 (2001).
DOI: [10.1016/S0032-3861\(00\)00468-7](https://doi.org/10.1016/S0032-3861(00)00468-7)
- [26] García-López D., Picazo O., Merino J. C., Pastor J. M.: Polypropylene–clay nanocomposites: Effect of compatibilizing agents on clay dispersion. *European Polymer Journal*, **39**, 945–950 (2003).
DOI: [10.1016/S0014-3057\(02\)00333-6](https://doi.org/10.1016/S0014-3057(02)00333-6)
- [27] Duquesne S., Jama C., Le Bras M., Delobel R., Recourt P., Gloaguen J. M.: Elaboration of EVA-nano-clay systems – Characterization, thermal behavior, and fire performance. *Composites Science and Technology*, **63**, 1141–1148 (2003).
DOI: [10.1016/S0266-3538\(03\)00035-6](https://doi.org/10.1016/S0266-3538(03)00035-6)
- [28] Zhang W., Chen D., Zhao Q., Fang Y.: Effects of different kinds of clay and different vinyl acetate content on the morphology and properties of EVA/clay nanocomposites. *Polymer*, **44**, 7953–7961 (2003).
DOI: [10.1016/j.polymer.2003.10.046](https://doi.org/10.1016/j.polymer.2003.10.046)
- [29] Peeterbroeck S., Alexandre M., Jérôme R., Dubois P.: Poly(ethylene-co-vinyl acetate)/clay nanocomposites: Effect of clay nature and organic modifiers on morphology, mechanical and thermal properties. *Polymer Degradation and Stability*, **90**, 288–294 (2005).
DOI: [10.1016/j.polymdegradstab.2005.03.023](https://doi.org/10.1016/j.polymdegradstab.2005.03.023)
- [30] Fornes T. D., Yoon P. J., Hunter D. L., Keskkula H., Paul D. R.: Effect of organoclay structure on nylon 6 nanocomposite morphology and properties. *Polymer*, **43**, 5915–5933 (2002).
DOI: [10.1016/S0032-3861\(02\)00400-7](https://doi.org/10.1016/S0032-3861(02)00400-7)
- [31] Hotta S., Paul D. R.: Nanocomposites formed from linear low density polyethylene and organoclays. *Polymer*, **45**, 7639–7654 (2004).
DOI: [10.1016/j.polymer.2004.08.059](https://doi.org/10.1016/j.polymer.2004.08.059)
- [32] LeBaron P. C., Wang Z., Pinnavaia T. J.: Polymer-layered silicate nanocomposites: An overview. *Applied Clay Science*, **15**, 11–29 (1999).
DOI: [10.1016/S0169-1317\(99\)00017-4](https://doi.org/10.1016/S0169-1317(99)00017-4)
- [33] Wang K. H., Choi M. H., Koo C. M., Choi Y. M., Chung I. J.: Synthesis and characterization of maleated polyethylene/clay nanocomposites. *Polymer*, **42**, 9819–9826 (2001).
DOI: [10.1016/S0032-3861\(01\)00509-2](https://doi.org/10.1016/S0032-3861(01)00509-2)
- [34] Balazs A. C., Singh C., Zhulina E.: Modeling the interactions between polymers and clay surfaces through self-consistent field theory. *Macromolecules*, **31**, 8370–8381 (1998).
DOI: [10.1021/ma980727w](https://doi.org/10.1021/ma980727w)
- [35] Zhulina E., Singh C., Balazs A. C.: Attraction between surfaces in a polymer melt containing telechelic chains: Guidelines for controlling the surface separation in intercalated polymer–clay composites. *Langmuir*, **15**, 3935–3943 (1999).
DOI: [10.1021/la981406g](https://doi.org/10.1021/la981406g)

- [36] Ginzburg V. V., Singh C., Balazs A. C.: Theoretical phase diagrams of polymer/clay composites: The role of grafted organic modifiers. *Macromolecules*, **33**, 1089–1099 (2000).
DOI: [10.1021/ma991324e](https://doi.org/10.1021/ma991324e)
- [37] Vaia R. A., Giannelis E. P.: Lattice model of polymer melt intercalation in organically modified layered silicates: Model predictions and experiment. *Macromolecules*, **30**, 7990–7999 (1997).
DOI: [10.1021/ma9514333](https://doi.org/10.1021/ma9514333)
- [38] Zanetti M., Lomakin S., Camino G.: Polymer layered silicate nanocomposites. *Macromolecular Materials and Engineering*, **279**, 1–9 (2000).
DOI: [10.1002/1439-2054\(20000601\)279:1<1::AID-MAME1>3.0.CO;2-Q](https://doi.org/10.1002/1439-2054(20000601)279:1<1::AID-MAME1>3.0.CO;2-Q)
- [39] Dennis H. R., Hunter D. L., Chang D., Kim S., White J. L., Cho J. W., Paul D. R.: Effect of melt processing conditions on the extent of exfoliation in organoclay-based nanocomposites. *Polymer*, **42**, 9513–9522 (2001).
DOI: [10.1016/S0032-3861\(01\)00473-6](https://doi.org/10.1016/S0032-3861(01)00473-6)
- [40] Fornes T. D., Yoon P. J., Keskkula H., Paul D. R.: Nylon 6 nanocomposites: The effect of matrix molecular weight. *Polymer*, **42**, 9929–9940 (2001).
DOI: [10.1016/S0032-3861\(01\)00552-3](https://doi.org/10.1016/S0032-3861(01)00552-3)
- [41] Hejazi I., Sharif F., Garmabi H.: Effect of material and processing parameters on mechanical properties of polypropylene/ethylene–propylene–diene–monomer/clay nanocomposites. *Materials and Design*, **32**, 3803–3809 (2011).
DOI: [10.1016/j.matdes.2011.03.017](https://doi.org/10.1016/j.matdes.2011.03.017)
- [42] Hemati F., Garmabi H.: Compatibilised LDPE/LLDPE/nanoclay nanocomposites: I. Structural, mechanical, and thermal properties. *The Canadian Journal of Chemical Engineering*, **89**, 187–196 (2010).
DOI: [10.1002/cjce.20377](https://doi.org/10.1002/cjce.20377)
- [43] Maksimov R. D., Gaidukov S., Zicans J., Jansons J.: Moisture permeability of a polymer nanocomposite containing unmodified clay. *Mechanics of Composite Materials*, **44**, 505–514 (2008).
DOI: [10.1007/s11029-008-9041-x](https://doi.org/10.1007/s11029-008-9041-x)
- [44] Zhang J., Wilkie C. A.: Preparation and flammability properties of polyethylene–clay nanocomposites. *Polymer Degradation and Stability*, **80**, 163–169 (2003).
DOI: [10.1016/S0141-3910\(02\)00398-1](https://doi.org/10.1016/S0141-3910(02)00398-1)

Rheological and thermal analysis of the filling stage of injection moulding

A. Szűcs*, K. Belina

Department of Polymer and Rubber Technology, Faculty of Mechanical Engineering and Automation, Kecskemét College, Izsáki út 10., H-6000 Kecskemét, Hungary

Received 14 October 2011; accepted in revised form 7 March 2012

Abstract. Flow conditions are different in the cavity of the injection mould from the capillary flow of a laboratory rheological instrument. An injection moulding slit die rheometer (Rheo-mould) was designed with a series of slit and orifice dies. Four pressure sensors were built in the stationary side of the mould, therefore the pressure could be measured at four different places. A changeable slit die insert was designed in the moving side. The shear stress and the shear rate can be calculated from the pressure gradient and from the flow rate of the melt, respectively. Flow curves of low density polyethylene were determined using Bagley, Rabinowitsch and Mooney corrections. The results were compared to the flow curves determined by Göttfert and Haake capillary equipments. It was found that the agreement between the methods is excellent.

Keywords: rheology, injection moulding, cavity pressure, mould filling

1. Introduction

Determination of rheological properties of molten polymers is a considerably studied field of Polymer Physics. Knowledge of real viscosity of polymer melt in the injection moulding process is extremely important. The flow of polymers is a complex process, as the viscosity of plastics, apart from temperature and pressure, depends on the molecular mass, molecular mass distribution and on the deformation rate. These make plastic processing rather difficult. During the flow in nozzle, runner system and in thin walled cavities of injection moulds, both shear and elongation deformation processes are developed, and the deformation rates are generally high. Many laboratory instruments can be found on the market but only a few of them are suitable for measuring the flow properties of polymeric material in the processing environment. On-line extrusion viscometers are wide-spread instruments, but injection

moulding machines are hardly used for rheological tests [1–6].

One of the main goals of our research is to develop a special injection mould which is suitable to determine the rheological properties of polymers at a high deformation rate. In the first stage of the research, two pressure sensors were built into a standard injection mould. Basic measurements and calculations were carried out by it. Then a spiral injection mould was designed, and after some success, it was upgraded to a changeable slit die system. In the final set-up, most of the important parameters can be controlled [7, 8].

The importance of the results is to get reliable data for the simulation of the injection moulding process. Reliability of filling simulations depends mainly on the following four factors [7]: input data, process parameters, software applications and numerical models. In particular, among the processing param-

*Corresponding author, e-mail: szucs.andras@gamf.kefo.hu
© BME-PT

eters, the rheological characteristics of polymer melts have the largest influence on the filling simulation.

2. Theoretical background and calculations

There are two approaches to describe flow behaviour of a rheologically complex fluid: continuum mechanics and molecular approach. The molecular approach is rather complex, as molecular structure and molecular motions are considered to describe the relationships. Considering the material as a continuum, stress-strain relationships can be calculated by mathematical equations based on the theories of continuum mechanics. In principle, there are six independent components of stress that must be specified to completely describe the state of stress. However, in simple steady shear flow, fewer number of stress components is necessary. For example, stress components in a cube are shown in Figure 1, and the corresponding stress and deformation rate tensors are shown in Equation (1) and Equation (2), respectively:

$$\tau = \begin{bmatrix} \tau_{zz} & \tau_{zy} & 0 \\ \tau_{yz} & \tau_{yy} & 0 \\ 0 & 0 & \tau_{xx} \end{bmatrix} \tag{1}$$

$$\dot{\gamma} = \begin{bmatrix} 0 & \dot{\gamma} & 0 \\ \dot{\gamma}_{yz} & 0 & 0 \\ 0 & 0 & 0 \end{bmatrix} \tag{2}$$

where τ is the shear stress tensor, $\dot{\gamma}$ is the shear rate tensor, x, y and z shows the directions. τ_{zz} means the shear stress acting on the surface perpendicular to the z axis and showing in z direction.

Different kinds of measuring systems can be used for rheological measurements. Mostly simple shear flow is carried out in capillary or in slit die. In steady shear flow there are no more than three independent material functions needed for correlating the stress quantities of rheological significance to the shear

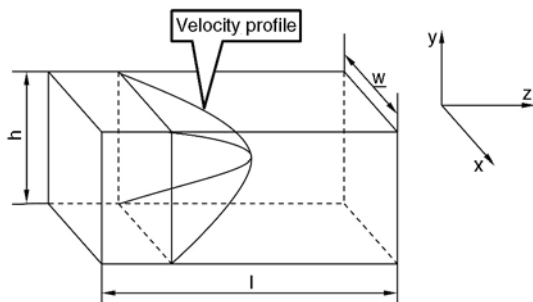


Figure 1. Shear flow in a slit die. (w : width of the die; h : height of the die, l : flow length)

rate. These viscosity functions are given by Equations (3–5):

$$\tau_{12} = \tau(\dot{\gamma}), \quad \eta(\dot{\gamma}) = \frac{\tau(\dot{\gamma})}{\dot{\gamma}} \tag{3}$$

$$\tau_{11} - \tau_{22} = N_1(\dot{\gamma}), \quad \xi_{12}(\dot{\gamma}) = \frac{N_1(\dot{\gamma})}{\dot{\gamma}^2} \tag{4}$$

$$\tau_{22} - \tau_{33} = N_2(\dot{\gamma}), \quad \xi_{23}(\dot{\gamma}) = \frac{N_2(\dot{\gamma})}{\dot{\gamma}^2} \tag{5}$$

in which $\eta(\dot{\gamma})$, N_1 and N_2 are called material functions. $\eta(\dot{\gamma})$ defines the shear dependent viscosity, ξ_{12} defines the first normal stress function, ξ_{23} defines the second normal stress function [9].

In the measurements by capillary rheometers, the flow rate (shear rate) is controlled and the pressure drop (shear stress) is measured. The apparent values can be calculated from the primary data, but some corrections must be made for the determination of real functions.

In the calculations, apparent values are used. The apparent shear rate, shear stress and viscosity can be calculated if slit die is used by Equations (6–8):

$$\dot{\gamma}_{app} = \frac{6Q}{h^2w} \tag{6}$$

$$\tau_{app} = \frac{h\Delta p}{2l} \tag{7}$$

$$\eta_{app} = \frac{\tau_{app}}{\dot{\gamma}_{app}} \tag{8}$$

where Q is the volumetric flow rate, h is the height of the die, w is the width of the die, l is the flow length, Δp is the pressure drop, τ is the shear stress, $\dot{\gamma}$ is the shear rate.

In order to obtain accurate experimental results, the height-to-width ratio (h/w) of the slit die should be near to zero ($w \gg h$), because the existing theoretical equations converting Q and $\Delta p/l$ to shear rate and shear stress, respectively, are based on the assumption that the velocity does not depend on lateral position. Approaching w/h ratio to zero, the edges make negligible contribution to the pressure drop. In this case the corrected shear rate and shear stress are calculated by Equations (9–11) [10]:

$$\tau_w = \frac{\Delta p h}{2l} \left(\frac{1}{\frac{h}{w} + 1} \right) \tag{9}$$

where h is the height and w is the width of the die. Δp is the pressure drop, l is the measured flow length (Equation (10)):

$$\dot{\gamma} = \frac{2}{3} \left(\frac{6Q}{h^2} \right) \left(\frac{b}{f} + \frac{a}{f n} \right) \quad (10)$$

where Q is volume rate, a, b, f are correction factors, n is the power law index (Equation (11)):

$$n = \frac{d \log \tau_f}{d \log \dot{\gamma}_f} \quad (11)$$

Some material might slip on the wall of the die. Figure 2 shows the velocity profile of the melt if it slips. Using different slit die cross sections but same flow length, the velocity of the wall slip can be determined [11].

The total volumetric flow rate (Q_T) can be calculated by Equation (12):

$$Q_T = \frac{h^3 w}{6} \dot{\gamma} \quad (12)$$

The volumetric flow rate by the slip (Q_{slip}) is given by the Equation (13):

$$Q_{\text{slip}} = whv_{\text{slip}} \quad (13)$$

where v_{slip} is the velocity of wall slip.

The apparent shear rate can be plotted as function of $1/h$ and the wall slip velocity can be calculated from the slope of the curve described in Equation (14):

$$\dot{\gamma}_{\text{app}} = \dot{\gamma}_{\text{true}} + \frac{6v_{\text{slip}}}{h} \quad (14)$$

According to Equation (7), the pressure gradient is a linear function of flow length. If it is not valid, Bagley correction should be applied.

The viscosity of molten polymer is really high, basically it is between 10...10.000 Pa·s in injection moulding or extrusion process. Due to the high viscosity, the dissipation heat and the effect of pressure

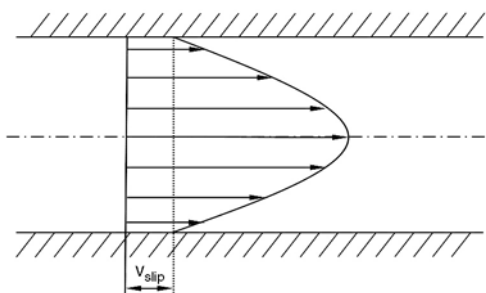


Figure 2. Velocity profile of the melt

are not negligible. The average temperature rising (ΔT) can be calculated by Equation (15):

$$\Delta T = \frac{\Delta p}{\rho c_p} \quad (15)$$

where Δp is the pressure drop, ρ is the density, c_p is the specific heat of the material. Equation (15) assumes that there is no heat exchange between the material and the mould (wall of the die). In real cases there is some heat transfer between the mould and the polymer melt. This transfer depends on the temperature difference, therefore changing the mould temperature it is possible to influence the heat exchange rate. Dimensionless numbers (Graetz-, Nahme- Brinkman-number) are used to characterise the thermal conditions of the flow of polymer melt. Graetz-number (Gz , Equation (16)) [12] compares the heat transfer in the flow direction to the perpendicular direction:

$$Gz = \frac{2\rho c_p Q h}{\lambda w l} \quad (16)$$

where ρ is the density of the material, c_p the specific heat capacity, λ is coefficient of thermal conduction. If $Gz \gg 1$, the material temperature in the calculation and the incoming material temperature are the same [13].

Nahme-number (Na , Equation (17)) compares the temperature rising by dissipation heat to the temperature influence to the viscosity:

$$Na = \frac{\eta Q^2 \alpha_\eta}{4kh^2 w^2} \quad (17)$$

where α_η is temperature coefficient of viscosity.

If $Na > 1$, the dissipation heat has significant effect on the viscosity.

Brinkman-number (Br , Equation (18)) compares the dissipation heat to the perpendicular heat transfer:

$$Br = \frac{\eta Q^2}{4kh^2 w^2 |T_{\text{in}} - T_{\text{wall}}|} \quad (18)$$

where T_{in} is the incoming material temperature, T_{wall} is the temperature of the wall of the cavity.

If $Br > 1$, the dissipation is the major process, therefore the temperature drop of the material is negligible. If the mould temperature and the material temperature are the same, the Brinkman-number is infinite.

According to Laun studies [13–14], the real pressure drop (allowing for the dissipation heat and the effect of the pressure) can be calculated by Equation (19):

$$\Delta p \approx \Delta p_0 \exp(\beta_\eta p_1) \left[1 - (\beta_\eta + \alpha_\eta \varepsilon_p) \frac{\Delta p_0}{2} \exp(\beta_\eta p_1) \right] \quad (19)$$

where Δp_0 stands for the pressure loss without pressure and temperature effects, β_η pressure coefficient of viscosity α_η temperature coefficient of viscosity, Δp is the measurable pressure difference ($\Delta p = p_1 - p_2$).

$$\varepsilon_p = \frac{1}{\rho_0 \left(c_p + \frac{\Lambda}{\dot{m}} \right)} \quad (20)$$

Equation (20) represents a dissipative heating coefficient (ε_p) (Λ lump heat transfer coefficient summarising all types of heat loss out of the melt). The adiabatic case (insulated walls) is got by setting $\Lambda = 0$, \dot{m} represents the mass flow rate, ρ_0 is the melt density [13].

3. Experimental

3.1. Materials

TIPOLEN FA2210 (Tisza Chemical Group PLC, Tiszaújváros, Hungary) low-density polyethylene material was used for the measurements. This material is recommended for blow moulding technology, so the viscosity of the material can be measured easily during shear and the deformation caused by elongation. The characteristics of the PE are summarised in Table 1.

Table 1. Main properties of the material

Properties	Value
MFI (190°C; 2,16 kg)	0.3 g/10 min
Density (23°C)	0.922 g/cm ³
Maximum viscosity (190°C)	90 000 Pa·s
Apparent activation energy of flow	31.5 kJ/mol

3.2. Measuring system

An ARBURG Allrounder 270 C 350-70 standard injection moulding machine was used in the experiment. The most important machine parameters are listed in Table 2.

There are some instrumented injection moulds [1–5] but the one developed by us is basically different

Table 2. The most important machine parameters

Parameters	Value
Injection rate (Q)	5...90 cm ³
Injection pressure ($p_{injection}$)	1500 bar
Material temperature (T_{mat})	180...220°C
Mould temperature (T_{mould})	30...220°C
Screw rotation speed (n)	150 mm/s
Back pressure (p_{back})	20 bar
Switch-over point (s_{switch})	1 cm ³
Packing time (t_{pack})	0 s

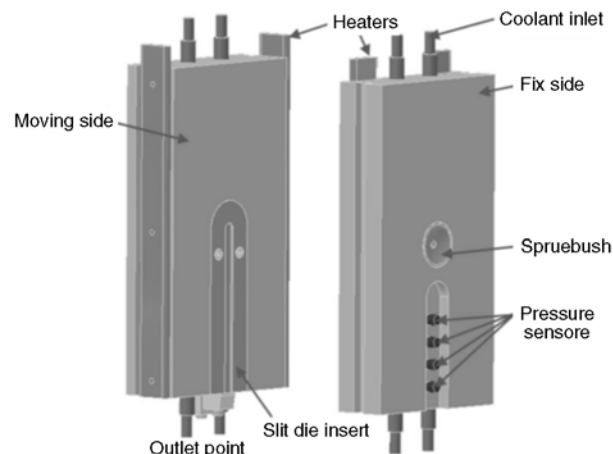


Figure 3. Active plates and the accessories of the system

from them. The material enters in the centreline of the mould from the sprue bush and goes to the parting line. There is a quick-change slit die system in the moving side. The material flow through the die and came out at the end of it. Three pressure sensors (Kistler 6157BD) and one P-T combo sensor (Kistler 6190A) were built into the fixed side. The mould temperature was controlled by cooling fluid to 90°C, and an electric heating system was used above 90°C. The drawing of the mould can be seen in Figure 3.

Figure 4 shows the positions of the sensors. The dimensions of the dies used in the experiments are listed in the Table 3. The width of the dies was the same, 15 mm.

A virtual instrument was developed by LabView software environment for data processing. It can control the database and calculate the rheological properties from the measured pressure in Windows XP environment. The applied sampling rate was 0.001 sec in the measurements. This relatively high sampling rate is necessary to study the melt fracture effect. The schematic drawing of the electronic system is shown in Figure 5.

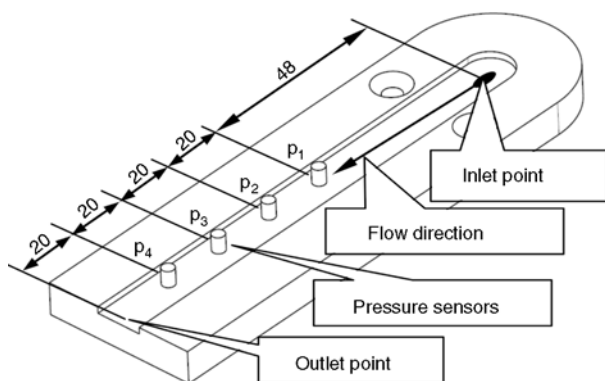


Figure 4. Slit die insert

Table 3. Geometry of the dies

No. of slit die	1.	2.	3.	4.	5.	6.
Height (<i>h</i>) [mm]	2	3	4	2	2	2
Flow length (<i>l</i>) [mm]	80	80	80	45	65	80
Width (<i>w</i>) [mm]	15	15	15	15	15	15

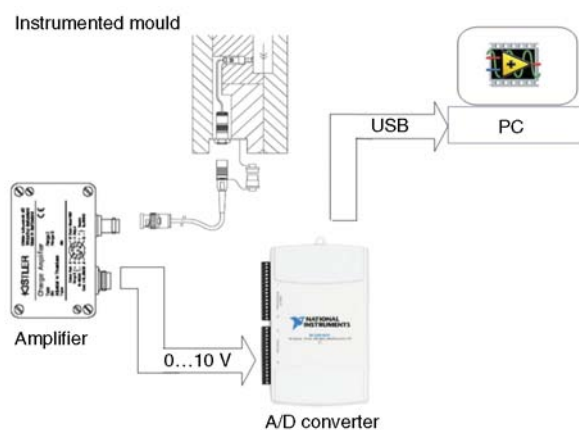


Figure 5. Signal transducer system

The measured four pressure curves and the pressure differences are plotted as a function of time in Figure 6. It can be seen that the cavity filling has two different phases. The material flows inside of the cavity in the first stage. The pressures increase continuously until the melt front reaches the outlet point.

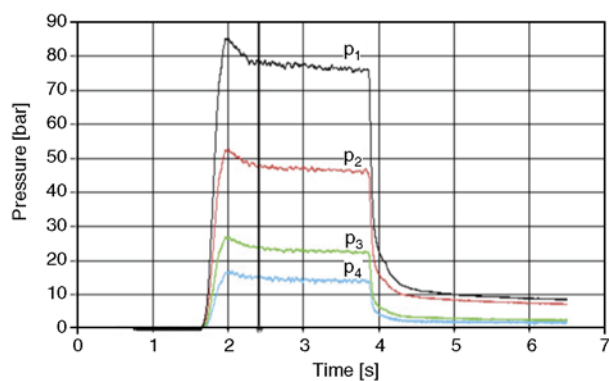


Figure 6. Measured pressure curves

The molten polymer flows out freely from this time and the measured pressures are roughly constant. These constant pressures were used in the calculations. The pressure drops close to the end of the cavity between p_3 and the p_4 pressure were smaller than the former pressure drops. It can be explained by the end effect of the die.

Minimum three injections were made by each set up and the pressure curve was recorded if the standard deviation was less than 5%. The average deviation was less than 1%.

4. Results and discussion

4.1. Investigation of the flow

The measuring range was 500–9000 1/s. Three different temperatures were investigated. The calculated apparent flow curves are shown in Figure 7. These curves correspond to the curves of pseudo plastic materials: increasing the shear rate, the viscosity of the melt decreases.

Correction of cross section showed that the apparent shear rate increased (Rabinowitsch correction), and the apparent shear stress decreased (Figure 8).

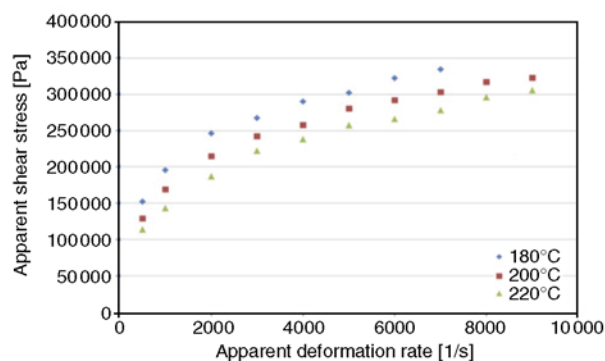


Figure 7. Effect of the cross section correction

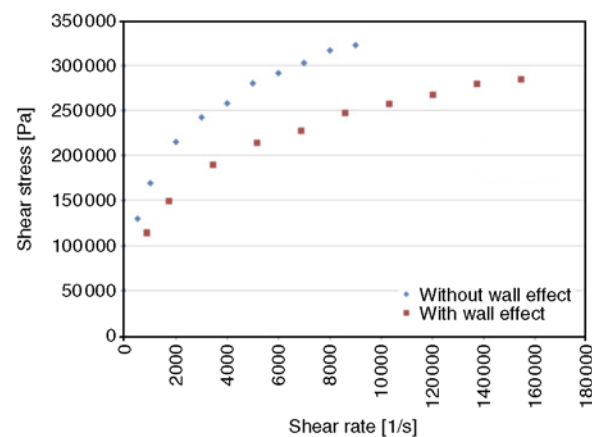


Figure 8. Flow curves calculated with and without the wall effect

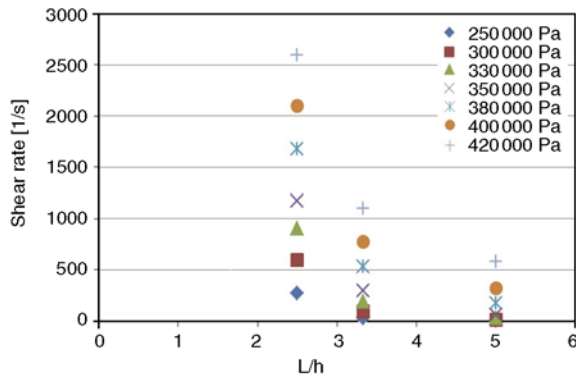


Figure 9. Mooney plots

The Mooney correction was calculated by the measurement of die inserts No 1,2,3. It was found that the slope of the Mooney lines were negative so there is no slip on the wall (Figure 9)

The Bagley correction was calculated by the measurement with inserts No. 4, 5 and 6 (Figure 10). It can be seen that the smallest l/h ratio was 15. It is rather far from the ideal l/h range (close to 0), however the regression constants of the lines are above 0,98. The calculated values are summarised in Table 4.

The apparent values were corrected and the real viscosity curves are shown in Figure 11. For comparison, the material was tested by two other kinds of

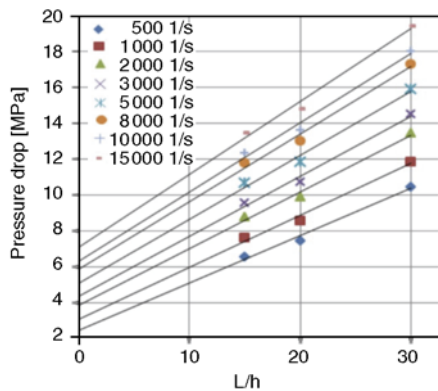


Figure 10. Bagley plot ($T_{mat} = 180^{\circ}C$)

Table 4. Constants of the Bagley plots

$\dot{\gamma}$ [1/sec]	Slope of Bagley plots [Pa·s]	Extrapolated pressure drop [Pa]	Linear regression (R^2)
500	265 175	2 415 699	0.9878
1 000	290 716	3 046 552	0.9877
2 000	318 000	3 809 722	0.9874
3 000	335 000	4 327 469	0.9873
5 000	357 000	5 065 246	0.9870
8 000	378 000	5 838 593	0.9868
10 000	389 000	6 240 761	0.9866
15 000	408 000	7 034 650	0.9864

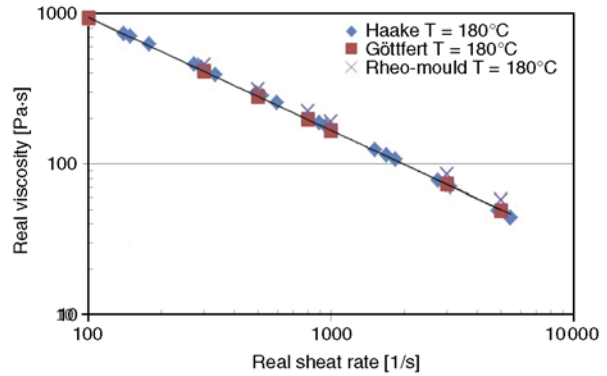


Figure 11. Real viscosity curves

Table 5. The constants of the viscosity curves

Instrument	μ_1	n
Haake	29 706	0.250
Götffert	30 349	0.246
Rheo-mould	29 091	0.270

instruments. Haake extrusionmeter (Miskolc University) and Götffert Rheograph 25 were used. Correlation of the results of the different instruments is excellent.

The Equation (21) was fit to the calculated real viscosity curves, where μ_1 is a constant without real physical meaning. The constants of the equation are listed in the Table 5 (Equation (21)).

$$\eta = \mu_1 \dot{\gamma}^{n-1} \tag{21}$$

4.2. Investigation of thermal condition by dimensionless quantities

Calculations were made by the dimensionless quantities (Equations 16–18) using data of the minimum and the maximum flow rate. The mould and material temperature and the cross section of the slit die were changed, too. The results are summarised in Table 6 and Table 7.

Table 6. Dimensionless quantities ($T_m = 180^\circ\text{C}$)

Mould	T_{mould}	Flow rate	Graetz-number	Nahme-number	Brinkman-number	p_1 [bar]	
Die 1 $h = 2$ mm $w = 15$ mm	30°C	min.	183	25	3	300	
		max.	2198	1353	42	350	
	90°C	min.	183	29	1.23	173.8	
		max.	2198	681	28.6	345.4	
	180°C	min.	–	–	–	149	
		max.	–	–	–	290	
Die 2 $h = 3$ mm $w = 15$ mm	30°C	min.	274	35	1.6	147.9	
		max.	4946	992	44	232.7	
	90°C	min.	274	34	2.1	136.8	
		max.	4946	1388	64.2	234.4	
	Die 3 $h = 4$ mm $w = 15$ mm	30°C	min.	366	29	1.3	90.6
			max.	6595	807	36.6	144.8
90°C		min.	366	29	1.9	88.7	
		max.	6595	859	55	148.6	

Table 7. Dimensionless quantities ($T_m = 220^\circ\text{C}$)

Mould	T_{mould}	Flow rate	Graetz-number	Nahme-number	Brinkman-number	p_1 [bar]	
Die 1 $h = 2$ mm $w = 15$ mm	30°C	min.	183	26	2	260.5	
		max.	2198	570	44	318.3	
	90°C	min.	183	20	1.36	150.9	
		max.	2198	520	34	215.4	
	220°C	min.	–	–	–	106	
		max.	–	–	–	270	
Die 2 $h = 3$ mm $w = 15$ mm	30°C	min.	274	24	1.41	127.4	
		max.	4946	563	33	170.3	
	90°C	min.	274	29.2	1.26	114.8	
		max.	4946	879	38	196.7	
	Die 3 $h = 4$ mm $w = 15$ mm	30°C	min.	366	23	0.92	74.4
			max.	6595	608	24.4	115.0
90°C		min.	366	15	0.7	46.3	
		max.	6595	700	17	119.6	

It can be seen that the Graetz number is larger than 100 in every set up. As the calculated Nahme numbers are much larger than 1, the cross heat flow is much smaller than the axial heat flow. However, it should be emphasised that on the cavity wall a frozen polymeric layer was developed affecting the efficient cross-section of the flow. This thickness is proportional to the pressure drop; the higher the pressure drop is, the thicker the frozen layer is. According to the measured and calculated values (Table 6, Table 7), increasing the height of the cavity the effect of the mould temperature on the pressure becomes smaller meaning that the frozen layer has less effect on the flow. Because of this frozen layer, the flow cross section must be smaller, and it has effect on the pressure drop and the dissipation heat, too. Applying the thinnest die ($h = 2$ mm) and

cooled mould temperature, the pressure drop was the highest.

Brinkman number was larger than one in every setup (except two measurements with die 3 at 220°C). This means that the dissipation heat has a larger effect on the viscosity than the perpendicular heat transfer.

The measured pressure drop between two sensors ($\Delta p_{\text{measured}}$), the average temperature rising by dissipation heat (ΔT_{dissip}), the real viscosity (η_{measured}), the viscosity decrease by dissipation heat (η_{dissip}), the viscosity decrease by pressure (η_{pressure}) and the corrected pressure drop ($\Delta p_{\text{corrected}}$) are summarised in Table 8.

The effect of the pressure and the temperature ($\Delta p_{\text{corrected}}$) were calculated by Laun. $\Delta p_{\text{measured}}$ and $\Delta p_{\text{corrected}}$ are in good correlation. The average dif-

Table 8. Effect of the dissipation heat and the pressure on viscosity

	T _{material} [°C]	180	180	220	220
	T _{mould} [°C]	30	180	30	220
Q					
$\Delta p_{\text{measured}}$ [MPa]	min.	10.67	12.54	11.42	8.53
	max.	15.95	28.24	14.9	20.65
$\Delta T_{\text{dissip.}}$ [°C]	min.	5.4	6.33	5.7	4.31
	max.	8	14.27	7.5	10.4
η_{measured} [Pa·s]	min.	267	313.5	285.6	213.3
	max.	20	35.3	18.59	25.8
η_{dissip} [Pa·s]	min.	232	265.8	245.8	190.7
	max.	16.1	24.35	15.3	19.67
η_{pressure} [Pa·s]	min.	277.6	328.2	297.8	220
	max.	21.2	39.14	19.7	27.8
$\Delta p_{\text{corrected}}$ [MPa]	min.	11.4	13.47	12.23	9.03
	max.	17.2	28.1	16	22.04

ference is less than 6%. This good correlation means that the dissipation heat equalises the effect of the pressure on the viscosity of the melt.

5. Conclusions

A new type of rheological measuring system has been designed and manufactured. The special injection mould can be used to determine the flow curve of molten polymers during the injection moulding process. If the mould is heated up to the processing temperature, the flow condition is close to adiabatic, especially by higher flow rate. It was found that the mould temperature has a smaller effect on the flow condition if the cross section is bigger than 2 mm.

References

- [1] Clavería I., Javierre C., Ponz L.: Method for generation of rheological model to characterize non-conventional injection molding by means of spiral mold. *Journal of Materials Processing Technology*, **162–163**, 477–483 (2005). DOI: [10.1016/j.jmatprotec.2005.02.065](https://doi.org/10.1016/j.jmatprotec.2005.02.065)
- [2] Chen S. C., Tsai R. I., Chein R. D., Lin T. K.: Preliminary study of polymer melt rheological behavior flowing through micro-channels. *International Communications in Heat and Mass Transfer*, **32**, 501–510 (2005). DOI: [10.1016/j.icheatmasstransfer.2004.07.004](https://doi.org/10.1016/j.icheatmasstransfer.2004.07.004)
- [3] Chen C-S., Chen S-C., Liaw W-L., Chien R-D.: Rheological behavior of POM polymer melt flowing through micro-channels. *European Polymer Journal*, **44**, 1891–1898 (2008). DOI: [10.1016/j.eurpolymj.2008.03.007](https://doi.org/10.1016/j.eurpolymj.2008.03.007)
- [4] Benhadou M., Haddout A., Villoutreix G.: Injection of polypropylene reinforced with short glass fibers: Rheological behavior. *Journal of Reinforced Plastics and Composites*, **26**, 1357–1366 (2007). DOI: [10.1177/0731684407079735](https://doi.org/10.1177/0731684407079735)
- [5] Bariani P. F., Salvador M., Lucchetta G.: Development of a test method for the rheological characterization of polymers under the injection molding process conditions. *Journal of Materials Processing Technology*, **191**, 119–122 (2007). DOI: [10.1016/j.jmatprotec.2007.03.089](https://doi.org/10.1016/j.jmatprotec.2007.03.089)
- [6] Haddout A., Villoutreix G.: Polymer melt rheology at high shear rates. *International Polymer Processing*, **2000**, 291–296 (2000).
- [7] Szűcs A.: Study of non-isothermal mould filling. in ‘Proceedings of International Doctoral Seminar, Smolenice, Slovakia’, 467–474 (2010).
- [8] Belina K., Szűcs A.: Investigation of polymer flow during filling stage. in ‘Proceedings of PPS2006 conference, Pretoria, South Africa’ p.4 (2006).
- [9] Chang D. H.: *Rheology in polymer processing*. Academic Press, New York (1976).
- [10] Son Y.: Determination of shear viscosity and shear rate from pressure drop and flow rate relationship in a rectangular channel. *Polymer*, **48**, 632–637 (2007). DOI: [10.1016/j.polymer.2006.11.048](https://doi.org/10.1016/j.polymer.2006.11.048)
- [11] Hay G., Mackay M. E., McGlashan S. A., Park Y.: Comparison of shear stress and wall slip measurement techniques on a linear low density polyethylene. *Journal of Non-Newtonian Fluid Mechanics*, **92**, 187–201 (2000). DOI: [10.1016/S0377-0257\(00\)00096-3](https://doi.org/10.1016/S0377-0257(00)00096-3)
- [12] Halász L.: *Control methods in polymer processing*. Elsevier, Amsterdam (1994).
- [13] Laun H. M.: Pressure dependent viscosity and dissipative heating in capillary rheometry of polymer melts. *Rheologica Acta*, **42**, 295–308 (2003). DOI: [10.1007/s00397-002-0291-6](https://doi.org/10.1007/s00397-002-0291-6)
- [14] Laun H. M.: Polymer melt rheology with a slit die. *Rheologica Acta*, **22**, 171–185 (1983). DOI: [10.1007/BF01332370](https://doi.org/10.1007/BF01332370)

Synthesis and characterization of poly(sodium-p-styrenesulfonate)/modified SiO₂ spherical brushes

N. Su¹, H. B. Li^{1*}, H. M. Zheng¹, S. P. Yi², X. H. Liu¹

¹School of Printing and Packaging, Wuhan University, 430079 Wuhan, China

²College of Chemistry and Molecular Sciences, Wuhan University, 430072 Wuhan, China

Received 12 December 2011; accepted in revised form 7 March 2012

Abstract. The multistep procedures for preparing novel anionic spherical polyelectrolyte brushes (ASPB) by grafting sodium-p-styrenesulfonate (SSS) from the surface of γ -methacryloxypropyl trimethoxy-silane modified SiO₂ nanoparticles were demonstrated. The morphology of ASPB was characterized by Transmission Electron Microscopy (TEM) and Scanning Electron Microscopy (SEM). The core radius R_c and hydrodynamic radius R_h of ASPB measured by Zeta Potential/Particle Sizer (ZLS) were ca. 50nm and (84.5±1) nm respectively. The percentage of grafting (PG%) of polyelectrolyte brushes was 4.3% investigated by Thermo-gravimetric analysis (TGA). Detailed characterizations on ASPB were performed by cleaving the grafts from the anchoring surface. The molecular weight (M_w) and polydispersity (M_w/M_n) of brushes were 1.788·10³ g/mol and 1.6 respectively from Gel Permeation Chromatography (GPC) measurements. Moreover, R_h and ζ -potential of ASPB in the presence of aqueous NaCl solutions of different concentrations were discussed.

Keywords: *nanomaterials, sodium-p-styrenesulfonate, polyelectrolyte brushes, grafting polymerization, thermal properties*

1. Introduction

Polyelectrolyte brushes consist of polyelectrolyte chains attached to planar or curved surfaces. Owing to novel properties brought about by the strong electrostatic interaction between the densely grafted highly charged chains, an intense research on these systems has been done in the past twenty years. The field of polyelectrolyte brushes is explored as one of the most active fields in polymer science [1, 2]. If the polyelectrolyte chains affix to the surface of spheres, spherical polyelectrolyte brushes (SPB) result [3, 4]. With the advantage of spherical symmetry or quasi-symmetric structure, SPB have been used in a variety of areas, such as organic-inorganic composite materials [5], carrier system of nanoparticles [6], biocompatibility [7], papermaking [8], etc. Hence, the synthesis of novel SPB to meet the

application needs has attracted considerable attention recently.

In general, the synthesis of SPB by chemically grafted polyelectrolytes [9, 10] mainly involves two different strategies: ‘grafting to’ and ‘grafting from’. The former method is applied by attaching polyelectrolyte chains with appropriate functional end or side groups to reactive surfaces. The grafting density of brushes formed is limited in this fashion because of the steric hindrance among the pre-formed polymers [11–13]. The latter strategy, the so-called ‘grafting from’ technique [14–17], is based on the surface modified by polymerization initiators. Due to bearing initiator functionalities on the surface of core, it can lead to a dense layer of chemically bound polyelectrolyte chains.

*Corresponding author, e-mail: lhb@whu.edu.cn

© BME-PT

In this study, we have succeeded in grafting sodium-p-styrenesulfonate (SSS) from the surface of modified SiO₂ using conventional free radical polymerization. Compared with the methods which are widely used in synthesizing polyelectrolyte brushes, such as ATRP (atom transfer radical polymerization) polymerization and RAFT (reversible addition-fragmentation chain transfer) polymerization, this approach is more simple, practicable and maneuverable. In other words, this technique is of significance for extensive industrial applications due to its low cost.

2. Experimental

2.1. Materials

Tetraethyl orthosilicate (TEOS), γ -methacryloxypropyl trimethoxy-silane and sodium-p-styrenesulfonate (SSS) were purchased from Sinopharm Chemical Reagent Ltd.. 2,2-Azo-bis-iso-butyronitrile (AIBN) purchased from Shanghai Chemical Co., Ltd. was recrystallized from ethanol and dried under vacuum. Other chemicals and solvents including Hydrochloric acid (HCl, 34 wt%), Ammonia (NH₃ (aq), 25–28 wt%), Sodium hydroxide, toluene and ethanol were analytical reagents. They were used without further purification.

2.2. Preparation and modification of SiO₂ nanoparticles

Monodisperse spherical SiO₂ nanoparticles (ca. 100 nm) were prepared using tetraethoxysilane by sol-gel method [18]. The γ -methacryloxypropyl trimethoxy-silane was used to introduce ethylene groups onto the surface of SiO₂ nanoparticles and create a cleavable group for grafted polyelectrolyte chains. In a typical run, 4.2 g of γ -methacryloxypropyl trimethoxy-silane was dissolved in 100 ml of ethanol/water (10/1, v/v) mixture, followed by

adjusting pH to 4 with HCl for the hydrolysis of γ -methacryloxypropyl trimethoxy-silane. The hydrolysis reaction proceeded at room temperature for 1h. After the complete addition of 100 g of 4 wt% SiO₂ dimethylcarbinol suspension, the reaction mixture was stirred vigorously at 70°C for 5 h. The products were then separated from the mixture with a high-speed centrifuge (TG16-II, Changsha PINGFAN Instruments and Meter Co., Ltd.), and washed with ethanol three times by repeated centrifugation. The resulting products were dried in vacuum at 65°C for 12 h.

2.3. Synthesis of ASPB

The surface-initiated polymerization of SSS monomer on modified SiO₂ nanoparticles was carried out in the presence of a small amount of sacrificial initiator AIBN under a nitrogen atmosphere. The reaction protocol in Figure 1 clearly shows the sequence used to synthesize the brushes and cleave them from the silica particles. An amount of 10 g of 4 wt% modified SiO₂ ethanol/water (10/1, v/v) mixture was appended into a three-necked flask containing 100 ml of toluene, followed by addition of 12 mg of initiator [AIBN] with vigorously stirring. After the mixture was heated to 40°C, 400 mg of monomer [SSS] was then added. Polymerization was allowed to proceed for 24 h. The synthesized ASPB were separated from toluene, and subjected to three sequential washings with ethanol and distilled water before finally being dried in vacuum at 65°C for 12 h. The products were stored in a desiccator for other analytical experiments.

2.4. Cleavage of grafted polyelectrolyte chains

The chemistry for cleaving long polyelectrolyte chains from the surface of modified SiO₂ nanoparticles was also illustrated in Figure 1. The ASPB

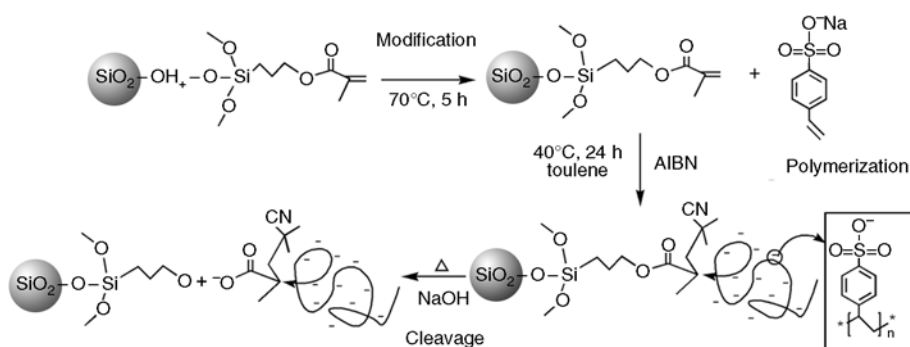


Figure 1. The reaction scheme for the synthesis of ASPB and the hydrolysis of PSS chains

were hydrolyzed by refluxing in 2M of NaOH (aq) at 85°C for 48 h. The SiO₂ cores and grafted polyelectrolyte brushes in the reaction mixture were then carefully separated by centrifuging. The PSS chains were obtained by extraction, neutralization and concentration of supernatant.

2.5. Characterization methods

Fourier transform infrared spectrum (FTIR) was recorded using a Nicolet AVATAR 360FT [Japan] spectrometer in region between 4000 cm⁻¹ and 500 cm⁻¹. The morphologies of samples were characterized by Transmission electron microscopy (TEM) and Scanning electron microscopy (SEM). TEM measurements were performed on a JEM-100CX II transmission electron microscope at an acceleration voltage of 100 kV. SEM images were made with a high resolution Quanta 200 scanning electron microscope operated at 30 kV. X-ray photoelectron spectroscopy (XPS) measurements were carried out on a FEI ‘Quanta 200’ instrument operating at a voltage of 30 kV with MnK α radiation. The PG% of polyelectrolyte brushes was calculated by Thermo-gravimetric analysis (TGA). TGA measurements were conducted with a SETSYS-1750 [SETARAM] instrument at the heating rate of 10°C/min from 25 to 750°C under a nitrogen atmosphere. The average initial sample mass was ca. 5 mg. The PG% of polyelectrolyte brushes could be defined by Equation (1) [19]:

$$PG\% = \frac{m_1}{m_2} \cdot 100\% \quad (1)$$

where m_1 is the weight of all grafted PSS brushes, m_2 is the weight of SiO₂.

Gel Permeation Chromatography (GPC) was performed on Spectra SERIES P100 to obtain the molecular weight distribution of brushes. The surface grafting density could be defined as moles of polymer graft per gram [mole/g] or per square [mole/m²] of the matrix. Knowing the average molecular weight (M_w) and the PG% of polyelectrolyte brushes, the surface grafting density σ was calculated using Equation (2) [20]:

$$\sigma = \frac{PG}{M_w} \quad (2)$$

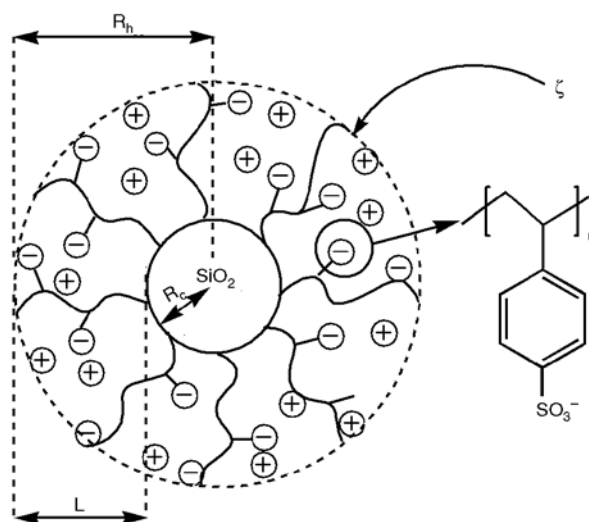


Figure 2. A sketch of ASPB in this study

Considering the surface area of silica particles, the calculation of surface grafting density could also be achieved by chains per square nanometer surface. The Zeta Potential/Particle Sizer (ZLS, Nicomp 380, USA) was used to measure the ζ -potential and R_h of ASPB. Figure 2 displayed this model system termed ASPB. The core radius R_c consisted of the radius of SiO₂ and the thin layer thickness of γ -methacryloxypropyl trimethoxy-silane, from which polyelectrolyte chains (PSS) were grafted. L denoted the thickness of the brush layer, R_h the hydrodynamic radius and ζ the zeta potential.

3. Results and discussion

3.1. FTIR and XPS analyses

Figure 3 shows the FTIR spectra of SiO₂ (a), modified SiO₂ (b), cleaved PSS chains (c) and SSS (d).

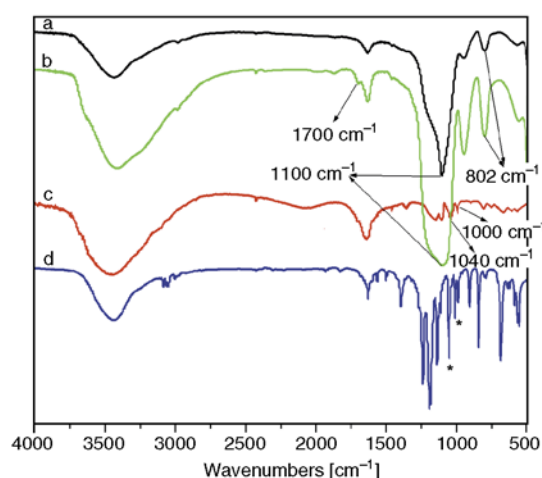


Figure 3. FTIR curves of SiO₂ (a), modified SiO₂ (b), cleaved PSS chains (c), and NaSS (d)

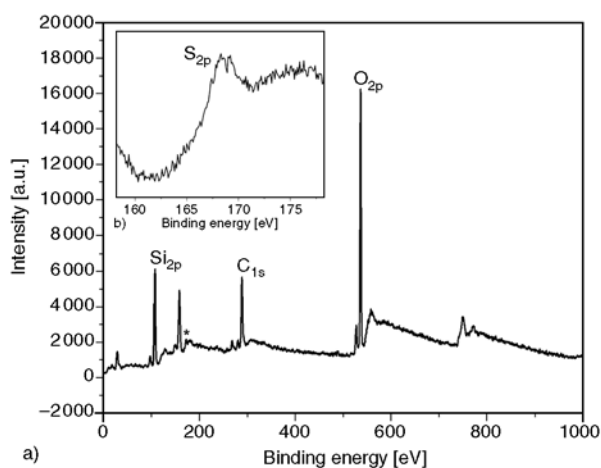


Figure 4. XPS spectra of wide region spectroscopy (a) and S 2p (b) of ASPB

The characteristic peaks at 1100 and 802 cm^{-1} for both SiO_2 (Figure 3a) and modified SiO_2 (Figure 3b) are visible, attributed to the Si–O–Si stretching vibration. The spectrum of modified SiO_2 (Figure 3b) displays the characteristic absorption bands at 1700 cm^{-1} of C=O stretching vibration of the carboxyl group (–COO–), which suggests that γ -methacryloxypropyl trimethoxy-silane interacts

with SiO_2 . The FTIR spectra of cleaved PSS chains and SSS are shown in Figure 3c and Figure 3d, respectively. Compared with the characteristic peaks in the FTIR spectrum of SSS, major characteristic peaks appear in the FTIR spectrum of cleaved PSS chains. The peaks at 1000 and 1040 cm^{-1} are attributed to the S=O stretching vibration [21] confirming the existence of PSS chains on modified SiO_2 surface. Thus the FTIR spectra clearly support the surface modification reaction and polymerization given in Figure 1.

Figure 4a shows a typical XPS wide-scan spectrum for ASPB in which the exhibited peak at 168.5 eV is observed. The narrow spectrum of S 2p is also displayed in Figure 4b. Thereby, the appearance of sulfur signal further supports the surface modification reaction.

3.2. Morphologies and particle size distribution

The TEM and SEM images clearly indicate the morphologies of SiO_2 , modified SiO_2 and ASPB. As shown in Figure 5, they are well dispersed and

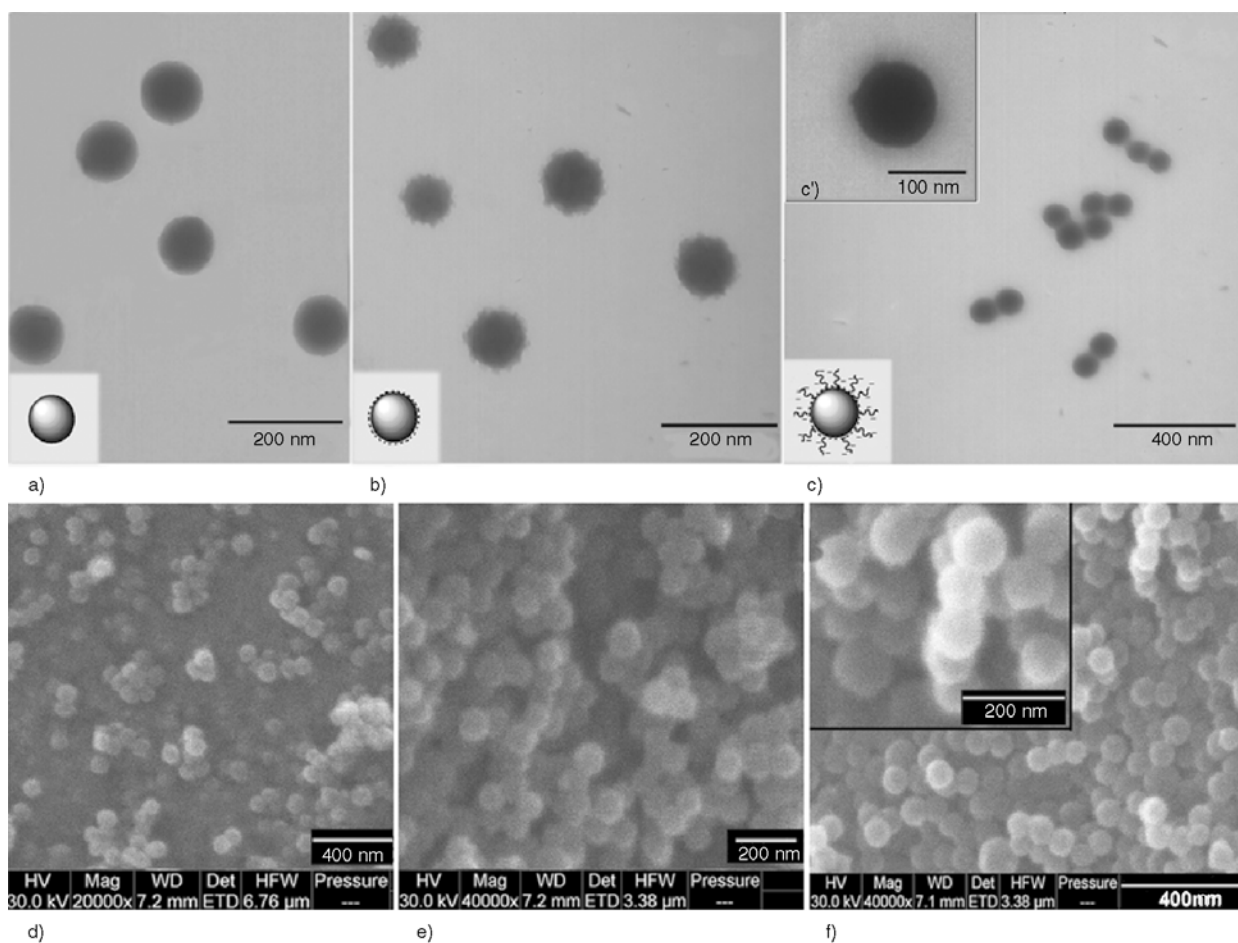


Figure 5. TEM and SEM images of SiO_2 (a, d), modified SiO_2 (b, e), ASPB (c, f) and an enlargement of c (c')

have uniform spherical structure. The average diameter of SiO₂ core is ca.100 nm. Figure 5c and Figure 5f display the TEM and SEM images of ASPB. The blurring and hair edges can be observed in Figure 5c' which is an enlargement of Figure 5c. The hydrodynamic radius R_h of ASPB is (84.5±1) nm determined by ZLS, which demonstrates that the polyelectrolyte brushes have been anchored onto modified SiO₂ cores successfully.

3.3. Determination of percentage of grafting (PG%)

For any brush polymer system PG% is an important factor which is related to the morphology of brushes and determines the properties of the system. In order to calculate the PG% of PSS brushes on the surface of modified SiO₂ cores, TG-DTG is employed (Figure 6). Compared with the SiO₂, the main weight losses for modified SiO₂ (10.1%) and ASPB (13.4%) have occurred between 200 and 750°C. The TGA thermogram of γ -methacryloxypropyl trimethoxy-silane is also displayed as insert (Figure 6d) to assess the thermal decomposition temperature of products. As shown in Figure 6d, the weight loss of γ -methacryloxypropyl trimethoxy-silane occurs in the temperature range of 90–190°C which may be because of the thermopolymerization. The decomposition temperature sections of modified SiO₂ and the number of DTG peaks of ASPB are different. For the modified SiO₂, only one endothermic peak at 458°C is observed, attributed to the decomposition of γ -methacryloxypropyl trimethoxy-silane with 90.2% residues. In the case of ASPB, a new endothermic peak appears at higher

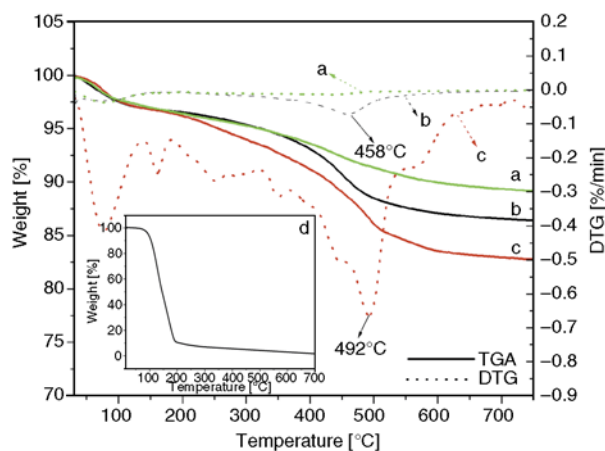


Figure 6. TG-DTG curves of SiO₂ (a), modified SiO₂ (b), and ASPB (c); the insert shows the TGA curve of γ -methacryloxypropyl trimethoxy-silane (d)

temperatures (490°C) [22] with 88.1% residues. It may be due to the thermal insulating property of SiO₂ particles. More energy is required, which suggests that the polymer has been bonded to modified SiO₂ nanoparticles. The PG% is 4.3% calculated from Equation (1).

3.4. Molecular weight and surface grafting density

After cleaving the polyelectrolyte chains from the surface of modified SiO₂ nanoparticles, the molecular weight distribution of PSS brushes is measured by GPC. The GPC curve of cleaved PSS chains is shown in Figure 7. Taking 0.1 M NaCl (aq) as mobile phase, PEG is used as the internal standard at room temperature. The M_w and polydispersity (M_w/M_n) are $1.788 \cdot 10^3$ g/mol and 1.6 respectively. The surface grafting density σ is $2.013 \cdot 10^{-5}$ mol/g or $0.047 \mu\text{mol}/\text{nm}^2$.

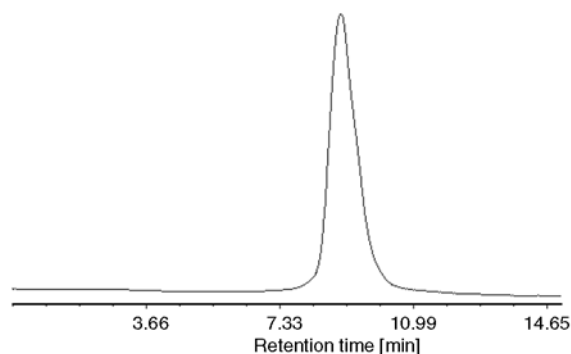


Figure 7. GPC curve of cleaved PSS chains

3.5. ζ -potential and R_h

Figure 8 illustrates the ζ -potential and R_h of ASPB as a function of aqueous NaCl solutions of different concentrations. It is shown that the magnitude of ζ -potential and R_h decrease with increasing salt concentration. At the lowest salt concentration (10^{-4} M), electrostatic interaction prevails and the grafted polyelectrolyte chains adopt an extended conformation. Intermediate salt concentrations result in a partial screening of the electrostatic interaction and a shrinking of the brush layer. As shown in Figure 8, when salt concentration is around 0.1 M, contraction of the brush layer becomes pronounced ($R_h \approx 60$ nm). This effect can be well captured by the theory of Hariharan *et al.* [23]. In case of ASPB, the electrostatic screening increases with increasing salt concentration resulting in a reduced elec-

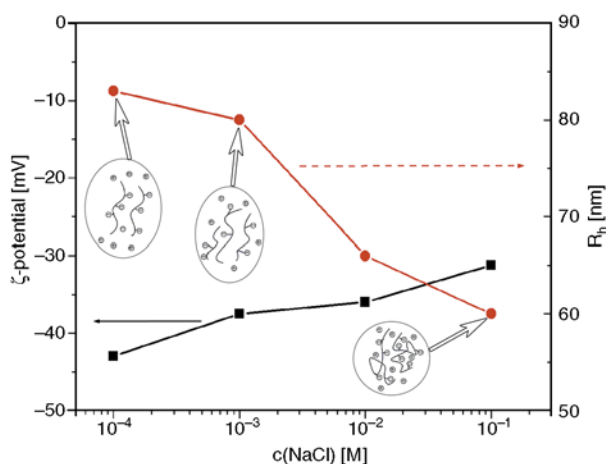


Figure 8. ζ -potential and R_h of ASPB as a function of aqueous NaCl solutions of different concentrations ($T = 25^\circ\text{C}$, $\text{pH} = 6$, $c(\text{ASPB}) = 1 \text{ mg/ml}$)

trophoretic mobility [24]. This is presumably due to the fact that continuous collapse of the brush layer with salt concentration has the effect of moving the shear plane closer to the surface, thus the ζ -potential of particles decreases [25]. In monovalent electrolyte solution (aqueous NaCl solutions), the value of ζ -potential at salt concentration of 0.1 M is still below -30 mV.

4. Conclusions

In this paper, novel ASPB have been successfully synthesized using conventional free radical polymerization. Different characterization and analytical methods confirm PSS brushes have been attached to the surface of modified SiO_2 cores. The synthesized ASPB are well dispersed and have uniform spherical structure, high grafting density and a narrow molecular weight distribution. Upon adding sodium ions (Na^+) the brush layer responds by contracting, and the ζ -potential of particles decreases.

Acknowledgements

This research was supported by Scientific Research Program of Wuhan University (217274815) and National Natural Science Foundational of China (31170558).

References

[1] Pincus P.: Colloid stabilization with grafted polyelectrolytes. *Macromolecules*, **24**, 2912–2919 (1991). DOI: [10.1021/ma00010a043](https://doi.org/10.1021/ma00010a043)

[2] Borisov O. V., Birshtein T. M., Zhulina E. B.: Collapse of grafted polyelectrolyte layer. *Journal de Physique II*, **1**, 521–526 (1991). DOI: [10.1051/jp2:1991186](https://doi.org/10.1051/jp2:1991186)

[3] Zhang L., Yu K., Eisenberg A.: Ion-induced morphological changes in ‘crew-cut’ aggregates of amphiphilic block copolymers. *Science*, **272**, 1777–1779 (1996). DOI: [10.1126/science.272.5269.1777](https://doi.org/10.1126/science.272.5269.1777)

[4] Biver C., Hariharan R., Mays J. W., Russel W. B.: Neutral and charged polymer brushes: A model unifying curvature effects from micelles to flat surfaces. *Macromolecules*, **30**, 1787–1792 (1997). DOI: [10.1021/ma9610065](https://doi.org/10.1021/ma9610065)

[5] Velten U., Sheldon R. A., Caseri W. R., Suter U. W., Li Y.: Polymerization of styrene with peroxide initiator ionically bound to high surface area mica. *Macromolecules*, **32**, 3590–3597 (1999). DOI: [10.1021/ma9813791](https://doi.org/10.1021/ma9813791)

[6] Sharma G., Ballauff M.: Cationic spherical polyelectrolyte brushes as nanoreactors for the generation of gold particles. *Macromolecular Rapid Communications*, **25**, 547–552 (2004). DOI: [10.1002/marc.200300107](https://doi.org/10.1002/marc.200300107)

[7] Wittmann A., Ballauff M.: Temperature-induced unfolding of ribonuclease A embedded in spherical polyelectrolyte brushes. *Macromolecular Bioscience*, **5**, 13–20 (2005). DOI: [10.1002/mabi.200400133](https://doi.org/10.1002/mabi.200400133)

[8] Mei Y., Abetz C., Birkert O., Schädler V., Leyrer R. J., Ballauff M.: Interaction of spherical polyelectrolyte brushes with calcium carbonate and cellulose fibers: Mechanistic studies and their application in papermaking. *Journal of Applied Polymer Science*, **102**, 233–241 (2006). DOI: [10.1002/app.23637](https://doi.org/10.1002/app.23637)

[9] Motschmann H., Stamm M., Toprakcioglu C.: Adsorption kinetics of block copolymers from a good solvent: A two-stage process. *Macromolecules*, **24**, 3681–3688 (1991). DOI: [10.1021/ma00012a032](https://doi.org/10.1021/ma00012a032)

[10] Schepelina O., Zharov I.: Poly(2-(dimethylamino)ethyl methacrylate)-modified nanoporous colloidal films with pH and ion response. *Langmuir*, **24**, 14188–14194 (2008). DOI: [10.1021/la802453z](https://doi.org/10.1021/la802453z)

[11] Retsch M., Walther A., Loos K., Müller A. H. E.: Synthesis of dense poly(acrylic acid) brushes and their Interaction with amine-functional silsesquioxane nanoparticles. *Langmuir*, **24**, 9421–9429 (2008). DOI: [10.1021/la8009767](https://doi.org/10.1021/la8009767)

[12] Kobayashi M., Yamaguchi H., Terayama Y., Wang Z., Ishihara K., Hino M., Takahara A.: Structure and surface properties of high-density polyelectrolyte brushes at the interface of aqueous solution. *Macromolecular Symposia*, **279**, 79–87 (2009). DOI: [10.1002/masy.200950513](https://doi.org/10.1002/masy.200950513)

- [13] Boyes S. G., Akgun B., Brittain W. J., Foster M. D.: Synthesis, characterization, and properties of polyelectrolyte block copolymer brushes prepared by atom transfer radical polymerization and their use in the synthesis of metal nanoparticles. *Macromolecules*, **36**, 9539–9548 (2003).
DOI: [10.1021/ma035029c](https://doi.org/10.1021/ma035029c)
- [14] Parnell A. J., Martin S. J., Dang C. C., Geoghegan M., Jones R. A. L., Crook C. J., Howse J. R., Ryan A. J.: Synthesis, characterization and swelling behaviour of poly(methacrylic acid) brushes synthesized using atom transfer radical polymerization. *Polymer*, **50**, 1005–1014 (2009).
DOI: [10.1016/j.polymer.2008.11.051](https://doi.org/10.1016/j.polymer.2008.11.051)
- [15] Sanjuan S., Perrin P., Pantoustier N., Tran Y.: Synthesis and swelling behavior of pH-responsive polybase brushes. *Langmuir*, **23**, 5769–5778 (2007).
DOI: [10.1021/la063450z](https://doi.org/10.1021/la063450z)
- [16] Zhao B., Brittain W. J.: Polymer brushes: Surface-immobilized macromolecules. *Progress in Polymer Science*, **25**, 677–710 (2000).
DOI: [10.1016/S0079-6700\(00\)00012-5](https://doi.org/10.1016/S0079-6700(00)00012-5)
- [17] Zhang H. N., R  he J.: Swelling of poly(methacrylic acid) brushes: Influence of monovalent salts in the environment. *Macromolecules*, **38**, 4855–4860 (2005).
DOI: [10.1021/ma047501f](https://doi.org/10.1021/ma047501f)
- [18] Rao K. S., El-Hami K., Kodaki T., Matsushige K., Makino K.: A novel method for synthesis of silica nanoparticles. *Journal of Colloid and Interface Science*, **289**, 125–131 (2005).
DOI: [10.1016/j.jcis.2005.02.019](https://doi.org/10.1016/j.jcis.2005.02.019)
- [19] Zhang H., Lei X., Su Z., Liu P.: A novel method of surface-initiate atom transfer radical polymerization of styrene from silica nanoparticles for preparation of monodispersed core-shell hybrid nanospheres. *Journal of Polymer Research*, **14**, 253–260 (2007).
DOI: [10.1007/s10965-007-9104-z](https://doi.org/10.1007/s10965-007-9104-z)
- [20] Jayachandran K. N., Chatterji P. R.: Synthesis of dense brush polymers with cleavable grafts. *European Polymer Journal*, **36**, 743–749 (2000).
DOI: [10.1016/S0014-3057\(99\)00111-1](https://doi.org/10.1016/S0014-3057(99)00111-1)
- [21] Chu C-C., Wang Y-W., Wang L., Ho T-I.: Synthesis and characterization of novel conductive star polymers containing PSS/PANI arms. *Synthetic Metals*, **153**, 321–324 (2005).
DOI: [10.1016/j.synthmet.2005.07.246](https://doi.org/10.1016/j.synthmet.2005.07.246)
- [22] Castro C., Gargallo L., Radic D., Kortaberria G., Mondragon I.: Blends containing chitosan and poly(sodium-4-styrene sulphonate). Compatibility behavior. *Carbohydrate Polymers*, **83**, 81–87 (2011).
DOI: [10.1016/j.carbpol.2010.07.027](https://doi.org/10.1016/j.carbpol.2010.07.027)
- [23] Hariharan R., Biver C., Russel W. B.: Ionic strength effects in polyelectrolyte brushes: The counterion correction. *Macromolecules*, **31**, 7514–7518 (1998).
DOI: [10.1021/ma9718199](https://doi.org/10.1021/ma9718199)
- [24] Saleh N., Kim H-J., Phenrat T., Matyjaszewski K., Tilton R. D., Lowry G. V.: Ionic strength and composition affect the mobility of surface-modified Fe⁰ nanoparticles in water-saturated sand columns. *Environmental Science and Technology*, **42**, 3349–3355 (2008).
DOI: [10.1021/es071936b](https://doi.org/10.1021/es071936b)
- [25] Borget P., Lafuma F., Bonnet-Gonnet C.: Characterizations and properties of hairy latex particles. *Journal of Colloid and Interface Science*, **285**, 136–145 (2005).
DOI: [10.1016/j.jcis.2004.11.019](https://doi.org/10.1016/j.jcis.2004.11.019)